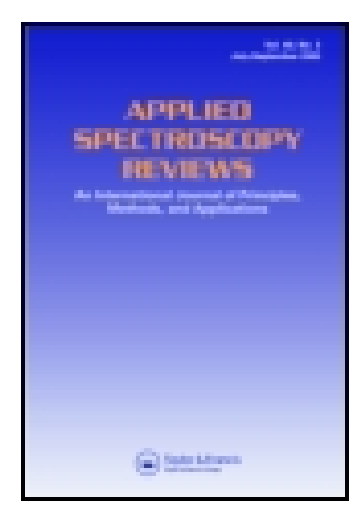
This article was downloaded by: [George Mason University]

On: 18 June 2014, At: 07:57 Publisher: Taylor & Francis

Informa Ltd Registered in England and Wales Registered Number: 1072954 Registered office: Mortimer House,

37-41 Mortimer Street, London W1T 3JH, UK



## Applied Spectroscopy Reviews

Publication details, including instructions for authors and subscription information: http://www.tandfonline.com/loi/laps20

# Raman Spectroscopy of Biological Tissues

Abdullah Chandra Sekhar Talari<sup>a</sup>, Zanyar Movasaghi<sup>b</sup>, Shazza Rehman<sup>c</sup> & Ihtesham ur Rehman<sup>a</sup>

- <sup>a</sup> Department of Materials Sciences and Engineering, The Kroto Research Institute, North Campus, University of Sheffield, Sheffield, UK
- <sup>b</sup> Barts Health NHS Trust, Community Health Services Division, St Leonard's Hospital, London UK
- <sup>c</sup> Department of Medical Oncology, Airedale NHS Foundation Trust, Airedale General Hospital, Skipton Road, Steeton, West Yorkshire, UK Accepted author version posted online: 29 May 2014.

To cite this article: Abdullah Chandra Sekhar Talari, Zanyar Movasaghi, Shazza Rehman & Ihtesham ur Rehman (2014): Raman Spectroscopy of Biological Tissues, Applied Spectroscopy Reviews, DOI: 10.1080/05704928.2014.923902

To link to this article: <a href="http://dx.doi.org/10.1080/05704928.2014.923902">http://dx.doi.org/10.1080/05704928.2014.923902</a>

Disclaimer: This is a version of an unedited manuscript that has been accepted for publication. As a service to authors and researchers we are providing this version of the accepted manuscript (AM). Copyediting, typesetting, and review of the resulting proof will be undertaken on this manuscript before final publication of the Version of Record (VoR). During production and pre-press, errors may be discovered which could affect the content, and all legal disclaimers that apply to the journal relate to this version also.

#### PLEASE SCROLL DOWN FOR ARTICLE

Taylor & Francis makes every effort to ensure the accuracy of all the information (the "Content") contained in the publications on our platform. However, Taylor & Francis, our agents, and our licensors make no representations or warranties whatsoever as to the accuracy, completeness, or suitability for any purpose of the Content. Any opinions and views expressed in this publication are the opinions and views of the authors, and are not the views of or endorsed by Taylor & Francis. The accuracy of the Content should not be relied upon and should be independently verified with primary sources of information. Taylor and Francis shall not be liable for any losses, actions, claims, proceedings, demands, costs, expenses, damages, and other liabilities whatsoever or howsoever caused arising directly or indirectly in connection with, in relation to or arising out of the use of the Content.

This article may be used for research, teaching, and private study purposes. Any substantial or systematic reproduction, redistribution, reselling, loan, sub-licensing, systematic supply, or distribution in any form to anyone is expressly forbidden. Terms & Conditions of access and use can be found at <a href="http://www.tandfonline.com/page/terms-and-conditions">http://www.tandfonline.com/page/terms-and-conditions</a>

#### Raman Spectroscopy of Biological Tissues

#### Abdullah Chandra Sekhar Talari

Department of Materials Sciences and Engineering

The Kroto Research Institute, North Campus,

University of Sheffield, Sheffield, UK

#### Zanyar Movasaghi

Barts Health NHS Trust

Community Health Services Division

St Leonard's Hospital,

London UK

#### Shazza Rehman

Department of Medical Oncology
Airedale NHS Foundation Trust, Airedale General Hospital,

Skipton Road, Steeton, West Yorkshire, (UK)

#### Ihtesham ur Rehman

Department of Materials Sciences and Engineering

The Kroto Research Institute, North Campus,

University of Sheffield, Sheffield, UK

**Abstract:** We published a comprehensive review paper previously reviewing the Raman spectroscopy of biological molecules. This research area has expanded rapidly, which warranted an update to the existing review paper by adding the recently reported studies in literature. This article reviews some of the recent advances of Raman spectroscopy in relation to biomedical applications starting from natural tissues to cancer biology. Raman spectroscopy, an optical molecular detective, is a vibrational spectroscopic technique that has potential not only in cancer diagnosis but also in understanding progression of the disease. This article summarizes some of the most widely observed peak frequencies and their assignments. The aim of this review is to develop a database of molecular fingerprints, which will facilitate researchers in identifying the chemical structure of the biological tissues including most of the significant peaks reported both in the normal and cancerous tissues. It has covered a variety of Raman approaches and its quantitative and qualitative biochemical information. In addition, it covers the use of Raman spectroscopy to analyse a variety of different malignancies including breast, brain, cervical, gastrointestinal, lung, oral, and skin cancer. Multivariate analysis approaches used in these studies have also been covered.

**Key Words:** Raman spectroscopy, biological tissues, analysis of cancer tissues, characteristic peak assignments

#### **AIMS:**

For the purpose of non-invasive diagnostic applications, the vibrational spectroscopic techniques are becoming potential tools. Applications of spectroscopic techniques in biological studies have increased significantly in recent years, and especially clinical investigations regarding detection of cancer and malignancy have gained attention from both clinical and non-clinical researchers. Numerous papers have been published on the diagnostic significance of different spectroscopic and imaging techniques in the field of cancer detection [1-12]. However, there has been a gap in the details of the characteristic peak frequencies and their definitions. This can be attributed to the fact that specific functional groups present in the biological tissues have not yet been fully investigated. In addition, there is no comprehensive review in the literature that addresses the Raman spectroscopic investigations of all biological tissues together, as researchers have to rely on a number of previously published research papers and most of the times the interpretation of the spectral data differs considerably. In this paper considerable amount of spectroscopic investigations published on biological tissues have been reviewed and it shows that there are striking similarities in defining different peak frequencies [13]. Furthermore, by compiling a unique database involving a detailed study on the works, different chemical bands and their assignments of spectral bands could provide significant assistance to research groups focusing on spectroscopy, and which in turn can lead to significant improvements in the quality and quantity of the research done. This article has updated recent Raman spectroscopic investigations of biological tissues; most of them explored multivariate approaches especially in distinguishing cancerous tissues from normal tissues [14-15].

This article endeavours to present a broad and detailed collection of interpretation of Raman spectral frequencies. It is predicted that this article will be of considerable assistance to research groups working on Raman spectroscopy of biological tissues. Moreover, it presents current researchers an overall view of Raman spectroscopic findings in cancer biology especially in detection and understanding the disease at molecular level.

#### INTRODUCTION

Spectroscopy has emerged lately as one of the main tools for biomedical applications and has made considerable progress in the field of clinical assessment. Research has been performed on a wide variety of natural tissues using spectroscopic techniques, including Raman spectroscopy. These vibrational spectroscopic techniques are comparatively straightforward, reproducible, non-invasive to the tissue and only small amounts of material (micrograms to nanograms) with a minimum sample preparation are required. In addition, these techniques also provide molecular level information allowing investigation of functional groups, bonding types and molecular conformations. In vibrational spectra the spectral bands are molecule specific and provide unique information about the biochemical composition. These bands are fairly narrow, easy to resolve and sensitive to molecular structure, conformation and environment.

In studies related to spectroscopic techniques it is strongly believed that both the reliable experimental procedure and characterisation of spectral peak positions and their assignment along with accurate peak detection and definition are of crucial importance. Although a number of scientists have used different techniques, it seems that there is a noticeable similarity in their spectral interpretations of comparable areas in their collected spectra.

# <sup>4</sup> ACCEPTED MANUSCRIPT

In table 1, the spectral interpretation studies are tabulated which have been published so far. This table provides a comprehensive account of spectral frequencies of the biological tissues.

#### RAMAN SPECTROSCOPY

Raman spectroscopy, a molecular and chemical detective, can be used to optically probe the molecular changes associated with diseased tissues [16-17]. Theoretically, when the energy of incident photon is unaltered after collision with a molecule, the scattered photon has the same frequency as the incident photon. This is known as Rayleigh or elastic scattering. When energy is transferred either from the molecule to the photon or vice versa, the scattered photon has less or more than the energy of the incident photon. This is inelastic or Raman scattering and was first observed in 1928 by Sir C. V. Raman, an Indian physicist, who received the Nobel prize 2 years later for work in this field [18]. A very small portion (1 in 10<sup>10</sup>) of the light, however, is in elastically scattered at a different wavelength to the incident light [19]. If the proton has a higher frequency and therefore lower energy than the incident light, this is known as Stokes-Raman and is due to the change in vibrational mode of the sample molecule.

Raman spectra are a plot of scattered intensity as a function of the energy difference between the incident and scattered photons and are obtained by pointing a monochromatic laser beam at a sample. The loss (or gain) in the photon energies corresponds to the difference in the final and initial vibrational energy levels of the molecules participating in the interaction. The resultant spectra are characterized by shifts in wave numbers (inverse of wavelength in cm<sup>-1</sup>) from the incident frequency.

The frequency difference between incident and Raman scattered light is termed the Raman shift, which is unique for individual molecules and is measured by the machines detector and is represented as 1/cm. Raman peaks are spectrally narrow, and in many cases can be associated with the vibration of a particular chemical bond (or a single functional group) in the molecule [4-20-21-22].

#### Raman Spectroscopy Biological Molecules:

A number of researchers have reported on Raman spectroscopy of biological tissues, which include investigations on bone [23- 24-25], cornea [26], cervical tissue [27- 28- 29], epithelial tissue [30- 31- 32], lung [20- 33- 34- 35- 36- 37- 38- 39- 40], breast [21- 41- 42- 43- 44- 45- 46- 47- 48- 49], skin [50- 51- 52- 53- 54- 55- 56- 57- 58- 59- 60- 61], gastro-intestinal tissue [62- 63- 64- 65- 66- 67- 68- 69], brain [70- 71- 72- 73- 74- 75], oral tissue [76- 77- 78- 79- 80- 81- 82], Liver [83- 84- 85], testicular [86], Heme protein [87], Atherosclerotic Plaque [88], serum [89- 90- 91- 92- 93], Human Coronary Arteries [94], lymphocytes [95], Human Blood cells [96- 97- 98- 99], mixed cancer cells [100], human living cells[101], microbial cells [102], Individual Cells [103], saliva [104], DNA [105- 106- 107- 108], Cancer Genes [109], Anti-Cancer Drug [110], tissue processing [111], Raft cultures [112], meningiomas [113], cancer field effects [114], prostate lesion[115], neuroblastoma [116], cancerous cells (to be targeted) [117], and Mammalian cell cultures [118].

This paper is divided into two parts. In the first part a brief summary of the related research is presented which provides a background for spectral data tabulated in the second part of the paper.

Z. Huang et al reported on diagnosis of lung cancer using near-infrared Raman spectroscopy. The objective of their study was to explore the technique for distinguishing tumour from normal bronchial tissue. A rapid-acquisition dispersive-type NIR Raman spectroscopy system was used for tissue Raman studies at 785nm. Raman spectra differed significantly between normal and malignant tumour tissues, namely, squamous cell carcinoma (SSC) and adenocarcinoma. Tumours showed higher percentage signals for nucleic acids, tryptophan and phenylalanine and lower percentage signals for phospholipids, proline and valine, in comparison with normal tissues. Raman spectral shape differences between normal and tumour tissues were also observed particularly in the region of 1000-1100, 1200-1400 and 1500-1700 cm<sup>-1</sup>, which contain signals related to protein and lipid conformations and nucleic acid's CH stretching modes. The ratio of Raman intensities at 1445 to 1655 cm<sup>-1</sup> provided good differentiation between normal and malignant bronchial tissue (p<0.0001). The results of this exploratory study indicated that NIR Raman spectroscopy provides significant potential for non-invasive diagnosis of lung cancer in vivo based on the optic evaluation of biomolecules [20].

K.E. Shafer-Peltier et al reported on Raman spectroscopic model of human breast tissue and its implications for breast cancer diagnosis in vivo. They believed that Raman spectroscopy has the potential to provide real-time, in situ diagnosis of breast cancer during needle biopsy or surgery via an optical fibre probe. To understand the relationship between the Raman spectrum of a sample of breast tissue and its disease state, near-infrared Raman spectroscopic images of human breast tissue were acquired using a confocal microscope. These images were then compared with phase contrast and hematoxylin- and eosin-stained images to develop a chemical/morphological model of breast tissue Raman spectra. The model explained the spectral

features of a range of normal and diseased breast tissue samples, including breast cancer, and it also could be used to relate the Raman spectrum of a breast tissue sample to diagnostic parameters used by pathologists [21].

McManus et al reported that Raman spectroscopy could be used as a molecular detective to understand the crystallinity and bone quality from human primary osteoblasts and osteoblastslike cells. The spectra of both cell lines have shown amide I (1655 cm<sup>-1</sup>), amide III (1248 cm<sup>-1</sup>), C-N stretching (720 cm<sup>-1</sup>), CH bending (985 and 1319 cm<sup>-1</sup>), CH deformation (1448 cm<sup>-1</sup>) and O-P-O stretch (788 cm<sup>-1</sup>) vibrations. Osteoblasts-like cells have explicitly shown tyrosine ring breathing (826 cm<sup>-1</sup>) and O-P-O asymmetric stretching (857 cm<sup>-1</sup>) vibrations. Nucleic acid (DNA/RNA) and O-P-O are higher intensities in osteoblasts-like cells than compared to primary osteoblasts. After 28 days of culture, Raman spectra of osteoblasts-like cells have shown mineralising features and peaks associated with this nature are 1246-1269 cm<sup>-1</sup> (amide III) and 1595-1720 cm<sup>-1</sup> (amide I). Furthermore, the appearance of PO stretch at 960 cm<sup>-1</sup> denotes the inclusion of hydroxyapatite in the extra cellular matrix. Combination of univariate peak analysis and PCA has proved that osteoblasts-like cells have analogous features like bone as well as primary osteoblasts in terms of carbonate-to-phosphate ratio, mineral-to-matrix ratio and crystallinity. This study has contradicted with previous studies and explored Raman as decisive tool for identifying compositional differences between the osteoblasts-like cell line and primary osteoblasts [24].

Nyman et al reported that Confocal Raman Spectroscopy could be used in quantifying differences in compositional properties of osteonal and interstitial bone tissues. This study is based on hypothesis that collagen peaks least affected by the orientation of bone tissue and

demonstrates statistically significant differences in bone composition namely, mineral-tocollagen ratio between osteonal and interstitial tissue. Raman spectra were acquired from the polished surface of the bone tissue with a 785 nm laser diode source with spectral resolution of 1 cm<sup>-1</sup>. Raw peak intensities using custom developed software was obtained, the intensities were calculated for  $v_1$  phosphate at 960–962 cm<sup>-1</sup> ( $v_1PO_4$ ),  $v_2$  phosphate at 431–433 cm<sup>-1</sup> ( $v_2PO_4$ ),  $v_4$ phosphate at 584–589 cm<sup>-1</sup> (v<sub>4</sub>PO<sub>4</sub>), type B carbonate at 1071–1072 cm<sup>-1</sup> (Carb), proline at 855– 857 cm<sup>-1</sup>, amide III at 1247–1248 cm<sup>-1</sup>, CH<sub>2</sub>-wag at 1451–1452 cm<sup>-1</sup>, and amide I at 1666–1667 cm<sup>-1</sup>. They have also calculated 15 peak ratios such as  $v_1PO_4$ / amide I,  $v_2PO_4$ /amide III, v<sub>4</sub>PO<sub>4</sub>/proline, v<sub>1</sub>PO<sub>4</sub>/CH<sub>2</sub>-wag and Carb/v<sub>4</sub>PO<sub>4</sub>, furthermore the inverse of the full width of the  $v_1$ PO4 peak at half-max ( $v_1$ FWHM-1) wherein the maximum intensity was normalized. Results have illustrated peak ratios of m1 phosphate (PO<sub>4</sub>) to proline and m1 phosphate (PO<sub>4</sub>) to amide III calculated to increase highly from 15.4 or 12.5%, respectively, in composition from osteonal to interstitial tissue. The coefficient of variance was below 5% for each as opposed to a value of 8% for the traditional  $v_1PO_4$ /amide I a peak ratio, which was more varied between transverse and longitudinal, cuts of each tissue type. Raman peaks were affected by embedding and it also cannot obscure modification in peak ratios that are related to mineralization between two different tissue types. In further studies with limited sample size but higher number of Raman spectra is most likely to detect a compositional differences among samples, the number of Raman spectra per specimen must be sufficient enough to attain spatial averaging  $v_1PO_4$ /amide III or  $v_1PO_4$ / proline. The  $v_1PO_4$ /proline and  $v_1PO_4$ /amide III ratios basically illustrate the mineral-to-matrix ratio of bone tissue; the ratio is related to degree of mineralization in the matrix overtime. The only explanation could be higher variance in  $v_1PO_4$ /amide I has convincing

dependency of amide I intensity on the orientation of the collagen fibrils in relation to the preferential orientation of the incident laser light polarization [25].

Utzinger et al introduced a Near-Infrared Raman Spectroscopic method for *in vivo* detection of cervical precancers. The main focus of the project was on squamous dysplasia, a precursor of cervical cancer. A pilot clinical trial was carried out at three clinical sites. Raman spectra were measured from one normal and one abnormal area of the cervix. These sites were then biopsied and submitted for routine histologic analysis. Twenty-four measurements were made in *vivo in* 13 patients. Cervical tissue Raman spectra contained peaks in the vicinity of 1070, 1180, 1195, 1210, 1245, 1330, 1400, 1454, 1505, 1555, 1656, and 1760 cm<sup>-1</sup>. The ratio of intensities at 1454 to 1656 cm<sup>-1</sup> is greater for squamous dysplasia than all other tissue types, while the ratio of intensities at 1330 to 1454 cm<sup>-1</sup> is lower for samples with squamous dysplasia than all other tissue types. A simple algorithm based on these two-intensity ratios separated high-grade squamous dysplasia, misclassifying only one sample. Spectra measured *in vivo* resembled those measured *in vitro*. It was believed that cervical epithelial cells might contribute to tissue spectra at 1330 cm<sup>-1</sup>, a region associated with DNA. In contrast, epithelial cells probably do not contribute to spectra at 1454 cm<sup>-1</sup>, a region associated with collagen and phospholipids [27].

Kamemoto et al used near-infrared Raman spectroscopy as molecular marker detective to discriminate between normal and invasive cervical cancer tissue samples. This study has concentrated on the final stage of invasive carcinoma and collected 14 tissue samples from four healthy individuals with no cervical cancer record and three patients with cervical squamous cell carcinoma. The wavelength of the laser used was 785nm to excite both normal and cancer cells. The spectrum of normal squamous cells has shown good amounts of  $\delta$  (CCH) aliphatic of

# <sup>10</sup> ACCEPTED MANUSCRIPT

collagen (816 cm<sup>-1</sup>), ring breathing in Tyrosine & CCH deformation (854 cm<sup>-1</sup>), C-C stretch (922 cm<sup>-1</sup>), C-C skeletal stretch (938 cm<sup>-1</sup>), phenylalanine (Phe) & C-H in-plane bending (1003 cm<sup>-1</sup>), O-P-O backbone stretch of DNA (1101 cm<sup>-1</sup>), amide III (1247 cm<sup>-1</sup>), δ (C=CH) (1273 cm<sup>-1</sup>), CH<sub>2</sub> deformation of lipids (1321, 1450 cm<sup>-1</sup>), DNA (1342 cm<sup>-1</sup>) and α-helix of amide I (1664 cm<sup>-1</sup>). The outcome of this work has shown two specific differences between normal and malignant cells. Firstly, several well-defined Raman peaks of collagen (775 to 975 cm<sup>-1</sup>) were observed in normal squamous cells, but these were absent in invasive cancer cells. Secondly, the amide III (1248 cm<sup>-1</sup>) were present in normal cells, whereas, it is absent in cancer cells. This investigation has also revealed that C-H stretching mode (2800 to 3100 cm<sup>-1</sup>) is six times lower in the factor in cancer cells when compared to normal cells[28].

Gonzalez-Solis et al reported detection of cervical cancer by investigating blood samples with Raman spectroscopy and multivariate analysis. In this study, serum was obtained by fresh blood samples from 20 patients and 10 healthy volunteers and in total 240 spectra was collected from these samples. Among 240 spectra, 80 spectra were collected from 10 control patients, 160 spectra from 10 cervical cancer and 10 early cervical cancer patients. Principal component analysis (PCA) and Linear discrimination analysis (LDA) were performed after removing the fluorescence contribution, smoothing and the baseline correction. Raman spectra have shown clear evidence in peak intensities between normal and cervical cancer states. The peaks of Phenylalanine (1002 cm<sup>-1</sup>) and β-carotenes (1154, 1523 cm<sup>-1</sup>) of the cervical spectrum are higher than the peaks of the control spectrum. This study has also found that peaks at 898, 1615 cm<sup>-1</sup> (Adenine), 1080, 1313 cm<sup>-1</sup> (Tryptophan), 1449 cm<sup>-1</sup> (β-sheet and phospholipids), 1547 cm<sup>-1</sup> (Proline), 1659 cm<sup>-1</sup> (Glutathione), 1396 cm<sup>-1</sup> (β-carotene) and 1765 cm<sup>-1</sup> were present only in

the spectrum of cancer, whereas the peaks at 1266 cm<sup>-1</sup> (amide III) and 1722 cm<sup>-1</sup> were present only in the control spectrum. This study has allowed the biological molecule like adenine, tryptophan, proline, glutathione and β-carotene could also be used to discriminate between normal and cancerous samples [29].

N. Stone et al, for instance, applied NIR Raman spectroscopy for the classification of epithelial cancers and pre-cancers. The aim of their research was to evaluate the use of the technique in interrogating epithelial tissue biochemistry and distinguishing between normal and abnormal tissues. Tissues were selected for clinical significance and to include those, which develop into carcinoma from squamous, transitional or columnar epithelial cells. Rigorous histopathological protocols were followed. The epithelial tissues were obtained from larynx, tonsil, oesophagus, stomach, bladder and prostate. Sensitivities and specificities of up to 100% in separating the samples were obtained [30].

The same research group performed Raman spectroscopic investigations for identification of epithelial cancer. They evaluated the potential for the technique to develop a non-invasive real time probe for accurate and repeatable measurement of pathological samples. The study followed rigorous sample collection protocols and histopathological analysis using a board of expert pathologists. Only the data from sample with full agreement of a homogeneous pathology were used to construct a training data set of Raman spectra. Measurements of tissue specimens from the full spectrum of different pathological groups found in each tissue were made. Diagnostic predictive models were constructed and optimised. High levels of discrimination between pathology groups were demonstrated (greater than 90% sensitivity and

specificity for all tissues). However, it was outlined that larger sample numbers are required for successful implementation of *in vivo* Raman detection of early malignancies [31].

Keller et al employed Raman micro-spectroscopy for discriminating normal cervices of healthy patients versus those of patients with previous disease history. Cervical mapping study of in vitro epithelium and stroma showed spectral signatures for samples containing disease only in epithelial layers. Raman peaks at 1250 cm<sup>-1</sup> and 1400 cm<sup>-1</sup> were found consistently different between health cervix previously diagnosed abnormal cervix and cervix with no history of disease. 1250 cm<sup>-1</sup> peak is associated with collagen hence the spectral difference could be due to small amount of collagenous tissue at left around area at previous disease area. Overall accuracy for determining disease was greater than 99%. Raman can also differentiate normal and diseased and the band intensities were increased at 1334 cm<sup>-1</sup> and 1082 cm<sup>-1</sup> due to DNA content of cell. Increase amount of DNA in diseased suggest enhanced proliferation. Peak intensities of band in the regions from 1000 cm<sup>-1</sup> to 1100 cm<sup>-1</sup> and from 1250 cm<sup>-1</sup> to 1350 cm<sup>-1</sup> are higher in normal tissue. Some of these peak differences are associated with glycogen amount and were reported at 1048, 1083, 1256 and 1333 cm<sup>-1</sup>. It is known that the glycogen in the epithelium decreases with disease, but there is no mention of what happens in the stroma as a result of disease in the epithelium. This study has demonstrated that Raman spectroscopy as a diagnostic tool to detect subtle tissue changes and to identify disease markers associated with cervical cancer [32].

Y.K. Min et al reported on near-infrared 1064nm multi-channel Raman spectroscopy of fresh human lung tissues. Excitation at 785nm failed to detect any Raman bands because of an extremely high fluorescence backbone. As a result, it was confirmed that 1064nm excitation was a requisite for the Raman study of the fresh lung tissue. The observed Raman spectra of lung

tissues made a clear distinction between the normal and cancerous states. It was demonstrated that 1064nm near-infrared multichannel Raman spectroscopy is a feasible tool for in vivo, non-invasive and molecular-level clinical diagnosis of diseases including cancer [33].

S. Kaminaka et al investigated the possibility of molecular-level cancer diagnosis of human lung tissues, using near-infrared Raman spectroscopy. They used a Nd:YAG laser of 1064nm and could collect totally fluorescence-free Raman spectra of normal and cancerous lung tissues. It was concluded that the technique probed lung cancer unambiguously at the molecular level and could be used as a tool for cancer diagnosis [34].

Huang et al employed near-infrared Raman Spectroscopy to study the effect of formalin fixation of normal and cancerous human bronchial tissues. The aim of the study was to find out whether the variations of the Raman spectra caused by formalin fixation would affect the potential diagnostic ability for the lung cancer detection. A rapid dispersive type NIR Raman system with an excitation wavelength of 785nm was used. Bronchial tissue samples were obtained from six patients with known or suspected malignancies of the lung. Raman spectra of fresh normal and tumour tissue were compared with spectra of formalin-fixed normal and tumour tissue. Changes of the ratios of Raman intensities at 1445 to 1655 cm<sup>-1</sup> and 1302 to 1265 cm<sup>-1</sup> versus formalin fixing times varying from 2 to 24hours were also examined. The major Raman spectral peaks were found at 1265, 1302, 1445, and 1655 cm<sup>-1</sup> both in fresh and fixed bronchial tissues. However, bronchial tissues preserved in formalin showed a progressive decrease in overall intensities of these Raman peaks. The results showed that NIR Raman spectra of human bronchial tissues were significantly affected by formalin fixing and tissue hydration. Diagnostic markers at the 980-1100 and 1500-1650 cm<sup>-1</sup> regions derived from fixed tissues did

not appear to be applicable for *in vivo* lung cancer detection. It was shown that for yielding valid Raman diagnostic information for *in vivo* applications, fresh tissue should be used, if only fixed tissue is available thorough rinsing of specimens in phosphate-buffered saline (PBS) before spectral measurements may help reduce the formalin fixation artefacts on tissue Raman spectra [35].

Oshima et al applied Raman spectroscopy is to demonstrate differences among cultures of normal and cancerous lung cell lines. This study has used four different types of lung cancer cell lines namely adenocarcinoma and squamous cell carcinoma with low to medium malignancy and small cell carcinoma and large cell carcinoma with high malignancy. Single cell Raman spectra were obtained by using 532nm excitation wavelength instead of 785 or 633nm. High quality spectra were obtained at 60 sec/cell without any damage. The purpose of this study is to find diagnosis through a suitable Raman marker for lung cancer cell line and their malignancy. The spectra has shown strong band for cyc-c and laser has contributed much resonance in the spectra. PCA was successfully applied and 80% accuracy was achieved in discrimination between cancer lines. Step-wise LDA was performed on these cell lines to identify malignancy type and strain. The cross validation has provided 100% accuracy of discrimination. The current study has shown potentiality of 532nm laser in Raman diagnosis [36].

Li et al has employed Surface Enhanced Raman Spectroscopy (SERS) to detect bio-fluids at molecular level, so that prediction of lung cancer can be possible at early stages. SERS was performed on saliva samples to detect vibrational features of the lung cancer pathology. Raman spectra of control and cancerous sample have shown peaks at 791 cm<sup>-1</sup> (pyrimidine), 906 cm<sup>-1</sup> (tyrosine), 1007 cm<sup>-1</sup> (phenylalanine & carbamide), 1364 cm<sup>-1</sup> (tryptophan) and 1720 cm<sup>-1</sup>

(lipid). The only minute differences such as peak intensities were found between the both spectra. This group has used multivariate analysis such as PCA to extract the main factors and then LDA for the discriminate between both groups. PCA and LDA were successfully employed and 82% total accuracy was achieved. This study has shown promising approach of SERS on detection of lung cancer [37].

Huang et al have described applications of Raman spectroscopy in their review article to chemically characterise different organs of mice. This group has reported no spectral differences between blood pellets and blood. The major Raman vibrations were observed in this study were DNA, Tryptophan, Phosphatidylinositol, RBC, NADH, Phenylalanine, Triglyderides, Glucose, Collagen, Tyrosine, Amide II, Carotene, C-C or C-N stretching of proteins, CH<sub>3</sub>/CH<sub>2</sub> wagging and CH<sub>3</sub>, CH<sub>2</sub> of lipids and proteins. Further studies have demonstrated that Raman bands of 1375, 1590 and 1640 cm<sup>-1</sup> have increased during oxygen saturation. Whole blood spectrum has shown pointed peak at 2330 cm<sup>-1</sup> due to high atmospheric nitrogen and high laser intensity. The spectra of serum have shown vibrations regarding protein, proline, CH<sub>3</sub>/CH<sub>2</sub> wagging, collagen, CH<sub>3</sub>, fatty acids, CH<sub>2</sub>, RBC and Amide I. proline and amide I were observed in serum spectrum but not in whole blood spectrum [38].

Huang et al further reported in their review article about Raman studies of adipocytes, muscle and skin. Adipocytes have shown predominant bands of palmitic acid, Amide I, C550 ester, cholesterol, cholesterol ester, C-C, CH and CH<sub>2</sub> stretch of lipids. This spectrum has shown high resemblance with palmitic acid spectrum, which is one of the most frequent saturated fatty acid present in animal kingdom. Furthermore, these spectra have shown close resemblance with

other saturated fatty acids, such as, lauric and myristic acid. Muscle cells have glycogen as reserve sources

for energy and Raman was applied first time on human muscle cells. The spectra of muscle cells were dominated by tyrosine, proline, Amide III, cholesterol and cholesterol esters. Raman spectra of skin have shown peak intensities corresponding to palmitic acid, adenine, cytosine, Amide I, II & III, CH<sub>2</sub> and CH of lipids and proteins. The spectrum of skin has shown high similarity with adipose cells due to same composition of fat and proteins [38].

This review article has reported Raman fingerprinting of gastrointestinal tract such as stomach, intestine and colon. Raman bands of stomach tissue demonstrated presence of Tyrosine, DNA, polysaccharides, NADH, proline, Amide III. This group further reported Raman studies in gastrointestinal tract including stomach, small intestine and colon. The characteristic Raman peaks of normal stomach tissue were observed at 828, 851, 991, 1044, 1258, 1302, 1442, 1653, 1725, 2139, 2177 and 2917 cm<sup>-1</sup> and there is no study reported in the literature about Raman spectrum of stomach in the high frequency region. The characteristic Raman peaks of normal small intestine tissue were observed at 828, 921, 991, 1044, 1074, 1160, 1258, 1302, 1335, 1442, 1542, 1653, 1725, 2139, 2177, 2870 and 2917 cm<sup>-1</sup> and there is no study reported regarding intestine in the literature till today. The Raman spectra of normal colorectal tissue have shown prominent bands at 1080, 1260, 1300, 1450, 1650 and 1750 cm<sup>-1</sup>. Gastrointestinal tract has shown similar peaks at 828, 1258, 1302, 1442, 1653, 1725, 2136, 2169 and 2917 cm<sup>-1</sup>. These peaks have revealed interesting features of chemical fingerprint of gastrointestinal tract. The peaks at 828 and 1258 cm<sup>-1</sup>, 1302, 1442, 1653, and 2917 cm<sup>-1</sup>, 1725

# <sup>17</sup> ACCEPTED MANUSCRIPT

cm<sup>-1</sup> and 2136 & 2169 cm<sup>-1</sup> were appeared due to protein and DNA, lipids and proteins, lipid and water respectively [38].

This study has also covered Raman progress in urinary bladder, lung and brain. The spectrum of urinary bladder was similar to the gastrointestinal tract. The characteristic Raman peaks were observed at 828, 991, 1044, 1258, 1302, 1442, 1542, 1614, 1653, 1725, 2139 and 2917 cm<sup>-1</sup>. The spectra of both organs have shown similar intensities at 828, 991, 1044, 1442, 1653, 1725, 2139 and 2917 cm<sup>-1</sup>. The Raman spectra of bladder have shown weak intensities at 1258, 1302 and 1542 cm<sup>-1</sup> than that in gastrointestinal tract. The spectral similarities were observed due to common structure of the intestinal wall in both organs. The prominent Raman bands of lung were reported at 800, 991, 1044, 1302, 1335, 1442, 1542, 1590, 1614, 1653, 1725, 2139 and 2917 cm<sup>-1</sup>. A strong peak at 1590 cm<sup>-1</sup> has observed in lungs spectra, but it is not clear that what may be the cause of this. The Raman spectra of brain has shown characteristic peaks at 962, 991, 1044, 1302, 1442, 1542, 1614, 1653, 1725, 2139, 2879 and 2917 cm<sup>-1</sup>. In the spectrum of brain tissue a prominent peak was observed at 2879 cm<sup>-1</sup>, which also appeared in skin and adipose tissue due to lipids and proteins. This peak is believed to be originated from lipids since lipids are so abundant in brain tissue [38].

Nawaz et al reported that Confocal Raman Micro-spectroscopy (CRM) could be used to study the efficacy of chemotherapeutic agent, cisplatin, on A549 adenocarcinoma cells. The aim of this study is to explore chemical changes in cell membrane and cytoplasm of A549 cells after 96 hours exposure to cisplatin. Multiple spectra were obtained from different regions of cell include cell membrane, cytoplasm and nucleus. The spectral data was used to analyse the difference in cellular components and peak changes after cisplatin treatment and multivariate

analysis techniques like PCA, Partial Least Square Regression (PLSR) and PLS jack-knifing were used. This study has identified a band at 726 cm<sup>-1</sup> represented tryptophan as well as CH<sub>3</sub> stretching of lipids and present in a cytoplasm spectrum but not in a nuclear spectrum. Similarly, the Raman peaks at 1423 and 1510 cm<sup>-1</sup> were assigned to CH<sub>3</sub> deformation of aromatic lipids and C=C stretching of tryptophan and tyrosine respectively. These bands were observed predominately in cell membrane and cytoplasm spectra rather than nuclear membrane mean spectra. The effect of cisplatin on the cell membrane spectra has revealed the appearance protein related peaks at 671 cm<sup>-1</sup> and 728 cm<sup>-1</sup> (ring breathing of the tryptophan), 1030 cm<sup>-1</sup> (C-H bending), 1094 cm<sup>-1</sup> and 1126 cm<sup>-1</sup> (C-N stretching) and 1655 cm<sup>-1</sup> (amide I). The Raman bands at 1371 cm<sup>-1</sup> (CH<sub>3</sub> stretching) and 1448 cm<sup>-1</sup> (CH deformation) are related to cell membrane lipids and significant peak shifts were observed at 1371 to 1376 cm<sup>-1</sup> and 1488 to 1450 cm<sup>-1</sup>. They also extracted protein from control and treated Cisplatin cells, and analysed the spectral differences. This group has reported major changes in the Raman bands include an intensification of the 904 cm<sup>-1</sup> and 1131 cm<sup>-1</sup> (C-C skeletal stretching), 1001 cm<sup>-1</sup> (phenylalanine), 1061 cm<sup>-1</sup> (C-N stretching), 1131 cm<sup>-1</sup> and 639 cm<sup>-1</sup> (tyrosine ring breathing), 961 cm<sup>-1</sup> and 1199 cm<sup>-1</sup>, 1011 cm<sup>-1</sup> (tryptophan ring breathing), 1323 cm<sup>-1</sup> and 1404 cm<sup>-1</sup> (CH deformation) and 1606 cm<sup>-1</sup> (C=C bending). PLS Jack-kniffing analysis of cell membrane has demonstrated that cisplatin seems interacting with membrane lipids and caused some changes in their structure. Jack-kniffing results for cytoplasm have suggested that changes in cell physiology in term of ring breathing of tryptophan, RNA and CH bending were observed due to Cisplatin action [39].

Magee et al demonstrated that minifiber optic probe coupled with shifted subtracted Raman spectroscopy could be used to distinguish between *ex vivo* normal from malignant lung tissue. Mini Raman probe was specifically designed for the purpose of working in the channel of bronchoscope and SSRS was specifically designed to reduce fluorescence. A total of seven patients undergoing lung resection for non-small lung cancer were participated in this study. The Raman peak intensities at 1070 (C-C or C-N or C-O), 1300 and 1445 cm<sup>-1</sup> (collagen and phospholipids) was higher in healthy tissues while the peaks at 855, 920, 935, 1002 cm<sup>-1</sup> (phenylalanine) and 1260 (amide III) and 1665 cm<sup>-1</sup> (amide I) exhibit higher intensity in the tumour spectra. Spectral data was analysed using PCA with leave-one-out cross validation. Principle component 5 has classified spectra more precisely to 100% with cut-off score of 0.1. This study was done in *ex vivo* but has shown great prospective for Raman spectroscopy as a real-time diagnostic tool. Although it will require a larger and independent data-base containing set of spectra from malignant and normal tissue in the clinical setting to validate this model [40].

N.J. Kline and P.J. Treado reported on chemical imaging of Breast tissue using Raman spectroscopy. Raman chemical imaging of lipid and protein distribution in breast was performed without the use of invasive contrast agents. Instead, tissue component discrimination was based on the unique vibrational spectra intrinsic to lipids and proteins. It was suggested that visualization of breast tissue components is an essential step in the development of a quantitative Raman 'optical biopsy' technique suitable for the non-invasive detection and classification of breast cancer [42].

Tam et al carried out a study on sample processing techniques of breast cancer using Raman Spectroscopy. Fifty breast biopsies were studied using Raman spectroscopy prior to

receipt of pathology reports. This was applied to at least two of the three available tissue processing techniques using point spectroscopy, mapping, and imaging. Differences in the spectra were related to the various sample processing methods [43].

Haka et al has employed Raman spectroscopy to diagnose benign and malignant lesions in human breast tissue based on chemical composition. This study has used microspectroscopic model of breast tissue which was built upon nine basis spectra. The basis spectra represent the epithelial cell cytoplasm, cell nucleus, fat, β-carotene, collagen, calcium hydroxyapatite, calcium oxalate dihydrate, cholesterol-like lipid deposits and water. This group has developed a diagnostic algorithm for pathological diagnosis with 94% sensitivity and 96% specificity. This study has shown potentiality of Raman spectroscopy in *in vivo* studies to accurately classify breast lesions, thereby reducing number of biopsies [44].

Rehman et al used Raman spectroscopy in their study to examine the biochemical changes taking place within the breast cancer. Spectra of the normal breast tissue were compared with those of the malignant ones. Raman was used to identify chemical changes in different grades of ductal carcinoma *in situ* (DCIS) (Low nuclear grade (LNG), Intermediate nuclear grade (ING) and High nuclear grade (HNG)) and Invasive ductal carcinoma (IDC) (Grade I, Grade II and Grade III) were analysed using Raman spectroscopy. The Raman spectra of normal breast tissue has shown peak at 1662 cm<sup>-1</sup> due to amide I group of proteins. The bands intensity varies with the degree of fatty acid unsaturation and it depends mainly on the lipid to protein ratio. The peak reported at 1442 cm<sup>-1</sup> represents protein assignment of CH<sub>2</sub> and  $v_{as}$ CH<sub>3</sub> of collagen, or a lipid assignment attributed to  $v_{as}$  CH<sub>2</sub>, scissoring, phospholipids, and is of diagnostic significance. The normal tissue has shown weaker intensity than that of IDC tissue in Raman

# <sup>21</sup> ACCEPTED MANUSCRIPT

spectrum, and with increasing grades the intensity of peaks increases, i.e. grade I having the minimum intensity, grade II lying in between and the intensity of grade III considers to be the maximum. The increase in intensity of the OH–NH–CH peaks suggests a change in the lipids, proteins and DNA contents. The absolute intensity of each of the OH–NH–CH peaks in the 3500–2700 cm<sup>-1</sup> region varies with increasing grade (I, II and III), indicating varying concentrations of fatty acyl chains, phospholipids, cholesterol, creatine, proteins, and nucleic acids. There were obvious spectroscopic differences found between the three DCIS grades in both the relative and absolute intensities of absorption bands in the spectra. The spectra from HNG is rich in lipid/acylglycerides and the spectra from LNG is protein-rich, while the spectra from ING contains significant amounts of both lipids/acylglycerides and proteins [45].

Haka et al in their study examined in-vitro fresh-frozen tissues and this study has involved four types of tissue including normal breast tissue, fibrocystic change, fibroadenoma, and invasive carcinoma taken from 126 sites of 58 patients. In order to extract information from the Raman spectra a spectroscopic model was employed. The modelling of the Raman spectrum comprised of fit coefficients that reflect the chemical makeup of the lesion, which was in turn linked with morphological changes that pathologists routinely rely on to diagnose breast cancer. The resulting diagnostic algorithm which classifies tissues not even as benign or malignant, but also according to pathological diagnoses, attained a sensitivity of 94%, specificity of 96% and a total test efficiency of 95% for the diagnosis. In their study, Raman spectra were recorded by using 830nm diode laser with spectral resolution of 8 cm<sup>-1</sup>. The diagnostic algorithm, which was developed earlier, was then applied prospectively to get the Raman spectral diagnoses, which was further compared to traditional histopathology diagnoses. This group has developed

# <sup>22</sup> ACCEPTED MANUSCRIPT

algorithm based on the fit coefficients for fat and collagen. Current algorithm has diagnosed 5 out of 20 DCIS specimen as cancerous, and the remaining 15 DCIS specimens were identified as noncancerous, which includes seven fibrocystic change, seven normal breast tissue and one fibroadenoma. This study has included spectra that recorded from patients who had undergone preoperative chemotherapy. All of these spectra were incorrectly diagnosed by this algorithm. It is clear that other fit coefficients must be incorporated into the algorithm to correctly diagnose DCIS. Studies are presently in progress to expand the diagnostic algorithm to incorporate DCIS[46].

Saha et al applied Raman spectroscopy for detecting microcalcifications in breast tissue based on their chemical composition. Raman spectra were acquired from tissue samples collected through core needle breast biopsy procedures. The algorithm developed to identify microcalcifications was based on model fit coefficients for total calcium, collagen and fat. The spectra of breast biopsies were characterized by the presence of Raman peaks at 912 cm<sup>-1</sup> and 1477 cm<sup>-1</sup> (calcium oxalate) and 960 cm<sup>-1</sup> (calcium hydroxyapatite). This group has detected microcalcifications up to 2150 µm depth in the breast biopsies whereas previous studies were reported maximum transmission depth of only 1mm (1000 µm). This algorithm has positive predicted value (PPV) of 97%, negative predicted value (NPV) of 85% and sensitivity 0f 86% for detection of microcalcifications and this study was not only identified microcalcifications but also distinguished type I microcalcifications from type II [47].

Abramczyk et al has applied Raman imaging to distinguish between normal and cancerous breast tissue. This main aim of this study is not only to avoid histological studies based on biopsies, which are often prone to subjective interpretations, but also improve

biochemical analysis of vibrational properties of tissue. Optical fibres coupled catheters to micro-Raman spectrometer has been used in this study. This Raman images have shown clear differences in carotenoids and fatty acid composition and products of their metabolism between cancerous tissue and surrounding non-cancerous tissue. Spectral data has confirmed that non-cancerous tissue is almost identical to monosaturated oleic acid, which is common component of triglycerides and adipose tissue, whereas cancerous tissue is likely to be dominated by arachidonic acid derivatives mainly cyclic eicosanoids catalyzed by cyclooxygenase. This study has suggested carotenoids and lipids can be used as Raman biomarkers in breast cancer pathology [48-49].

W.T Cheng et al reported on micro-Raman spectroscopy used to identify and grade human skin pilomatrixoma (PMX). The normal skin dermis, collagen type I, hydroxyapatite (HA) were used as control. The Raman spectrum of normal skin dermis was found to be similar to that of collagen type I, confirming that the collagen was a predominant component in normal skin dermis. The most significant differences of the collected spectra of normal skin dermis and soft and hard PMX were the peaks at 1665 cm<sup>-1</sup>, which assigned to amide I band, and 1246 cm<sup>-1</sup>, which assigned toamide III band. The considerable changes in collagen content and its structural conformation, the higher content of tryptophan, and disulfide formation in PMX masses were markedly evidenced. In addition, the peak at 960 cm<sup>-1</sup> assigned to the stretching vibration of PO<sub>4</sub><sup>3-</sup> HA also appeared respectively in the Raman spectra of hard and soft PMX masses, suggesting the occurrence of calcification of HA in the PMX tissue. The results indicated that the micro-raman spectroscopy may provide a highly sensitive and specific method for identifying normal skin dermis and how it differs in chemical composition from different PMX tissues [50].

# <sup>24</sup> ACCEPTED MANUSCRIPT

S. Kaminaka et al reported on NIR multi-channel Raman spectroscopy toward real-time in vivo cancer diagnosis. The method used enabled them to measure an in vivo Raman spectrum of live human tissue (skin) in one minute using fiber probe optics. By applying the system to human lung tissue, they found that Raman spectroscopy makes a clear distinction not only between normal and cancerous tissues, but also between two different parts of lung carcinoma. The results indicated a promising future for the non-invasive real-time Raman diagnosis of cancer [51].

The research of S. Sigurdsson et al was about detection of skin cancer by classification of Raman spectra. The classification framework was probabilistic and highly automated. Correct classification of 80.5%<sup>+-</sup> 5.3% for malignant melanoma and 95.8%<sup>+-</sup>2.7% for basal cell carcinoma was reported, which are excellent and similar to that of trained dermatologists. The results were shown to be reproducible and small distinctive bands in the spectrum, corresponding to specific lipids and proteins, were also shown to hold discriminating information which the used to diagnose skin lesion [52].

Diagnosis of the most common skin cancer, basal cell carcinoma by Raman spectroscopy was carried out by M. Gniadecka et al. Biopsies of histopathologically verified BCC and normal skin were harvested and analysed by NIR-FT Raman spectroscopy using a 1064 nm Nd:YAG laser as a radiation source. The results indicated alterations in proteins and lipids structure in skin cancer samples. Spectral changes were observed in protein bands, amide I (1640-1680 cm<sup>-1</sup>), amideIII (1220-1300 cm<sup>-1</sup>), and v(C-C) stretching (probably in amino acids proline and valine, 928-940 cm<sup>-1</sup>), and in bands characteristic of lipids, CH<sub>2</sub> scissoring vibration (1420-1450 cm<sup>-1</sup>), and -(CH<sub>2</sub>)<sub>n</sub>- in-phase twist vibration around 1300 cm<sup>-1</sup>. Moreover, possible changes in

polysaccharide structure were found in the region 840-860 cm<sup>-1</sup>. Analysis of band intensities in the regions of 1220-1360, 900-990 and 830-900 cm<sup>-1</sup> allowed for a complete separation between BCC and normal skin spectra. In conclusion, Raman spectra of BCC differed considerably from those of normal skin and the technique can be viewed as a promising tool for the diagnosis of skin cancer [53].

A study on confocal Raman Microspectroscopy as a non-invasive *in vivo* optical method to measure molecular concentration profiles in the skin was carried out by Caspers et al. It was shown that how the technique can be applied to determine the water concentration in the stratum corneum as a function of distance to the skin surface, with a depth resolution of 5µm. The resulting *in vivo* concentration profiles were in qualitative and quantitative agreement with published data. No other non-invasive *in vivo* technique exist that analysis of skin molecular compositions as a function distance to the skin surface with similar detail and spatial resolution [55].

Larraona-puy et al have employed Raman microspectroscopy (RMS) in order to access its accuracy in detection and imaging basal cell carcinoma (BCC). This automated evaluation was carried out on skin tissues excised during Mohs micrographic surgery (MMS) and skin surgery. A spectral database was developed using 329 tissue regions from 20 patients and it was used to construct the multivariate classification model. The model has classified the spectra of BCC, dermis or epidermis. Collagen type I spectral features has mainly contributed to differentiate between dermis and BCC. On the other hand, DNA peaks provided evidence in discrimination of BCC from epidermis. Healthy dermis was characterised by proline and C-C backbone vibrations of proteins. This study has shown high sensitivity and specificity in

# <sup>26</sup> ACCEPTED MANUSCRIPT

discrimination of normal healthy tissue from BCC. Moreover, this approach has developed two dimensional biochemical images by using supervised models, which further supported the positive and strong correlation with histopathological detection [56].

Cartaxo et al reported FT-Raman spectroscopy could be used to differentiate cutaneous melanoma from pigmented nevus. Spectral measurements were recorded from normal, neoplastic and pigmented nevi tissues by using Nd:YAG 1064nm laser with spectral resolution of 4 cm<sup>-1</sup>. A total of 140 spectra from neoplastic, 105 from normal tissue and 126 from pigmented nevi were collected. Raman spectra were first pre-processed by correcting the baseline and performing the vector normalization using the Minitab software. The model of variance analysis with a constant factor was used at first phase, and this indicated that all variables showed an affiliation with their own group. In the next phase of the statistical study, a discriminating analysis was performed. The result of this analytical approach has demonstrated a significant differentiation between the three groups. Significant differences were found in the region of 800-980 cm<sup>-1</sup>. Peaks at 855 and 937 cm<sup>-1</sup> represent characteristics of the collagen spectrum. These peaks were reported due to the presence of proline and C-C stretching vibrations of protein structure. The Raman peak shifts were observed from 1540-1620 cm<sup>-1</sup> and 1040-1100 cm<sup>-1</sup> and this corresponded to DNA's vibrational mode. Increase of spectral intensity was reported in primary melanoma and it represents the increased duplication of genetic material that responsible for the proliferation of malignant cells. The discriminatory analysis has demonstrated 75.3% of efficiency in the differentiation among normal, neoplastic and pigmented nevi groups [57].

# <sup>27</sup> ACCEPTED MANUSCRIPT

Larraona-puy et al further reported that RMS could be used to discriminate between hair follicle and BCC in excised skin tissue explants during MMS. Spectral differences were observed among epidermis, BCC and hair follicle. Raman spectral data of hair follicles was very similar to epidermis, While BCC spectral data was dissimilar and has shown high amount of DNA. Spectral differences have clearly differentiated between hair follicles and BCC. This study has developed LDA-model, which is based on supervised Raman band selection. This approach has diagnosed BCC with 90 +/- 9% of sensitivity and 85 +/- 9% of specificity. It was also used to generate automated Raman spectral images and provide diagnosis for new tissue sections containing BCC, dermis, epidermis and hair follicles. Raman spectral images can differentiate hair follicles due to higher amount of nucleic acids than the external epithelial layer spectra. These images have reported excellent correlation with H&E images [58].

Wang et al developed a non-invasive system that combined two modalities including Raman spectroscopy and confocal microscopy, to analyse a cutaneous murine tumour model *in vivo* in terms of microstructures at different depths. A total 494 Raman spectra were recorded from 24 tumour bearing mice *in vivo* so as to assess the Raman spectral differences between different skin layers. The spectral changes involved in the epidermis, dermis, normal peritumoural skin and skin immediately overlying subcutaneous tumours have analysed in this study. The mean normalised Raman spectra of epidermis skin showed strong bands at 1061, 1128 and 1296 cm<sup>-1</sup> due to ceramide whereas dermal spectra showed 855 and 937 cm<sup>-1</sup> peaks due to the presence of collagen. The skin tumours mean spectrum has higher intensities for the peaks at 724 and 1093 cm<sup>-1</sup> and the band at 1325-1330 cm<sup>-1</sup>, which occur from nucleic acids, pointing out a higher density of cells or nuclei in the tumour. Normal and tumour skin tissues have shown

clear spectral differences in phenylalanine, proline and fatty acids absorptions. Multivariate data analysis techniques such as PCA and LDA were used to analyse Raman spectra. This study has established sensitivity of 95.8% and specificity of 93.8% for tumour diagnosis. However, micro-Raman system has the potential to demonstrate much higher accuracy in detecting specific spectral biomarkers and significantly improve the clinical diagnosis of different skin diseases [59].

Konig et al carried out multiphoton autofluorescence/second harmonics generation (SHG) and Coherent anti-Stokes Raman Scattering (CARS) tomography on skin biopsies not only to detect biochemical changes but also to explore tissue architecture, intra-tissue cell morphology and accumulation of various products of pharmaceutical and cosmetic industries. The combination of these multiple techniques has produced hybrid tomogram, which has provided valuable information about outer most skin layer. Distribution of keratin and polygonal patterns of intracellular lipids in stratum corneum have revealed in this study. *In vivo* CARS was used to study diffusion pattern of water and oil on the skin. This study has suggested partial accumulation of oil at the skin fold boundary while water was distributed within the tissue and the lipid free fold regions. CARS was used to distinguish differences between normal healthy skin and psoriasis skin. CARS image has revealed that corneocytes of healthy skin was always surrounded by bright lipid structures whereas pathological skin lacked such structures and the intracellular space were appeared dark [60].

De Oliverira et al applied FT-Raman spectroscopy to discriminate between primary and metastatic cutaneous melanoma, aiming towards a differential diagnosis. This study has analyzed fragments of normal skin, cutaneous melanoma and lymph nodal metastasis. Nd:YAG laser of

1064nm was used as excitation source for FT-Raman spectral recording. Melanoma spectrum has shown decrease in the Amide I peak with spectral area distortion between 1640 cm<sup>-1</sup> and 1670cm<sup>-1</sup> due to alterations in proteins molecular composition. Melanoma spectra has shown increased intensities at 1475 to 1640 cm<sup>-1</sup> (Proteins and lipids), 1200 to 1300 cm<sup>-1</sup> (amide III and lipids) and 1300-1400 cm<sup>-1</sup> (melanin), and decreased intensities at 920 to 980 cm<sup>-1</sup> (protein). Although DNA vibrational mode peak shifts were observed at 1540 to 1620 cm<sup>-1</sup> and 1040 to 1100 cm<sup>-1</sup> in both primary and metastatic melanoma, but metastatic group has shown higher intensities due to increase in nucleic acids and mitosis. Metastasis group has shown decrease in amide I intensities and increase in melanin, amide III, protein and lipid intensities compared to primary melanoma group. This study has made foundations to establish FT-Raman research in the diagnosis of cutaneous melanoma *in vivo* [61].

Design of auto-classifying system and its application in Raman spectroscopy diagnosis of gastric carcinoma was investigated by Tan et al. They developed a tentative user-friendly auto-classifying system to classify Raman spectra of gastric carcinoma tissues. They also suggested that the software could be applied into classifying of other tissues by some necessary alterations [62].

Shetty et al have demonstrated the potential of Raman spectroscopy for the identification and classification of the malignant changes in oesophageal carcinomas. It was aimed to understand the biochemical changes that distinguish between the different stages of disease through Raman mapping studies. This technique was used to analyse 20µm sections of tissue from 29 snap-frozen oesophageal biopsies. Contiguous haematoxylin and eosin sections were reviewed by a consultant pathologist. Changes were noted in the distribution of DNA, glycogen, lipids, and

proteins. The main spectra obtained from selected regions demonstrated increased levels of glycogen in the squamous area compared with increased DNA levels in abnormal region. It was concluded that Raman spectroscopy is a highly sensitive and specific technique for demonstration of biochemical changes in carcinogenesis, and there is potential for in vivo application for real-time endoscopic optical diagnosis [64].

Feng et al recently reported SERS on blood plasma analysis for nasopharyngeal cancer detection. In this investigation, the application of SERS spectroscopy in combination with multivariate analysis was explored for non-invasive gastric cancer detection. This study has revealed significant SERS spectral differences between normal and tumour samples. Primary SERS bands at 494, 589, 638, 725, 813, 886, 1004, 1075, 1134, 1207, 1330, 1445, 1580 and 1653 cm<sup>-1</sup> were all observed in both normal and tumour blood plasma having the strongest intensities at 494, 638 and 1134 cm<sup>-1</sup>. The SERS peaks normalised intensities at 494, 589, 638, 813 and 1134 cm<sup>-1</sup> were more intense for normal plasma than for tumour plasma, whereas SERS peaks at 1330, 1445 and 1580 cm<sup>-1</sup> were higher in gastric cancer plasma samples. The SERS band at 1445 cm<sup>-1</sup> corresponded to the C-H bending mode of collagen or phospholipids, and was higher in cancer plasma than in normal plasma. The SERS band at 1580 cm<sup>-1</sup> corresponded to the C= C bending mode of phenylalanine, where the percentage signals were significantly increased in cancer patient plasma, pointing out an increase in the percentage of phenylalanine content relative to the total SERS-active components in the plasma of gastric cancer patients. Multivariate approaches such as PCA and LDA have differentiated gastric cancer normal samples with diagnostic sensitivity of 79.5% and specificity of 91%. This study has revealed

great promise for developing SERS plasma analysis for non-invasive detection and screening of gastric cancers [65].

Chen et al reported that combination of Raman spectroscopy and multivariate approach can improve diagnosis of nasopharyngeal carcinoma detection. Classification algorithms like PCA, LDA, Bayesian classification (BC) and Mahalanobis distance (MD) were used to improve better classification from normal to cancerous tissues. Raman spectra were collected from nasopharyngeal tissue biopsies and analysed using 785 nm diode laser. Spectral variations between normal and cancer were relatively small but relative peak intensities of normal verses cancer have shown increased amounts of collagen and nucleic acid content. Chemometric approaches have separated cancer spectrum from normal with highest sensitivity, specificity and overall diagnostic accuracy of 98%, 99% and 99% respectively [119].

Kawabata et al reported that near-infrared multichannel Raman Spectroscopy (RAS) could be used as potential diagnostic tool in gastric malignancies. This study has used 1064 nm laser to distinguish non-neoplastic samples from cancer lesions, which were surgically resected after diagnosis of Gastric Cancer. A total of 213 Raman spectra were obtained from both types of samples. PCA was performed and 10 PCs were considered further discrimination analysis. The PCA based diagnostic algorithm yields a sensitivity and specificity of 73% and overall accuracy of 72% for detecting cancer. PCA resulting discrimination algorithm has attained a sensitivity of 98%, specificity of 84% and overall accuracy of 93% for discriminating early cancer from advanced stages. This unsupervised algorithm yields sensitivity of 95%, specificity of 100% and overall accuracy was 98% for distinguishing differentiated cancer from undifferentiated cancer.

This study might be helpful for physicians, who perform complete endoscopic submucosal dissection as well as in endoscopic treatment [66].

Su et al applied Raman confocal micro-spectroscopy to detect biochemical variations between normal and malignant oral tissues and normal and oral squamous cell carcinoma cells. Spectral profiles of normal and malignant samples have shown many marked differences and multiple Raman markers were identified in this study. These markers were mainly associated with DNA and protein vibrational features to distinguish between normal and cancerous samples. PCA was performed to reduce the number of parameters needed to represent the variance and the new principle component scores were representing the maximum variance in the data. The most pronounced differences were observed in the range of 700 to 1800 cm<sup>-1</sup>. The Raman spectra of normal tissue have shown peaks at 756 and 1546 cm<sup>-1</sup> corresponding to tryptophan and Phenylalanine at 1004 cm<sup>-1</sup> was observed both in normal and malignant samples. The malignant tissue display Raman peaks at 1341 and 1655 cm<sup>-1</sup>, which corresponds to adenine and guanine of DNA and amide I of protein respectively. The essential findings of this work have proven that Raman spectroscopy offers enormous potential in distinguish between normal and malignant lesions and it can assist histopathologists in a great way [67].

Kendall reported that novel confocal Raman probe design technology could be used as potential optical biopsy targeting tool in diagnosis of oesophageal adenocarcinoma. This group has developed Raman classification model in their previous study. Model was based on the discrimination of nine pathological groups namely normal squamous epithelium, cardiac type mucosa, fundic type mucosa, intestinal type Barrett's, low-grade dysplasia, high-grade dysplasia, adenocarcinoma, squamous dysplasia and squamous cell carcinoma. A total 1304 Raman spectra

were collected from 123 oesophageal biopsy samples, which were grouped into normal, low risk (Barrett's oesophagus) and high risk (dysplasia and cancer) using 830nm laser excitation source. A training model was developed using 590 spectra measured with an acquisition in 10 seconds. This model has shown sensitivity of 71-81% and specificity of 81-98%. The classification ability of the 2 second spectra has yield of 66-81% sensitivity and 80-98% specificity. When this 2 second spectra were projected on training model, it has a yield of 66-84% sensitivity and 81-96% specificity. This study has found remarkable number of false negatives, where high-risk samples are misclassified as either normal or low risk groups. This study was able to successfully differentiate between normal and other tissue, although there is considerable variance among low to high-risk group. Optical biopsy probe is an endoscopic equivalent tool that provides high signal to noise spectral information in clinically setting with minimally time consumed. Current endoscopic procedure requires multiple biopsies that can be reduced substantially also the Raman probe can facilitate targeted excisional biopsy in oesophageal cancer [69].

Lloyd et al reported that *ex vivo* Raman confocal fibre-optic probe could be useful in improving diagnosis standard of oesophageal cancer. Raman spectra were collected from tissue biopsies using an 830 nm diode laser. This study has used semi-supervised learning approach such as semi-supervised LDA (ssLDA) to discriminate between different grades of oesophageal cancer grades. The aim of this study is to identify diagnostic accuracy of non-consensus samples from true pathological biopsies, which were determined by LDA model. Significant sensitivity and specificity were achieved in discrimination among intestinal metaplasia, dysplasia and low-grade dysplasia. This current study has proved that application of chemometrics not only increase

disease classification performance but also allow larger training data sets to develop more robust diagnostic models [120].

L. Max Almond et al employed endoscopic Raman spectroscopy (ERS) for diagnosis of adenocarcinoma and esophageal high-grade dysplasia (HGD). Raman spectra were collected from *ex vivo* esophageal tissue biopsies using Raman probe provided with 830nm laser resource. Raman has successfully differentiated from epithelial and mucosal disease samples with sensitivity of 96% and specificity of 92%. LDA trained classification models have detected HGD and esophageal adenocarcinoma with sensitivity and specificity of 86% and 88% respectively. The results based on this study have proved that ERS could potentially as rapid objective in *in vivo* diagnosis near future [121].

Lakshmi et al conducted a Raman study on radiation damage of brain tissue in mice. A set of studies were carried out on brain tissue from mice subjected to irradiation to identify the biochemical changes in tissue as the result of radiotherapy and radiation injury. It was shown that brain irradiation produces drastic spectral changes even in tissue far removed from the irradiation site. The changes were very similar to those produced by the stress of inoculation and restraint and the administration of an anaesthetic drug. While the changes produced by stress or anaesthetics last for only a short time (a few hours to 1 or 2 days), radiation induced changes persist even after one week. The results also supported the hypothesis that various protective factors are released throughout the body when the central nervous system (CNS) is exposed to radiation [70].

Human brain tissue, in particular white matter, contains high lipid content. These brain lipids can be divided into three principal classes: neutral lipids including the steroid cholesterol,

phospholipids, and sphingolipids. Major lipids in normal human brain tissue are phosphatidylcholine, phosphatidylethanolamine, phosphatidylserine, phosphatidylinositol, phosphatidic acid, sphyngomyelin, galactocerebrosides, gangliosides, sulfatides, and cholesterol. Minor lipids are cholesterolester and triacylglycerides. A detailed research on Near-Infrared Raman spectra was carried out by Krafft et al. They recorded the Raman spectra of 12 major and minor brain lipids with 785nm excitation in order to identify their spectral fingerprints for qualitative and quantitative analysis [71].

Sato et al reported that Raman spectroscopy could be used to detecting molecular changes occurring due to physiological changes in living brain tissue in situ. This study has used near-infrared Raman system equipped with Raman probe which is made up of ball lens hollow fibres and Ti:sapphire laser. 785 and 720 nm excitation wavelength was used to obtain Raman spectra in fingerprint region (600-1800 cm<sup>-1</sup>) and high-wave number region (2600-3800 cm<sup>-1</sup>) respectively, in order to avoid the low-sensitivity range (>1000nm) of the CCD detector. The aim of this study is to identify protein and lipid alterations, and water cluster conformation under different conditions namely inhalation of sodium pentobarbital (SP), diethyl vapour (DE) and after euthanasia. The spectra of SP treated have shown peaks at 1664, 1446 and 1003 cm<sup>-1</sup> are consigned to the amide I, CH bending and phenylalanine respectively. The spectra of DE treated have shown peaks at 2846, 2881, and 2928 cm<sup>-1</sup> are associated to the CH stretching modes of the protein and lipid groups. The peak at 3453 cm<sup>-1</sup> associated to water cluster species and it denotes that the change in conformational clusters due to the inhalation of DE. The intensity of the water band has decreased approximately 7.7% in the spectrum obtained after euthanasia. This study has provided new insight for Raman approach to carry further analysis in conscious animals [72].

Kohler et al reported that Raman spectroscopy could be used to characterize the biochemical changes in lipid extracts of the brain tumors. This study has used fresh porcine brains, glioblastoma multiforme (GBM) tissue and healthy brain tissue for Raman investigation. The spectra of porcine brain have shown Raman peaks at 720 and 878 cm<sup>-1</sup>, which corresponds to choline group of Phosphatidylcholine and sphingomyelin. While the bands near 1087 cm<sup>-1</sup> are consigned to phosphodioxy group present in phospholipids and in sphingomyelin. Differences in porcine gray and white matter were observed at peaks 1268 and 1660 cm<sup>-1</sup>, which assigned to unsaturated fatty acids whereas, Raman peaks at 430, 546, 608, 701 and 1440 cm<sup>-1</sup>, which corresponds to Cholesterol content. Fatty acid unsaturation was predominant in gray matter whereas high cholesterol content was reported in white matter. Lipid extracted from GBM was analysed using Raman spectroscopy, the intensity ratios of the bands at 720 and 701 cm<sup>-1</sup>, which Phosphatidylcholine and cholesterol respectively. The intensity ratio of Phosphatidylcholine and cholesterol bands has increased in GBM compared to healthy brain. Raman spectra of GBM illustrated increased intensities at 1159 and 1527 cm<sup>-1</sup> that are assigned to carotenoids that have also formerly been identified in Raman spectra of brain tumours. The lipid composition and lipid content are correlated with the tumor grade and this approach has shown great prospect towards the diagnosis of brain tumours [73].

Kirsch et al has demonstrated that Raman imaging could be used to study inter-cerebral tumours. Brain tissue sections, pristine brain tissue and whole mouse brain *ex vivo* were used to examine cerebral pathology through *in vivo* Raman mapping to localize cerebral brain metastases. Spectral band near 2933 cm<sup>-1</sup> is associated with vibrations of CH<sub>2</sub> and CH<sub>3</sub> moieties in proteins and lipids. Other spectral bands of normal brain tissue slightly differ in the intensities

of valence vibrations of OH bonds near 3245 and 3245 cm<sup>-1</sup> that are mainly allocated to water. Most prominent bands are allocated to the aromatic amino acid phenylalanine (1004 cm<sup>-1</sup>), unsaturated fatty acids (1267 and 1661 cm<sup>-1</sup>), CH<sub>2</sub> and CH<sub>3</sub> deformation vibrations (1301 and 1445 cm<sup>-1</sup>), and the amide bands of protein backbones (1267 and 1661 cm<sup>-1</sup>) that overlap with spectral contributions of fatty acids. The Raman spectrum of the midline contains additional peaks due to oxygenated haemoglobin near 750, 1002, 1212, 1546, 1605 and 1619 cm<sup>-1</sup>. Raman spectra of the tumour demonstrate spectral contributions due to melanin near 597, 976, 1404 and 1595 cm<sup>-1</sup>. The melanin pigment was expressed by tumour cells and it can be used as an inherent marker of these brain metastases. Hence further development in nonlinear Raman spectroscopy associated fibre probe research can increase the prospect of Raman spectroscopy as a diagnostic tool for localize and metastatic diagnosis of various primary organs in mice [74].

Tay et al reported first Raman spectroscopic signature of the brain, using motor cortex from acute mouse brain injury. In this study the injury was mechanically initiated in the motor cortex through a cranial window and Raman was performed on the healthy and injured motor cortices immediately after the whole brain was isolated from the skull. A comparative study has shown several common peaks at 1002, 1090, 1130, 1274, 1450 and 1660 cm<sup>-1</sup> in the fresh and fixed tissue whereas the Raman bands at 1003 cm<sup>-1</sup> (C-N stretch of phenylalanine) and 1740 cm<sup>-1</sup> (lipid carbonyl stretch) is consistently different between the both samples. Characteristic amide I vibration at 1660 cm<sup>-1</sup>, one of the most foremost features observed from all healthy brain tissues, was much weaker in the spectra reported from the injured brain tissues. Spectral data from injury showed the band at 1002 cm<sup>-1</sup> (phenylalanine). It was observed that it was either weak or absent peak, as compared to the strong feature in undamaged hemisphere. In addition to above peak,

this group also noticed peak structure in the region of the amide III vibration and two additional bands at 1175 and 1227-1740 cm<sup>-1</sup> are observed in spectra obtained from the injured site. The spectral fingerprint obtained from Raman was further complemented by neurobiological and immuno-histochemical experiments. These results have established possible correlation between new Raman peaks and caspase 3 associated mitochondrial cellular apoptosis. Multivariate analysis such as PCA and LDA will facilitate in further investigation of biochemical differences related with brain injury [75].

R. Malini et al worked on discrimination of normal, inflammatory, pre-malignant and malignant oral tissue using Raman spectroscopy. Spectral profiles of different samples showed pronounced differences between one another. It was demonstrated that all the four tissue types could be discriminated and diagnosed correctly. The biochemical differences between normal and pathological conditions of oral tissue were also discussed [76].

Application of FTIR fiber-optic technique for distinguishing malignant from normal oral tissues was reported by J.G. Wu et al. According to the results, the 1745 cm<sup>-1</sup> band, which is assigned to the ester group (C=O) vibration of triglycerides, is a reliable marker that is present in normal tissue but absent or weak band in malignant oral tissues. In addition, other bands such as C-H stretching and the aide bands are also helpful in distinguishing the two groups of samples. Raman spectroscopic measurements were in agreement with results observed from FTIR spectra [77].

In another work, Lau et al studied on Raman spectroscopy for optical diagnosis of the larynx. The objective of the research was to determine if Raman spectra could be obtained rapidly from laryngeal tissue in vitro, and compare Raman spectra from normal, benign and

cancerous laryngeal tissue. Good quality spectra were obtained with five second signal acquisition time (SAT). Spectral peak analysis showed prediction sensitivities of 89%, 69%, and 88%, and specificities of 86%, 94%, and 94% for normal tissue, carcinoma and papilloma. Spectral differences appeared to exist between different samples and it was concluded that the ability of obtaining the spectra rapidly supports potential for future in vivo studies [78].

A Fourier transform near infrared (FT-NIR) Raman spectrometer was used in the present research, in order to detect samples of oral mucosa, leukoplakia and squamous cell carcinoma. Normal oral mucosa was acquired from squamous cell carcinoma patients and was characterised into groups by pathologist. Raman spectra were recorded by using Nd:YAG laser (1064 nm) with a resolution of 8 cm<sup>-1</sup>. Support vector machine was employed to classify the Raman spectra of different groups and to establish discriminating model. The efficiency of this algorithm was evaluated by its specificity, sensitivity, accuracy, Matthew coefficient correlation and rigidity. Raman spectra of squamous cell carcinoma has shown Peaks at 747, 897, 939, 1060, 1125 and 1610 cm<sup>-1</sup> corresponding to CH<sub>2</sub> rocking, C-C skeletal stretching, C-C stretching, C=C bending in phenylalanine and tyrosine, C-N stretching in phenylalanine and Amide I respectively. The difference between the mean spectra was relatively small in normal mucosa and leukoplakia. Also, by comparing with subtracted mean spectrum of normal mucosa and squamous cell carcinoma, the peaks were not so noticeable in the background noise. The primary purpose of this model was able to differentiate correctly between the two classes of spectra and, FT-NIR-Raman and this algorithm has successfully separated squamous cell carcinoma from normal mucosa. The efficiency of this model in discriminating the normal tissue and leukoplakia was lower, but further elimination of low-grade hyperplasia dataset, the accuracy and rigidity of the

model improved. This might be due to less proliferative nature of leukoplakia and the difference in biochemical fingerprinting between leukoplakia and normal mucosa was not as significant as that between squamous cell carcinoma and normal mucosa. Therefore, by using these approaches in a combination demonstrated great potentiality towards detection. This investigation provides a research-based and theoretical foundation for developing a real time, trauma-free and accurate diagnostic strategy for oral mucosal lesions[79].

The major aim of this Raman investigation is to assess the biochemical variations and inter-anatomical variations of different normal tissues in the oral cavity. Bergholt et al has studied different tissue sites in the fingerprint region of in vivo Raman spectra. The measurement sites, which were predefined, were total eight in number with distinctive anatomical locations in the oral cavity including hard palate, soft palate, buccal, inner lip, attached gingiva, floor, anterior dorsal tongue and ventral tongue. This research work has identified distinct Raman bands, which are highly associated with proteins, DNA, lipids, and bone/tooth minerals. There were marked differences in the spectral properties among the various anatomical sites. Raman peak intensity changes, especially for the Raman bands at 820, 853, 936, 956, 1070, 1265, 1302, 1450, 1575, 1670, and 1745 cm<sup>-1</sup>, reconfirmed that the oral tissue indeed is relatively complex. A semi-quantitative spectral modelling was employed which was based on non-negativityconstrained least squares minimization and partial least squares-discriminant analysis, for the evaluation of inter-anatomical variability and to render multiclass algorithms for clusterings of different tissues in the oral cavity. For multiclass classification, partial least squares-discriminant analysis was employed and the clustering dendrogram has divided into three major clusterings, namely, (1) buccal, inner lip, and soft palate; (2) dorsal, ventral tongue, and floor; (3) gingiva

and hard palate. A range of difference in spectra along with these algorithms revealed that interanatomical variability is significant and it should be considered as an important parameter in the interpretation and rendering of diagnostic decision on oral tissue diagnosis and characterisation [80].

Lau et al reported on Raman spectroscopy for optical diagnosis in normal and cancerous tissue of the Nasopharynx. The tissues obtained from biopsies were studied using a rapid acquisition Raman spectrometer. The spectra were collected in five seconds and consistent differences were noted between normal and cancerous tissue in three bands of 1290-1320, 1420-1470, and 1530-1580 cm<sup>-1</sup> [81].

Raman spectroscopy was used to quantify the cellular activities such as monitoring of the biomaterial during fabrication in tissue engineered *ex vivo* model. Lo et al reported that Raman can be successfully used as real-time monitoring tool to understand keratinocytes maturation during fabrication process. Raman spectra were taken from human normal oral mucosa and the corresponding tissue engineered *ex vivo* model with a confocal Raman spectroscopy system with a 632 nm, 18-mW He -Ne laser. The normal human keratinized oral mucosa Raman spectrum has shown weak amide I peak at 1650cm<sup>-1</sup>, the strong CH<sub>2</sub> deformation peak at 1440 cm<sup>-1</sup>, broad peaks in the amide III at 1200–1350 cm<sup>-1</sup>, broad C–OH peak at 1080 cm<sup>-1</sup> and the sharp phenylalanine peak at 1655 cm<sup>-1</sup>, a strong CH<sub>2</sub> deformation peak at 1440 cm<sup>-1</sup>, broad peaks in the amide I peak at 1655 cm<sup>-1</sup>, a strong CH<sub>2</sub> deformation peak at 1440 cm<sup>-1</sup>, broad peaks in the amide III at 1200 – 1350 cm<sup>-1</sup> region, a broad C-OH peak at 1080 cm<sup>-1</sup> and the sharp phenylalanine peak at 1001cm<sup>-1</sup>. A credible linear regression of the amide I/phenylalanine peak

ratio of the tissue engineered *ex vivo* model at different cultivating days with different maturation stages has been observed. The stable peak intensity of the phenylalanine band at 1004 cm<sup>-1</sup> could be explained by the active catalysis of phenylalanine by viable keratinocytes grown on the tissue engineered *ex vivo* model. This study has established Raman as a good quantitative marker for understanding maturation process of the three- dimensional constructs [82].

X. Li et al applied Raman spectroscopy and fluorescence for the detection of liver cancer and abnormal liver tissue. They measured laser induced human serum raman spectra of liver cancer and analysed the spectral differences between normal people and liver cancer patients. The results from more than two hundred case measurements showed that the spectral diagnosis was in good agreement with the clinical results. The experiment indicated that the blue shift of fluorescence peak difference between the normal, liver fibrosis and liver cirrhosis [83].

Guo et al reported that Raman Spectroscopy could be used to differentiate malignant hepatocytes from normal liver cells. In this study, the research was focused on exploring whether Raman spectroscopy associated statistical analysis method, is capable to categorise normal and malignant hepatocytes with a high accuracy, and attain more about the spectral differences between the normal and malignant hepatocytes. The statistical methods such as T-test, PCA and LDA were used to analyze the Raman spectra of both cell lines. The mean Raman spectra of normal and malignant cells in the region of 600–1800 cm<sup>-1</sup> showed that the strong bands at 1447 and 1656 cm<sup>-1</sup> can be attributed to the CH<sub>2</sub> deformation mode and the C=C stretching mode of the lipids and proteins, respectively. The band originating at 786 cm<sup>-1</sup> can be assigned to the O–P–O stretching mode of DNA. The bands appearing at 1004 and 1032 cm<sup>-1</sup> can be assigned to the symmetric ring breathing mode and the C-H in-plane bending mode of phenylalanine,

respectively. The T-test was carried out on the nine major bands at 786, 825, 852, 1004, 1230-1280, 1311, 1447, 1585, and 1625-1720 cm<sup>-1</sup>. The results of T-test have confirmed that the intensities of these bands are considerably different between two cell lines, except for the 1585 cm<sup>-1</sup> and 1625-1720 cm<sup>-1</sup> bands. In order to differentiate between normal and malignant hepatocytes, a total fifty spectra were analyzed by PCA and LDA. Ten principal components from PCA were used to feed the LDA model by leave-one-out cross-validation, and then one discriminant function can be obtained. The results visibly demonstrated that the high accuracy of 100% for Raman spectroscopic identification of normal and malignant hepatocytes was based on PCA and LDA [84].

Schie et al employed Coherent Anti-Stokes Raman Scattering (CARS) and Raman Spectroscopy to study dynamic changes of lipid droplets in live primary hepatocytes. A pathologic hallmark of liver injury is an increased accumulation of intracellular lipid droplets within hepatocytes. The laser (Nd:YVO4 1064 nm) was used as the Stokes probe beam to image lipid dynamics in primary rat hepatocytes. Raman spectra of lipid droplets were acquired over the spectral region from 500 to 3100 cm<sup>-1</sup> from variable sized lipid droplets within hepatocytes. This spectrum corresponds to a typical lipid Raman spectrum composed mainly of contributions from C-C, C-H, and C=O bond vibrations. Specifically, the 1266 cm<sup>-1</sup> and 1302 cm<sup>-1</sup> are an inplane 1/4C – H double bond vibration in cis configuration and a CH<sub>2</sub> twisting mode, respectively. The 1446 cm<sup>-1</sup> vibration is a combination of a CH<sub>2</sub> twisting mode and the 1455 cm<sup>-1</sup> CH<sub>2</sub> scissoring mode and its intensity is a good measure of the total lipid content in the droplets. The peak at 1655 cm<sup>-1</sup> is a C=C stretch vibration in the *cis* configuration and represents the degree of hydrocarbon chain unsaturation. The peak at 1742 cm<sup>-1</sup> indicates C=O ester group and it

represents triglyceride esterification within the lipid droplets. Palmitic acid treatment has resulted in an increase in the intensities at 1302 cm<sup>-1</sup> and the 1444 cm<sup>-1</sup>. Additionally, a new peak at 1630 cm<sup>-1</sup> assigned to 13-hydroxy-9,11-octadedecadienoicacid (13-HODE) appeared and the 1656 cm<sup>-1</sup> unsaturated lipid peak decreased considerably. This reduction pointed out that 13-HODE is a important factor leading to the increased accumulation of saturated fatty acids in lipid droplets. Treatment of hepatocytes with a combination of palmitic acid and 13-HODE lead to a stark change of the lipid droplet spectra. The 860 cm<sup>-1</sup> peak disappeared and a new peak at 891 cm<sup>-1</sup> became apparent, and hence corresponding to a CH<sub>2</sub> rocking vibration. These findings made a new insight to combinational approach of CARS and Raman in studying the effects of metabolic disorders and diseases [85].

Movasaghi et al employed Raman spectroscopy to study testicular cancer at cellular level. The aim of this study is to identify spectral differences between sensitive and resistant types of cell lines. Spectra were obtained using different lasers. The sensitive subtype has expressed specific bands at 483 cm<sup>-1</sup> (PO<sub>4</sub><sup>3-</sup> vibration) and 862 cm<sup>-1</sup> (C-C stretching and CCH bending). These are not found in resistant subtypes. PLS-DA algorithm has applied on spectral data to discriminate between these two subtypes. The advantage of this method over other unsupervised approaches is identification of linear combination, which further can be used to LDA analysis. The peaks at 437 and 487cm were selected for ratio classifier in distinguishing between these two cell types. This approach has achieved discrimination accuracy of 96-100%. This approach has provided new insight in understanding the chemical fingerprint of testicular cancer tissues in future studies [86].

Another FT-Raman spectroscopy was carried out on the carcinogenic polycyclic aromatic hydrocarbons (PAHs) in biological systems and their banding to heme proteins, by H.P. Chiang et al. The Raman spectra of benzo[a]pyrene (BaP), a typical carcinogenic PAH, were acquired under different conditions and analysed. It was concluded that CH wagging and ring stretching mixed strongly with CH in-plane bending are the most significantly affected vibrations [87].

It was confirmed that the intrinsic Raman scattering intensity of single-walled carbon nanotubes(SWNTs) does not decay over time. Raman spectroscopy was subsequently used to measure the post injection blood concentration of SWNTs with different polyethylene-glycol (PEG) coatings in mice and therefore glean nanotube blood circulation times. Raman spectroscopy and Raman imaging were also employed in this investigation to probe the biodistribution of SWNTs in various organs of mice ex vivo over a period of several months. It was established that the surface chemistry of nanotubes was critical to their in vivo behaviour. This result was expected due to pristine carbon nanotubes which have very hydrophobic surfaces and are highly nonspecific in binding to biological species. Recently, it was discovered that intravenously injected pristine SWNTs are highly rich in the lung and also in reticuloendothelial systemand remain in mice indefinitely. This hydrophobicity has to be blocked by proper chemical functionalisation such as the PEG coatings, which enables biologically inert SWNTs with long blood circulation, low RES uptake, and relatively fast clearance from organs and excretion from the body. For the *in vivo* behaviour of nanotubes the degree of PEGylation of SWNTs is important. Longer PEG chains, especially those with branched structures, are excellent in affording SWNTs with the most desirable characteristics for in vivo applications. This finding should also be applicable to functionalisation of various other nanomaterials such as

### <sup>46</sup> ACCEPTED MANUSCRIPT

nanocrystals, particles for *in vivo* research. SWNTs detected in the faeces of mice clearly revealed that the biliary excretion pathway. A proportion of nanotubes seemed to be excreted via the renal pathway. In addition, no obvious toxic effect was found in the necropsy, histology, and blood chemistry studies, which warrants the safety of properly functionalised carbon nanotubes for future *in vivo* biomedical applications [122].

S.W.E. Van de Poll et al reported on Raman spectroscopic evaluation of the effects diet and lipid-lowering therapy on atherosclerotic plaque development in mice. Through this technique, they could make quantitative characterisation of the plaque without using the standard destructive histopathological methods such as sectioning. Raman spectra were obtained over the full width and entire length of the ascending aorta and aortic arch. Spectra were modelled to calculate the relative dry weights of cholesterol and calcium salts, and quantitative maps of their distribution were created. In conclusion, Raman spectroscopy could be used to quantitatively study the size and distribution of depositions of cholesterol and calcification. It also could be used for the quantitative investigation of atherosclerosis and lipid-lowering therapy in larger animals or humans in vivo [88].

J. Duarte et al investigated on the use of near-infrared Raman spectroscopy to detect Immunoglobulin G and Immunoglobulin M antibodies against Toxoplasma Gondii in serum samples of domestic cats. The aim of this work was to investigate a new method to diagnosis Toxoplasma Gondii, instead of serological tests which usually have a high cost and are time consuming as well. In conclusion, the possibility of antibody detection by Raman spectroscopy was confirmed [89].

Application of Raman Spectroscopy of serum for cancer detection was investigated by Li et al. The spectra of serum from cancerous and normal individuals were analysed. Three Raman peaks with intensities of 1005, 1156, and 1523cm<sup>-1</sup> were consistently observed from normal blood serum samples, whereas no peaks or only very weak peaks were detected from tumorous cases [90].

Rohleder et al applied Raman Spectroscopy as a tool for predicting the concentrations of different parameters in serum and serum ultrafiltrate. In an investigation using sample from 247 blood donors, the concentrations of glucose, triglycerides, urea, total protein, cholesterol, high density lipoprotein, low density lipoprotein and uric acid were determined with accuracy within the clinically interesting range. After training a multivariate algorithm for the data analysis using 148 samples, concentrations were predicted blindly for the remaining 99 serum samples based solely on the Raman spectra. Relative errors of prediction around 12% were obtained. It was also shown that ultrafiltration can efficiently reduce fluorescent light background to improve prediction accuracy [91-92].

Neugebauer et al further reported that Raman imaging could be used to identification and differentiation of circulating tumour cells from peripheral blood. Circulating tumour cells play an important role in tumour diagnosis and the alteration in these numbers over time can serve as a marker for tumor therapeutic studies. The aim of this study is to identify leukocytes, myeloid leukaemia cells and solid tumor cells by using combination of Raman spectroscopy and statistical approaches. Raman images were collected from dried cell using 785 nm laser with spectral resolution of 4 cm<sup>-1</sup>. The general features of these cells spectra are look very much alike but leukocytes have shown higher intensities. Negative differences can be observed near 780,

### <sup>48</sup> ACCEPTED MANUSCRIPT

811, 851, 1004, 1034, 1302, 1441 and 1656 cm<sup>-1</sup> due to increase in nucleic acid, lipid and amino acid content of cancer cells. Unsupervised statistical method such as hierarchical cluster analysis was applied on vector normalized average spectral region between 1800 and 500 cm<sup>-1</sup>. This analysis was performed by using Euclidean distance method and Ward's algorithm. The resultant dendrogram has well separated leukocytes from other cell types. PCA studies were further supported the clustering results. Supervised approach such as support vector machines was classified the cells with high prediction accuracy of more than 97.7%. This pioneering research could assist not only in early cancer detection but also useful in monitoring cancer therapy [92].

Neugebauer et al applied Raman spectroscopy to detect and identification of tumour cells based on biochemical variation. From the peripheral blood of healthy donors leukocytes and erythrocytes were isolated, whereas myeloid leukaemia cells and breast carcinoma derived cells were obtained from cell cultures. A laser emitting 785 nm light was used for optical trapping the single cells in the laser focus. Raman spectra were acquired from single cells in aqueous medium using a microscopic setup, which acted as optical tweezers. Raman spectra of cells suspended in PBS buffer have shown amide I (1657 cm<sup>-1</sup>), phenylalanine and tyrosine (1605 cm<sup>-1</sup> and 1585 cm<sup>-1</sup>), CH<sub>2</sub> deformation (1450 cm<sup>-1</sup>), amide III (1255 cm<sup>-1</sup>), tryptophan (758 cm<sup>-1</sup>) and PO<sub>2</sub>-backbone vibrations (1094 cm<sup>-1</sup>). Raman spectra of the cancer cells and the leukocytes look very much alike; the Raman spectrum of erythrocytes looks remarkably different from haemoglobin content which gives rise to the prominent sharp bands around 1621, 1584, 1564, 1374 and 755 cm<sup>-1</sup>. In order to develop a classification model for Raman spectra of five cell types in suspension, supervised statistical approach such as support vector machines was used. Differentiation of cancer cells and normal cells from different donors and cultivation batches was

achieved by employing supervised statistical methods with high sensitivity of >99.7% and specificity of >99.5%. Even though the prediction accuracy of 92.4% is slightly lower for the differentiation between different cell types the Raman-based approach also holds promise to determine the cell type and, consequently, the origin of the cancer cells [93]

L Silveira et al reported on the correlation between near-infrared Raman spectroscopy and the histopathological analysis of the atherosclerosis in human coronary arteries." The objective of the study was to obtain feasible diagnostic information to detect atheromatous plaque using NIRS. An 830nm Ti:sapphire laser pumped by an argon was used. A spectrograph dispersed light scattered from arterial tissue and a liquid-nitrogen cooled CCD detector was used to obtain Raman spectra. A total of 111 arterial fragments were scanned and Raman results were compared with histopathology. An algorithm was modelled for tissue classification into three categories: non-atherosclerotic (NA), non-calcified (NC), and calcified (C) using Raman spectra. Spectra were randomly separated into training and prospective groups. It was found that for the NA tissue the algorithm has sensitivity of 84 and 78% and specificity of 91 and 93% for training and prospective groups, respectively. For NC tissue the algorithm has sensitivity of 88 and 90% and specificity of 88 and 83%. For the C tissue both sensitivity and specificity were maximum, 100% [94].

G.J. Puppels et al made an investigation on carotenoids located in human lymphocyte subpopulations (CD4+, CD8+, T-cellreceptor- $\gamma\delta$ + and CD19+) and natural killer cells (CD16+) using Raman Microspectroscopy. In CD4+ lymphocytes a high concentration of carotenoids was found in the Gall body (about  $10^{-3}$  M). In other cell groups, except CD19+ ones, carotenoids appeared to be concentrated in the Golgi complex (about  $10^{-4}$  M). The concentration of

carotenoids in CD19+ lymphocytes was found to be below the present detection limit (about 10<sup>-6</sup> to 10<sup>-5</sup> M). The results provided new possibilities to investigate the mechanisms behind the suggested protective role of carotenoids against development of cancers [95].

Dochow et al employed combination of Raman spectroscopy and optical traps to identify tumor cells in microfluid environments such as saliva, urine or blood. Raman spectra were recorded from individual cells by using optical tweezers and 514nm excitation source. This study has used two optical traps, the first one quartz capillary coupled to a 785nm laser source and second one microfluidic glass chip associated with laser fibres of the optical trap. LDA has classified normal cells and tumor cells, and even identified cell type based on small variations. LDA classification model for quartz capillary-based approach has yielded overall accuracy of 92.2%. The individual accuracy for erythrocytes, leukocytes, breast tumor cells and myeloid leukemia cells were 95%, 97.2%, 94.5% and 94.6%, respectively. The overall accuracy of second approach was 94.9% and LDA has classified myeloid leukemia cells, breast tumor cells and leukocytes with accuracies of 96.3%, 95.4% and 86.2% respectively. Erythrocytes were identified based on their size, shape and pigmentation whereas leukocytes and leukemia cells have shared common ancestry and are closely related to each other [96].

Lin et al has reported confocal micro-Raman spectroscopy to analyze drug effects of paclitaxel on human Burkitt lymphoma cells. In this study, Raman was used to detect structural and functional changes associated with lymphoma cells, which are treated with different concentrations of paclitaxel. Raman spectra were recorded in the range of 300- 1800 cm<sup>-1</sup> by using 785nm diode laser with spectral resolution of 2 cm<sup>-1</sup>. The Raman spectra of control and treated ones have shown clear spectral differences. As the concentration of drug increases, the

band intensities at 1094 cm<sup>-1</sup>(O-P-O symmetric stretching), 1338 cm<sup>-1</sup> and 1578 cm<sup>-1</sup> (adenine and guanine) decrease, which portray the affect of DNA replication due to destruction of DNA bases. On the contrary, the band intensities of O-P-O symmetric stretch (831 cm<sup>-1</sup>), and amide III (1258 cm<sup>-1</sup>) and amide I (1658 cm<sup>-1</sup>) have increased due to possible conformational changes in DNA and protein double helix respectively. Multivariate statistical approaches such as PCA and LDA were performed on Raman data to differentiate lymphoma cells from treated cells. The sensitivity and specificity of the both approaches has increased with increasing doses of drug and this approach went upto 100% with high drug dose. Raman coupled with multivariate approach has proved that 5 μg/ml drug concentration is seemed to be as an effective and appropriate concentration for damaging the burkitt lymphoma cells. This work has shown Raman a great insight to explore cytotoxicity and drug interaction studies in coming future [97].

JL Deng et al have carried out a study on the effect of alcohol on single human red blood cells (RBCs) using Near-Infrared laser tweezers Raman Spectroscopy. A low-power diode laser at 785nm was applied for the trapping of a living cell and the excitation of its Raman spectrum. The denaturation process of single RBCs in 20% alcohol solution was investigated by detecting the time evolution of the Raman spectra at the single-cell level. The vitality of RBCs was characterised by Raman bands at 752cm<sup>-1</sup>, which corresponds to the porphyrin breathing mode. They found that the intensity of this band decreased by 34.1% over a period of 25 minutes after the administration of alcohol. In a further study of the dependence of the denaturation on alcohol concentration, it was discovered that the decrease in the intensity of the 752cm<sup>-1</sup> band became more prominent as the alcohol concentration increased [98].

Bonnier et al reported that combination of Raman maps and vector quantization could be used to study molecular information of single cancer cells. K- means cluster analysis and PCA were successfully differentiated molecular differences among cellular regions such as cytoplasm, nucleus and nucleoli. Initially PCA was applied on pure biomolecular components such as albumin, RNA and histones and scatter plots were correlated with loading points and resulting spectral differences were applied on complex data sets of single cells. The loading plots have provided complex mixture of molecular vibrations regarding lipids and nucleic acids. Pair wise analysis approach has clearly identified sub cellular regions based on biochemical differences[123].

Liu et al employed Raman spectroscopy to study tumor apoptotic interactions between flavonoids and protease inhibitors. Both compounds share common functional features and they are divergent in structural and more of action. Spectra were collected from samples containing natural flavonoids like quercetin and protease inhibitors such as bortezomib and MG-262. Raman has revealed significant stretching and ring vibrational differences between bortezomib and the combination of bortezomib and quercetin at 950 cm<sup>-1</sup> (C-C), 830 cm<sup>-1</sup> (C-O) and 820 – 760 cm<sup>-1</sup> respectively. Spectral differences were at C-O symmetric and C-C twisting between quercetin and MG-262 [99].

C.M. Krishna et al used micro-Raman spectroscopy to investigate randomly mixed cancer cell populations, including human promyelocytic leukaemia, human breast cancer, human uterine sarcoma: as well as their respective pure cell lines. In this study, the efficiency of micro-Raman spectroscopy to identify a cell type in randomly distributed mixed cell population was assessed. According to the results, cells from different origins can display variances in their

spectral signatures and the technique can be used to identify a cell type in a mixed cell population via its spectral signatures [100].

N. Kuhnert and A. Thumser, reported on the use ofRaman Microspectroscopy using Diode laser at 785nm or Argon ion laser 512nm. This technique was employed for detection of vibrationally labelled compounds in living human cells and positive results were obtained. They suggested that future research should concentrate on sensitivity and experimental set-up in order to achieve better detection limits [101].

Chan et al worked on detection of the individual neoplastic and normal hematopoietic cells using Micro-Raman Spectroscopy. The potential application of confocal Micro-Raman Spectroscopy as a clinical tool for single cell cancer detection based on intrinsic biomolecular signatures was demonstrated. They showed that this method can discriminate between different kinds of unfixed lymphocytes, and single-cell Raman spectra provide a highly reproducible biomolecular fingerprint of each cell type. Characteristic peaks, mostly due to different DNA and protein concentrations, allowed to discriminate between normal lymphocytes from transformed ones with high confidence (p<<0.05). The method was shown to have a sensitivity of 98.3% for cancer detection, with 97.2% of the cells being correctly classified as belonging to the normal or transformed type [103].

S Farguharson et al measured the chemotherapeutic drug 5-fluorouracil in saliva using Surface-Enhanced Raman Spectroscopy (SERS). A silver-doped sol-gel provided SERS and also some chemical selectivity. 5-fluorouracil and physiological thiocyanate produced SERS, whereas large biochemicals, such as enzymes and proteins did not, supporting the expectation that the larger molecules do not diffuse through the sol-gel to any appreciable extent. In addition, 5-

fluorouracil samples of  $2\mu g/ml$  were easily measured, and an estimated limit of detection of  $5\mu g/ml$  in 5 minutes should provide sufficient sensitivity to perform pharmacokinetic studies and to monitor and regulate patient dosage [104]

Barhoumi et al reported SERS could be used to detect post-translational modifications of DNA and this study has developed a link between chemical and DNA fingerprinting studies. Single stranded DNA sequences of normal, adenine-methylated and mixture of both DNA with length of 12 bases have been used for spectroscopic studies. Adenine breathing mode at 736 cm<sup>-1</sup> was dominated in normal DNA spectrum and three new peaks at 390, 1100 and 1197 cm<sup>-1</sup> were observed in adenine-methylated DNA due to 6-methyladenine. This study also has identified methylated and hydroxymethylated cytosine and oxidized guanine in purely synthesized DNA. This study has offered SERS as potential promising tool for DNA based diagnostic applications [105].

Characterization of conformational changes on guanine-cytosine and adenine-thymine oligonucleotides induced by amiooxy analogues of spermidine using Raman spectroscopy was accomplished by A.J. Ruiz-Chica et al. These analogues resulted from the substitution of the two terminal aminomethylene groups of spermidine, <sup>+</sup>NH<sub>3</sub>CH<sub>2</sub>, by an amnooxy one, H<sub>2</sub>NO. The spectra demonstrated the existence of strong differences in the oligonucleotide-analogue interactions depending on base sequences. Different spectral features were observed. This fact supported the idea that the two amino terminal groups of spermidine could have different roles in the interaction this biogenic polyamine with DNA [106].

K.J. Jalkanen et al used vibrational spectroscopy to study protein and DNA structure, hydration and binding of biomolecules, as a combined theoretical and experimental approach.

The systems studied systematically were the amino acids, peptides, and a variety of small molecules. The goal was to interpret the experimentally measured vibrational spectra for these molecules to the greatest extent possible, and to understand the structure, function and electronic properties of these molecules in their various environments. It was also believed that the application of different spectroscopic methods to biophysical and environmental assays is expanding, and therefore a true understanding of the phenomenon from a rigorous theoretical basis is required [107].

Zhang et al demonstrated that stimulated Raman scattering (SRS) could be used to live cell imaging of nucleic acids. SRS, a coherent Raman scattering technique, is advantage over CARS in nonresonant background and spectral distortion. This study has shown live cell imaging of two mammalian cell lines namely human embryonic kidney cells and breast cancer cells, and single polytene chromosomes within the salivary glands of Drosophila melanogaster, commonly known as fruit fly. Targeted molecule concentration is linearly propositional to SRS signal that can be used for imaging in the fingerprint region. Two excitation beams (1064 nm Nd:YVO4 laser and 532nm Nd:YVO4 laser) with the frequency difference matching the vibrational frequency of targeted molecules are applied. Due to high amount of DNA concentration, the spectrum of Drosophila melanogaster larvae has shown peaks at 2845 cm<sup>-1</sup> (CH<sub>2</sub> vibration in lipids), 1655 cm<sup>-1</sup> (amide I proteins), 785 cm<sup>-1</sup> (phosphodiester stretch) and 1090 cm<sup>-1</sup> (dioxy stretch of the phosphate backbone). This study has identified sporadic regions of heterochromatin and euchromatin and these are source of the banding pattern of polytene chromosomes. Raman can also detect cell division through imaging of DNA. Raman has

impending perspective to identify cells undergoing cell division or apoptosis within living tissue [108].

Viehoever et al, examined the use of organotypic raft as an *in vitro* model of *in vivo* tissue conditions in an attempt to overcome some of the limitations of previously used methods. In this study, organotypic raft cultures resembling normal and dysplastic epithelial cervical tissue were conducted and grown at an air-liquid interface for 2 weeks. Raman spectra of normal as well as dysplastic raft cultures were measured and compared with *in vivo* spectra from the corresponding tissue type. These investigations showed that the Raman spectra of the raft cultures are similar to the spectra acquired from the cervix in vivo for both normal and dysplastic tissues. It was concluded that this type of culture is an effective and useful tool for the cellular and biochemical analysis of tissue spectra [112].

Koljenovic et al conducted a study on meningioma and normal dura matter by Raman microscpectroscopy to assess the possibility of developing an in vivo Raman method for guidance of meningioma resections. Raman maps were constructed of cryosections of dura and meningioma obtained from 20 patients. Comparison of these maps with histopathology enabled assignment of the spectra to either meningioma or dura. It was concluded that large differences exist between the Raman spectra of dura and meningioma, due to the high collagen content of dura and the increased lipid content of tumours. In this study, a classification model for dura and tumour tissue based on linear discriminant analysis of Raman spectra yielded an accuracy of 100%. It was shown that Raman spectra enable meningioma to be distinguished from dura. According to the writers, this can make Raman spectroscopy a viable candidate for guidance of surgical resection of meningioma [113].

Lieber et al reported that cancer field effects (CFE) could be detected in normal tissues using Raman Spectroscopy. The changes in normal tissues due to effect of surrounding neoplastic lesion, are collectively defined as CFE or malignancy-associated changes. Organotypic tissue culture raft models were used in this study and Raman measurement were recorded from dermis and epidermis of both naïve and tumour-associated populations. Raman spectra of epidermis have seen differences in amino acids near 855cm<sup>-1</sup> (tyrosine and proline) and 1004 cm<sup>-1</sup> (phenylalanine). Raman peak at 1004 cm<sup>-1</sup> suggests C-C vibration of keratin. The results have shown some changes in amide III, protein and lipid band at the region 1250 and 1340 cm<sup>-1</sup>. Major differences were seen at 858 cm<sup>-1</sup> shoulder of the 855 cm<sup>-1</sup> (tyrosine/proline) peak, and in the 1018 cm<sup>-1</sup> neck region between the 1004 cm<sup>-1</sup> (phenylalanine/keratin) peak and the 1040 cm<sup>-1</sup> peak attributed to both proline and oxidized albumin. Furthermore dermal spectra have shown distinct differences in CH2 and CH3 deformations at 1420 cm<sup>-1</sup> region. PCA has classified naïve and tumour associated rafts with sensitivity of 94% and specificity of 78%. Results demonstrated above and previous data from various raft models have shown Raman spectral changes to be result of CFE with more certainty. This study validates the use of Raman in animal and clinical studies to detect the CFE nature in multi-tissue and trans-organ environs, including the effects of hemo-dynamics and lymphatic circulation. Further research can potentially allow Raman as a tool to rapidly screen and diagnosis of internal tumours by analysing readily available anatomy [114].

Silva et al reported that combination of Raman spectroscopy and multivariate analysis such as PCA and mahalanobis distance could be used to distinguish between normal and prostate cancer (CaP) tissue. Raman spectra were collected from normal prostate tissues and neoplastic

(CaP) tissues from patients submitted to radical prostatectomy, using 830 nm laser. The spectra of both tissues have shown clear visible differences. The Raman spectra of cancerous tissues showed less intensity band at 1655 cm<sup>-1</sup>(C=O stretching mode of amide I of proteins and C=C stretching of lipids) and high intensity peaks at 1452 cm<sup>-1</sup>(CH<sub>2</sub> bending mode of proteins), 1330 cm<sup>-1</sup> (DNA purine bases and CH<sub>2</sub>/CH<sub>3</sub> wagging of collagen) and 1563 cm<sup>-1</sup> (guanine and adenine from nucleic acid). The presence of high amounts of genetic material and protein represents the malignant nature of the cancer. The PCA analytical model has shown better results when compared to the biochemical model. It shows the capability of PCA/Mahalanobis to categorize the spectra. Although despite the minor diagnostic capability, the simplified biochemical model exhibited the N tissue had greater protein-like characters and the CaP has greater lipid-like characters [115].

Rabah et al reported that Raman spectroscopy to diagnose and classification neuroblastoma in children. A total 698 spectra were collected from normal adrenal glands, neuroblastomas, ganglioneuromas, nerve sheath tumours and pheochromocytoma by using 785-nm laser resource. Higher amounts of carotenoids (1002, 1160 and 1518 cm<sup>-1</sup>) were observed in the Raman spectrum of normal adrenal tissue. These peaks (1160 and 1518 cm<sup>-1</sup>) were absent in neuroblastomas and ganglioneuromas, signifying that their absence may also play a role in the carcinogenesis. The spectra of neuroblastomas and ganglioneuromas have shown high protein intensity peaks at 754, 853, 938, 1002, 1300 to 1345, 1447, 1550, 1620, and 1660 cm<sup>-1</sup>. Raman spectroscopy was successfully differentiated between normal adrenal gland, neuroblastoma, and ganglio-neuroma with 100% sensitivity and 100% specificity. These results are well correlated with the Shimada histologic classification system with 100% sensitivity and 100% specificity.

This study has suggested that spectral profiles from different paediatric tissues and tumours will be use to create a library of molecular fingerprints. A large data base can be accumulated from different institutes which can then help to design and optimize a probe that can collect data in clinical paediatrics [116].

Zhang et al demonstrated that stimulated Raman scattering (SRS) could be used to live cell imaging of nucleic acids. SRS, a coherent Raman scattering technique, is advantage over CARS in nonresonant background and spectral distortion. This study has shown live cell imaging of two mammalian cell lines namely human embryonic kidney cells and breast cancer cells, and single polytene chromosomes within the salivary glands of Drosophila melanogaster, commonly known as fruit fly. Targeted molecule concentration is linearly propositional to SRS signal that can be used for imaging in the fingerprint region. Two excitation beams (1064 nm Nd:YVO4 laser and 532nm Nd:YVO4 laser) with the frequency difference matching the vibrational frequency of targeted molecules are applied. Due to high amount of DNA concentration, the spectrum of Drosophila melanogaster larvae has shown peaks at 2845 cm<sup>-1</sup> (CH<sub>2</sub> vibration in lipids), 1655 cm<sup>-1</sup> (amide I proteins), 785 cm<sup>-1</sup>(phosphodiester stretch) and 1090 cm<sup>-1</sup> (dioxy stretch of the phosphate backbone). This study has identified sporadic regions of heterochromatin and euchromatin and these are source of the banding pattern of polytene chromosomes. Raman can also detect cell division through imaging of DNA. Raman has impending perspective to identify cells undergoing cell division or apoptosis within living tissue [108].

Finally, Short et al reported that Raman spectroscopy can monitor changes due to cell proliferation. This was done by investigating cultures in the plateau (nonproliferating) and

exponential (proliferating) phases of growth, and estimating the relative amounts of biochemical components (lipid, protein, DNA, RNA) in cells and nuclei. Using relative amounts and ratios of biochemical components, reproducible differences were detected and quantified. It was shown that the differences due to cell proliferation can be assigned to specific biochemical changes. A detailed explanation of the changes in quantities of these compounds and their ratios was presented, and finally, it was concluded that this information can be important for Raman detection of rapidly dividing populations of cancer cells in vivo [118].

It has also been reported that the intrinsic Raman scattering intensity of single-walled carbon nanotubes (SWNTs) does not decay over time. Raman spectroscopy can subsequently be used to measure the post injection blood concentration of SWNTs with different polyethyleneglycol (PEG) coatings in mice and therefore glean nanotube blood circulation times. Raman spectroscopy and Raman imaging are also employed to probe the bio-distribution of SWNTs in various organs of mice ex vivo over a period of several months. It has been established that the surface chemistry of nanotubes is critical to their *in vivo* behaviour. This is due to pristine carbon nanotubes which have significantly hydrophobic surfaces and are highly nonspecific in binding to biological species. Recently, it was discovered that intravenously injected pristine SWNTs are highly rich in the lung and also in reticuloendothelial system and remain in mice indefinitely. This hydrophobicity has to be blocked by proper chemical functionalisation such as the PEG coatings, which enables biologically inert SWNTs with long blood circulation, low RES uptake. and relatively fast clearance from organs and excretion from the body. For the *in vivo* behaviour of nanotubes the degree of PEGylation of SWNTs is important. Longer PEG chains, especially those with branched structures, are excellent in affording SWNTs with the most desirable

characteristics for *in vivo* applications. This finding should also be applicable to functionalisation of various other nanomaterials such as nanocrystals, particles for *in vivo* research. SWNTs detected in the faeces of mice clearly revealed that the biliary excretion pathway. A proportion of nanotubes seem to be excreted via the renal pathway. In addition, no obvious toxic effect is found in the necropsy, histology, and blood chemistry studies, which warrants the safety of properly functionalised carbon nanotubes for future *in vivo* biomedical applications [122].

Shapiro et al employed Raman microscope to diagnose urothelial carcinoma commonly known as bladder cancer (BCa), from epithelial cells of the voided urine. Previous studies have attempted to discriminate BCa from normal bladder tissue by using Raman spectroscopy. Raman spectra were obtained from normal and cancerous tissues by using 532nm visible laser. A distinct peak at 1584 cm<sup>-1</sup> was observed in malignant tissue and it was absent in normal tissues. This group has developed a model based on peak height (1584 cm<sup>-1</sup>) of normalized spectrum and used sets of thresholds of the height to classify healthy, low-grade and high-grade tumors. The model has precisely classified low-grade tumors in 88% and high-grade tumors in 98.6%. Raman molecular imaging (RMI) yields a 92% of sensitivity and 91% of specificity for detecting BCa. This study has very high accuracy in differentiating low-grade tumors from high-grade tumours. Low-grade tumors were precisely assigned in 74% of the cases and high-grade tumors in 98.5% [124].

Zong et al reported that telomeric elongation controlled SERS (TEC-SERS) method could be useful in cancer diagnostic and therapeutic approaches. This approach involves binding of Raman reporter molecules and thiolated telomerase substrate primer to gold nanoparticles to construct SERS tag. This active tag forms G- quadruplex structures in the presence of telomerase

and elongation step stops in the absence of telomerase. TEC-SERS detection was applied on telomerase extract from cancer cell lines such as HeLa, SKBR3 and MCF7, and normal fibroblasts MRC-5. TEC-SERS has proved great reliability, simplicity and sensitivity in detecting SERS substrates. This method can detect telomerase up 2 to 3 orders of magnitude and avoid high cost associated Polymerase Chain Reaction (PCR) procedures [125].

T. Bhattacharjee et al reported that Swiss bare mice are best options for transcutaneous breast cancer studies through Raman spectroscopy. Transcutaneous spectra of Swiss mice have not only shown best signal-to-noise ratio, but also closer similarities towards *ex vivo* and *in vivo* human breast spectra. The spectral classification efficiency between normal breast and breast tumors was 99% and breast-to-bone metastasis can also be studied [126-127].

Sahu et al conducted pilot study to explore Raman spectroscopic detection of serum specific markers in treated, mild, moderate and advance stages of asthma samples. Currently, the force expiratory volume in one-second (FEV) values is considered as gold standard method for diagnosis and classification of different grades of asthma. Raman spectra were collected from serum samples on CaF<sub>2</sub> windows using a 785nm diode laser. Major spectral differences were reported between treated and different grades in the region of Amide I, DNA and δ CH<sub>2</sub> deformation. Spectra of disease samples have shown high amount of proteins, plasma free amino acids and DNA. These peaks might indicate higher amounts of prostaglandins, leukotrienes, histamines and glycosaminoglycans. These compounds play important role in the inflammatory response and will appear in huge amounts during asthma. Chemometrics algorithms such as PCA, PC-LDA and Leave-one-out-cross-validation (LOOCV) were applied on spectral data to

classify control and diseased serum samples. Multivariate approach has also classified different grades of asthma and treated versus untreated [127].

Fullwood et al have reported that importance of substrate choice and sample preparation in spectroscopic studies to understand histopathology. This study has covered effects of dewaxing procedure, spectral efficiency of different substrates such as low- E MirrIR slides, spectrosil quartz and calcium fluoride (CaF<sub>2</sub>). Low-E glass slide has shown highest baseline whereas CaF<sub>2</sub> has lowest. Both CaF<sub>2</sub> and spectrosil slides have retained paraffin wax due to their surface roughness during dewaxing procedure whereas low-E slides does not. This study has also found link between density of tissue type and dewaxing protocol. Dense cancerous tissue had retained more wax compared to less dense normal tissue during dewaxing protocol [128].

R. Mehrotra et al reported that SERS Raman spectroscopy could be used to explore DNA interactions with drugs in cancer therapeutic studies. Lomustine, an anticancer drug is used to treat various types of cancers such as brain, small cell lung and lymphomas. Calf thymus DNA was used to study conformational and structural interactions with drug at physiological conditions. Major Raman peaks have revealed stretching vibrations of nitrogenous bases, symmetric and asymmetric phosphate and phosphate backbone. Raman spectra have also revealed alkylation of major and minor grooves of double helical DNA, lomustine interacting sites on purines, pyrimidines and sugar-phosphate backbone. This study has promised SERS approach can be helpful in further understanding of DNA binding mechanisms in novel drug therapeutics[129].

#### The Characteristic Peak Frequencies

It is believed that accurate peak definitions along with different multivariate approaches have significant influence on reliability of the results provided through different spectroscopic techniques. Most of the researchers rely on reported studies to date in literature indicate that previously published work was very useful not only in understanding the chemical fingerprint of the biological molecules but also in distinguishing the cancer from normal tissues. However, without having a reliable and detailed database, which can cover most of the required peaks in the spectral range, it would be a time-consuming task to find the meanings of different unknown peak intensities. This updated article covers a wide range of supervised and unsupervised algorithms, how they have contributed towards diagnostic applications. In biological studies, for instance, where wide range of chemical information related to functional groups can be attributed to every single peak, finding appropriate interpretations, which can demonstrate the clinical importance of the technique and achieved results, can be one of the most important steps in understanding spectroscopic research work. As a result, the updated review with the aim of putting these shortages aside, a wide range of most frequently reported Raman peaks in biological tissues are presented in Table 1.

#### **SUMMARY**

Raman spectroscopy has become powerful non-invasive tool to explore biochemical information of biological tissues, because each biological molecule possesses a unique pattern of vibration that can serve as a Raman marker. In recent years Raman spectroscopy has been vividly used in

cancer diagnostic studies and it has become subject of great interest as an in vivo diagnostic tool to understand chemical and morphological structure of tissue. The information presented in this work can result in significant savings, particularly in the time scientists have to put for defining the peaks and they find in their studies. It has been tried to collect and present the data in such a way that can be referred to and used to make reliable definitions for spectral investigations.

The tabulated part, which is the main part of this article, has provided chemical fingerprint of each peak and its related study. It is suggested that, considering the type of samples being investigated and the chemical bands and functional groups which can possibly exist in the samples, the peak frequencies can be located in the table, and the appropriate interpretations could be chosen. Furthermore, having a detailed knowledge of the list of peaks which can be assigned to different biochemical compounds (such as lipids, proteins, or nucleic acids) would lead to a better correlation between the engineering and the medical aspects of spectroscopy. The lipid content and the chemical structure of these compounds, for instance, can be evaluated using peaks frequencies of 1754cm<sup>-1</sup> (C=O), 1656cm<sup>-1</sup> (C=C), 1440cm<sup>-1</sup> (CH<sub>2</sub> bend), and 1300 cm<sup>-1</sup> (CH<sub>2</sub> twist). The specifications of proteins content of biological samples can also be understood from 1656cm<sup>-1</sup> (amide I), 1450cm<sup>-1</sup> (CH<sub>2</sub> bend), 1100-1375cm<sup>-1</sup> (amide III), and 1004 cm<sup>-1</sup> (phenylalanine) [70]. Recent advances in Raman spectroscopy have revealed morphological changes associated with tissues such as nuclear enlargement, which became Raman marker for cancer detection. On the other hand, Raman results have shown great correlation with pathological studies and have attracted attention from many clinical researchers to reduce number of biopsies, patient trauma and high medical costs. However, it seems that more articles and scientific backing can be collected to improve this work, to keep it updated,

and to prepare a unique database which can be used for different methodologies. In addition, and along with the different research topics being covered by Raman spectroscopy day by day, this article can be of crucial assistance for spectroscopists, not only in the biological fields, but also in areas related to materials and tissue engineering.

#### **REFERENCES**

- 1. A. Mahadevan-Jansen, R. Richards-Kortum, and Ieee, *Raman Spectroscopy for Cancer Detection: A Review*, in *International Conference of the IEEE Engineering-in-Medicine-and-Biology-Society*. 1997: Chicago, Il. p. 2722-2728.
- 2. E.B. Hanlon, R. Manoharan, T.W. Koo, K.E. Shafer, J.T. Motz, M. Fitzmaurice, J.R. Kramer, I. Itzkan, R.R. Dasari, and M.S. Feld, "Prospects for in Vivo Raman Spectroscopy," Physics in Medicine and Biology. vol. 45, no. 2, Feb. 2000, pp. R1-R59.
- 3. R.K. Dukor, Vibrational Spectroscopy in the Detection of Cancer, 2002.
- L.P. Choo-Smith, H.G.M. Edwards, H.P. Endtz, J.M. Kros, F. Heule, H. Barr, J.S. Robinson, H.A. Bruining, and G.J. Puppels, "Medical Applications of Raman Spectroscopy: From Proof of Principle to Clinical Implementation," Biopolymers. vol. 67, no. 1, 2002. 2002.
- 5. B. Swinson, W. Jerjes, M. El-Maaytah, P. Norris, and C. Hopper, "Optical Techniques in Diagnosis of Head and Neck Malignancy," Oral Oncology. vol. 42, no. 3, Mar. 2006.
- R.A. Shaw and H.H. Mantsch, "Vibrational Biospectroscopy: From Plants to Animals to Humans. A Historical Perspective," Journal of Molecular Structure. vol. 481, May 4. 1999.
- W. Petrich, "Mid-Infrared and Raman Spectroscopy for Medical Diagnostics?," Shock. vol. 26, Oct. 2006.

- 8. H. Zeng, McWilliams, A. and Lam, S., "Optical Spectroscopy and Imaging for Early Lung Cancer Detection: A Review," Photodiagnosis and Photodynamic Therapy. vol. 1, no. 2. 2004, pp. 111-122.
- M.F. Parker, "Emerging Technology in Cervical Cancer Screening: Spectroscopy,"
   Clinical Obstetrics and Gynecology. vol. 48, no. 1, Mar. 2005.
- E. Dekker and P. Fockens, "Advances in Colonic Imaging: New Endoscopic Imaging Methods," European Journal of Gastroenterology & Hepatology. vol. 17, no. 8, Aug. 2005.
- 11. S.G. Demos, A.J. Vogel, and A.H. Gandjbakhche, "Advances in Optical Spectroscopy and Imaging of Breast Lesions," Journal of Mammary Gland Biology and Neoplasia. vol. 11, no. 2, Apr. 2006.
- 12. G.D. Pitt, D.N. Batchelder, R. Bennett, R.W. Bormett, I.P. Hayward, B.J.E. Smith, K.P.J. Williams, Y.Y. Yang, K.J. Baldwin, and S. Webster, "Engineering Aspects and Applications of the New Raman Instrumentation," Iee Proceedings-Science Measurement and Technology. vol. 152, no. 6, Nov. 2005.
- 13. I.U. Rehman, Movasaghi, Z. and Rehman, S., Vibrational spectroscopy for Tissue Analysis, CRC Press, Taylor & Francis Group, 2012.
- Z. Movasaghi, S. Rehman, and I.U. Rehman, "Raman Spectroscopy of Biological Tissues," Applied Spectroscopy Reviews. vol. 42, no. 5, 2007. 2007.
- Z. Movasaghi, S. Rehman, and I.U. Rehman, "Fourier Transform Infrared (Ftir)
   Spectroscopy of Biological Tissues," Applied Spectroscopy Reviews. vol. 43, no. 2,
   2008. 2008, pp. 134-179.

- 16. M.A. Short, H. Lui, D. McLean, H. Zeng, A. Alajlan, and X.K. Chen, "Changes in Nuclei and Peritumoral Collagen within Nodular Basal Cell Carcinomas Via Confocal Micro-Raman Spectroscopy," Journal of Biomedical Optics. vol. 11, no. 3, May-Jun. 2006.
- 17. J. Sebag, S. Nie, K. Reiser, and N.T. Yu, Raman-Spectroscopy Characterization of Diabetes Effects on Human Vitreous in Diabetic-Retinopathy, in Conf on Ophthalmic Technologies 3. 1993: Los Angeles, Ca.
- 18. R. Singh and F. Riess, "Sir C. V. Raman and the Story of the Nobel Prize," Current Science. vol. 75, no. 9, Nov 10. 1998.
- J. Conroy, A.G. Ryder, M.N. Leger, K. Hennessey, and M.G. Madden, Qualitative and Quantitative Analysis of Chlorinated Solvents Using Raman Spectroscopy and Machine Learning, in Opto-Ireland 2005 Conference. 2005: Dublin, IRELAND.
- Z.W. Huang, A. McWilliams, H. Lui, D.I. McLean, S. Lam, and H.S. Zeng, "Near-Infrared Raman Spectroscopy for Optical Diagnosis of Lung Cancer," International Journal of Cancer. vol. 107, no. 6, Dec 20, 2003.
- K.E. Shafer-Peltier, A.S. Haka, M. Fitzmaurice, J. Crowe, J. Myles, R.R. Dasari, and M.S. Feld, "Raman Microspectroscopic Model of Human Breast Tissue: Implications for Breast Cancer Diagnosis in Vivo," Journal of Raman Spectroscopy. vol. 33, no. 7, Jul. 2002, pp. 552-563.
- 22. E. Gazi, J. Dwyer, P. Gardner, A. Ghanbari-Siahkali, A.P. Wade, J. Miyan, N.P. Lockyer, J.C. Vickerman, N.W. Clarke, J.H. Shanks, L.J. Scott, C.A. Hart, and M. Brown, "Applications of Fourier Transform Infrared Microspectroscopy in Studies of Benign

- Prostate and Prostate Cancer. A Pilot Study," Journal of Pathology. vol. 201, no. 1, Sep. 2003.
- 23. I. Rehman, R. Smith, L.L. Hench, and W. Bonfield, "Structural Evaluation of Human and Sheep Bone and Comparison with Synthetic Hydroxyapatite by Ft-Raman Spectroscopy," Journal of Biomedical Materials Research. vol. 29, no. 10, Oct. 1995.
- 24. L.L. McManus, F. Bonnier, G.A. Burke, B.J. Meenan, A.R. Boyd, and H.J. Byrne, "Assessment of an Osteoblast-Like Cell Line as a Model for Human Primary Osteoblasts Using Raman Spectroscopy," Analyst. vol. 137, no. 7, 2012. 2012, pp. 1559-1569.
- 25. J.S. Nyman, A.J. Makowski, C.A. Patil, T.P. Masui, E.C. O'Quinn, X. Bi, S.A. Guelcher, D.P. Nicollela, and A. Mahadevan-Jansen, "Measuring Differences in Compositional Properties of Bone Tissue by Confocal Raman Spectroscopy," Calcified Tissue International. vol. 89, no. 2, Aug. 2011, pp. 111-122.
- 26. S. Kachi, K. Hirano, Y. Takesue, and M. Miura, "Unusual Corneal Deposit after the Topical Use of Cyclosporine as Eyedrops," American Journal of Ophthalmology. vol. 130, no. 5, Nov. 2000.
- U. Utzinger, D.L. Heintzelman, A. Mahadevan-Jansen, A. Malpica, M. Follen, and R. Richards-Kortum, "Near-Infrared Raman Spectroscopy for in Vivo Detection of Cervical Precancers," Applied Spectroscopy. vol. 55, no. 8, Aug. 2001.
- 28. L.E. Kamemoto, A.K. Misra, S.K. Sharma, M.T. Goodman, H. Luk, A.C. Dykes, and T. Acosta, "Near-Infrared Micro-Raman Spectroscopy for in Vitro Detection of Cervical Cancer," Applied Spectroscopy. vol. 64, no. 3, Mar. 2010, pp. 255-261.

- J.L. Gonzalez-Solis, J. Rodriguez-Lopez, J.C. Martinez-Espinosa, C. Frausto-Reyes, L.F. Jaye-Suarez, A.C. Aguilar-Lemarroy, H. Vargas-Rodriguez, and E. Martinez-Cano, Detection of Cervical Cancer Analyzing Blood Samples with Raman Spectroscopy and Multivariate Analysis, in 23rd International Congress on Laser Medicine/IALMS Courses/3rd Biannual Congress of the International-Photo-Therapy-Association. 2010: Florence, ITALY. p. 91-95.
- 30. N. Stone, C. Kendall, N. Shepherd, P. Crow, and H. Barr, "Near-Infrared Raman Spectroscopy for the Classification of Epithelial Pre-Cancers and Cancers," Journal of Raman Spectroscopy. vol. 33, no. 7, Jul. 2002.
- 31. N. Stone, C. Kendall, J. Smith, P. Crow, and H. Barr, "Raman Spectroscopy for Identification of Epithelial Cancers," Faraday Discussions. vol. 126, 2004. 2004.
- 32. M.D. Keller, E.M. Kanter, C.A. Lieber, S.K. Majumder, J. Hutchings, D.L. Ellis, R.B. Beaven, N. Stone, and A. Mahadevan-Jansen, "Detecting Temporal and Spatial Effects of Epithelial Cancers with Raman Spectroscopy," Disease Markers. vol. 25, no. 6. 2008, pp. 323-337.
- 33. Y.K. Min, T. Yamamoto, E. Kohda, T. Ito, and H. Hamaguchi, "1064 Nm near-Infrared Multichannel Raman Spectroscopy of Fresh Human Lung Tissues," Journal of Raman Spectroscopy. vol. 36, no. 1, Jan. 2005.
- 34. S. Kaminaka, H. Yamazaki, T. Ito, E. Kohda, and H.O. Hamaguchi, "Near-Infrared Raman Spectroscopy of Human Lung Tissues: Possibility of Molecular-Level Cancer Diagnosis," Journal of Raman Spectroscopy. vol. 32, no. 2, Feb. 2001.

- 35. Z.W. Huang, A. McWilliams, S. Lam, J. English, D.I. McLean, H. Lui, and H. Zeng, "Effect of Formalin Fixation on the near-Infrared Raman Spectroscopy of Normal and Cancerous Human Bronchial Tissues," International Journal of Oncology. vol. 23, no. 3, Sep. 2003.
- 36. Y. Oshima, H. Shinzawa, T. Takenaka, C. Furihata, and H. Sato, "Discrimination Analysis of Human Lung Cancer Cells Associated with Histological Type and Malignancy Using Raman Spectroscopy," Journal of Biomedical Optics. vol. 15, no. 1, Jan-Feb. 2010.
- 37. X. Li, T. Yang, S. Li, and T. Yu, Surface-Enhanced Raman Spectroscopy Differences of Saliva between Lung Cancer Patients and Normal People, in Conference on Clinical and Biomedical Spectroscopy and Imaging II. 2011: Munich, GERMANY.
- 38. N.Y. Huang, M. Short, J.H. Zhao, H.Q. Wang, H. Lui, M. Korbelik, and H.S. Zeng, "Full Range Characterization of the Raman Spectra of Organs in a Murine Model," Optics Express. vol. 19, no. 23, Nov. 2011, pp. 22892-22909.
- 39. H. Nawaz, F. Bonnier, A.D. Meade, F.M. Lyng, and H.J. Byrne, "Comparison of Subcellular Responses for the Evaluation and Prediction of the Chemotherapeutic Response to Cisplatin in Lung Adenocarcinoma Using Raman Spectroscopy," Analyst. vol. 136, no. 12. 2011, pp. 2450-2463.
- 40. N.D. Magee, J.S. Villaumie, E.T. Marple, M. Ennis, J.S. Elborn, and J.J. McGarvey, "Ex Vivo Diagnosis of Lung Cancer Using a Raman Miniprobe," Journal of Physical Chemistry B. vol. 113, no. 23, Jun 11. 2009, pp. 8137-8141.

- 41. D.C.B. Redd, Z.C. Feng, K.T. Yue, and T.S. Gansler, "Raman-Spectroscopic Characterization of Human Breast Tissues Implications for Breast-Cancer Diagnosis," Applied Spectroscopy. vol. 47, no. 6, Jun. 1993.
- 42. N.J. Kline and P.J. Treado, "Raman Chemical Imaging of Breast Tissue," Journal of Raman Spectroscopy. vol. 28, no. 2-3, Feb-Mar. 1997.
- 43. K. Tam, Armstrong, R. S., Carter, E. A., Lay, P. A., Mountford, C., Dowd, S., Himmerlreich, U. and Russell, P., Raman Spectroscopy for Breast Cancer Detection: A Sample Processing Study., in Proceedings of the XIX International Conference on Raman Spectroscopy. 2004. p. 457-457.
- 44. A.S. Haka, K.E. Shafer-Peltier, M. Fitzmaurice, J. Crowe, R.R. Dasari, and M.S. Feld, "Diagnosing Breast Cancer by Using Raman Spectroscopy," Proceedings of the National Academy of Sciences of the United States of America. vol. 102, no. 35, Aug 30. 2005, pp. 12371-12376.
- 45. S. Rehman, Z. Movasaghi, A.T. Tucker, S.P. Joel, J.A. Darr, A.V. Ruban, and I.U. Rehman, "Raman Spectroscopic Analysis of Breast Cancer Tissues: Identifying Differences between Normal, Invasive Ductal Carcinoma and Ductal Carcinoma in Situ of the Breast Tissue," Journal of Raman Spectroscopy. vol. 38, no. 10, Oct. 2007, pp. 1345-1351.
- A.S. Haka, Z. Volynskaya, J.A. Gardecki, J. Nazemi, R. Shenk, N. Wang, R.R. Dasari,
   M. Fitzmaurice, and M.S. Feld, "Diagnosing Breast Cancer Using Raman Spectroscopy:
   Prospective Analysis," Journal of Biomedical Optics. vol. 14, no. 5, Sep-Oct. 2009.

- 47. A. Saha, I. Barman, N.C. Dingari, S. McGee, Z. Volynskaya, L.H. Galindo, W. Liu, D. Plecha, N. Klein, R.R. Dasari, and M. Fitzmaurice, "Raman Spectroscopy: A Real-Time Tool for Identifying Microcalcifications During Stereotactic Breast Core Needle Biopsies," Biomedical Optics Express. vol. 2, no. 10, Oct 1. 2011, pp. 2792-2803.
- 48. H. Abramczyk, B. Brozek-Pluska, J. Surmacki, J. Jablonska, and R. Kordek, "The Label-Free Raman Imaging of Human Breast Cancer," Journal of Molecular Liquids. vol. 164, no. 1-2, Nov 1. 2011, pp. 123-131.
- 49. H. Abramczyk, B. Brozek-Pluska, J. Surmacki, J. Jablonska-Gajewicz, and R. Kordek, "Raman 'Optical Biopsy' of Human Breast Cancer," Progress in Biophysics & Molecular Biology. vol. 108, no. 1-2, Jan. 2012, pp. 74-81.
- 50. W.T. Cheng, M.T. Liu, H.N. Liu, and S.Y. Lin, "Micro-Raman Spectroscopy Used to Identify and Grade Human Skin Pilomatrixoma," Microscopy Research and Technique. vol. 68, no. 2, Oct. 2005.
- 51. S. Kaminaka, T. Ito, H. Yamazaki, E. Kohda, and H. Hamaguchi, "Near-Infrared Multichannel Raman Spectroscopy toward Real-Time in Vivo Cancer Diagnosis," Journal of Raman Spectroscopy. vol. 33, no. 7, Jul. 2002.
- 52. S. Sigurdsson, P.A. Philipsen, L.K. Hansen, J. Larsen, M. Gniadecka, and H.C. Wulf, "Detection of Skin Cancer by Classification of Raman Spectra," Ieee Transactions on Biomedical Engineering. vol. 51, no. 10, Oct. 2004.
- 53. M. Gniadecka, H.C. Wulf, N.N. Mortensen, O.F. Nielsen, and D.H. Christensen, "Diagnosis of Basal Cell Carcinoma by Raman Spectroscopy," Journal of Raman Spectroscopy. vol. 28, no. 2-3, Feb-Mar. 1997.

- 54. B.W. Barry, H.G.M. Edwards, and A.C. Williams, "Fourier-Transform Raman and Infrared Vibrational Study of Human Skin Assignment of Spectral Bands," Journal of Raman Spectroscopy. vol. 23, no. 11, Nov. 1992.
- 55. P.J. Caspers, G.W. Lucassen, E.A. Carter, H.A. Bruining, and G.J. Puppels, "In Vivo Confocal Raman Microspectroscopy of the Skin: Noninvasive Determination of Molecular Concentration Profiles," Journal of Investigative Dermatology. vol. 116, no. 3, Mar. 2001.
- M. Larraona-Puy, A. Ghita, A. Zoladek, W. Perkins, S. Varma, I.H. Leach, A.A. Koloydenko, H. Williams, and I. Notingher, "Development of Raman Microspectroscopy for Automated Detection and Imaging of Basal Cell Carcinoma," Journal of Biomedical Optics. vol. 14, no. 5, Sep-Oct. 2009.
- 57. S.B. Cartaxo, I.D. de Abranches Oliveira Santos, R. Bitar, A.F. Oliveira, L.M. Ferreira, H.S. Martinho, and A.A. Martin, "Ft-Raman Spectroscopy for the Differentiation between Cutaneous Melanoma and Pigmented Nevus," Acta Cirurgica Brasileira. vol. 25, no. 4, Jul-Aug. 2010, pp. 351-356.
- M. Larraona-Puy, A. Ghita, A. Zoladek, W. Perkins, S. Varma, I.H. Leach, A.A. Koloydenko, H. Williams, and I. Notingher, "Discrimination between Basal Cell Carcinoma and Hair Follicles in Skin Tissue Sections by Raman Micro-Spectroscopy," Journal of Molecular Structure. vol. 993, no. 1-3, May. 2011, pp. 57-61.
- 59. H. Wang, N. Huang, J. Zhao, H. Lui, M. Korbelik, and H. Zeng, "Depth-Resolved in Vivo Micro-Raman Spectroscopy of a Murine Skin Tumor Model Reveals Cancer-

- Specific Spectral Biomarkers," Journal of Raman Spectroscopy. vol. 42, no. 2, Feb. 2011, pp. 160-166.
- 60. K. Konig, H.G. Breunig, R. Buckle, M. Kellner-Hofer, M. Weinigel, E. Buttner, W. Sterry, and J. Lademann, "Optical Skin Biopsies by Clinical Cars and Multiphoton Fluorescence/Shg Tomography," Laser Physics Letters. vol. 8, no. 6, Jun. 2011, pp. 465-468.
- 61. A.F. de Oliveira, I. Santos, S.B. Cartaxo, R.A. Bitar, M. Enokihara, H.D. Martinho, A.A. Martin, and L.M. Ferreira, "Differential Diagnosis in Primary and Metastatic Cutaneous Melanoma by Ft-Raman Spectroscopy," Acta Cirurgica Brasileira. vol. 25, no. 5, Oct. 2010, pp. 434-439.
- 62. Y.Y. Tan, A.G. Shen, J.W. Zhang, N. Wu, L. Feng, Q.F. Wu, Y. Ye, J.M. Hu, and Ieee, "Design of Auto-Classifying System and Its Application in Roman Spectroscopy Diagnosis of Gastric Carcinoma," 2003 International Conference on Machine Learning and Cybernetics, Vols 1-5, Proceedings, 2003. 2003.
- 63. S.F. Weng, X.F. Ling, Y.Y. Song, Y.Z. Xu, W.H. Li, X. Zhang, L. Yang, W. Sun, X. Zhou, and J. Wu, "FTIR Fiber Optics and Ft-Raman Spectroscopic Studies for the Diagnosis of Cancer," American clinical laboratory. vol. 19, no. 7, 2000-Aug. 2000.
- 64. G. Shetty, C. Kendall, N. Shepherd, N. Stone, and H. Barr, "Raman Spectroscopy: Elucidation of Biochemical Changes in Carcinogenesis of Oesophagus," British Journal of Cancer. vol. 94, no. 10, May 22. 2006.
- 65. S. Feng, J. Pan, Y. Wu, D. Lin, Y. Chen, G. Xi, J. Lin, and R. Chen, "Study on Gastric Cancer Blood Plasma Based on Surface-Enhanced Raman Spectroscopy Combined with

- Multivariate Analysis," Science China-Life Sciences. vol. 54, no. 9, Sep. 2011, pp. 828-834.
- 66. T. Kawabata, H. Kikuchi, S. Okazaki, M. Yamamoto, Y. Hiramatsu, J. Yang, M. Baba, M. Ohta, K. Kamiya, T. Tanaka, and H. Konno, "Near-Infrared Multichannel Raman Spectroscopy with a 1064 Nm Excitation Wavelength for Ex Vivo Diagnosis of Gastric Cancer," Journal of Surgical Research. vol. 169, no. 2, Aug. 2011, pp. E137-E143.
- 67. L. Su, Y.F. Sun, Y. Chen, P. Chen, A.G. Shen, X.H. Wang, J. Jia, Y.F. Zhao, X.D. Zhou, and J.M. Hu, "Raman Spectral Properties of Squamous Cell Carcinoma of Oral Tissues and Cells," Laser Physics. vol. 22, no. 1, Jan. 2012, pp. 311-316.
- 68. M.G. Shim, L. Song, N.E. Marcon, and B.C. Wilson, "In Vivo near-Infrared Raman Spectroscopy: Demonstration of Feasibility During Clinical Gastrointestinal Endoscopy," Photochemistry and Photobiology. vol. 72, no. 1, Jul. 2000.
- C. Kendall, J. Day, J. Hutchings, B. Smith, N. Shepherd, H. Barr, and N. Stone,
   "Evaluation of Raman Probe for Oesophageal Cancer Diagnostics," Analyst. vol. 135, no.
   12, 2010. 2010, pp. 3038-3041.
- 70. R.J. Lakshmi, V.B. Kartha, C.M. Krishna, J.G.R. Solomon, G. Ullas, and P.U. Devi, "Tissue Raman Spectroscopy for the Study of Radiation Damage: Brain Irradiation of Mice," Radiation Research. vol. 157, no. 2, Feb. 2002.
- 71. C. Krafft, L. Neudert, T. Simat, and R. Salzer, "Near Infrared Raman Spectra of Human Brain Lipids," Spectrochimica Acta Part a-Molecular and Biomolecular Spectroscopy. vol. 61, no. 7, May. 2005.

- 72. H. Sato, Y.S. Yamamoto, A. Maruyama, T. Katagiri, Y. Matsuura, and Y. Ozaki, "Raman Study of Brain Functions in Live Mice and Rats: A Pilot Study," Vibrational Spectroscopy. vol. 50, no. 1, May 26. 2009, pp. 125-130.
- M. Koehler, S. Machill, R. Salzer, and C. Krafft, "Characterization of Lipid Extracts from Brain Tissue and Tumors Using Raman Spectroscopy and Mass Spectrometry," Analytical and Bioanalytical Chemistry. vol. 393, no. 5, Mar. 2009, pp. 1513-1520.
- 74. M. Kirsch, G. Schackert, R. Salzer, and C. Krafft, "Raman Spectroscopic Imaging for in Vivo Detection of Cerebral Brain Metastases," Analytical and Bioanalytical Chemistry. vol. 398, no. 4, Oct. 2010, pp. 1707-1713.
- 75. L.-L. Tay, R.G. Tremblay, J. Hulse, B. Zurakowski, M. Thompson, and M. Bani-Yaghoub, "Detection of Acute Brain Injury by Raman Spectral Signature," Analyst. vol. 136, no. 8, 2011. 2011, pp. 1620-1626.
- 76. R. Malini, K. Venkatakrishna, J. Kurien, K.M. Pai, L. Rao, V.B. Kartha, and C.M. Krishna, "Discrimination of Normal, Inflammatory, Premalignant, and Malignant Oral Tissue: A Raman Spectroscopy Study," Biopolymers. vol. 81, no. 3, Feb 15. 2006.
- 77. J.G. Wu, Y.Z. Xu, C.W. Sun, R.D. Soloway, D.F. Xu, Q.G. Wu, K.H. Sun, S.F. Weng, and G.X. Xu, "Distinguishing Malignant from Normal Oral Tissues Using FTIR Fiber-Optic Techniques," Biopolymers. vol. 62, no. 4, 2001. 2001.
- 78. D.P. Lau, Z.W. Huang, H. Lui, D.W. Anderson, K. Berean, M.D. Morrison, L. Shen, and H.S. Zeng, "Raman Spectroscopy for Optical Diagnosis in the Larynx: Preliminary Findings," Lasers in Surgery and Medicine. vol. 37, no. 3, Sep. 2005.

- 79. Y. Li, Z.-N. Wen, L.-J. Li, M.-L. Li, N. Gao, and Y.-Z. Guo, "Research on the Raman Spectral Character and Diagnostic Value of Squamous Cell Carcinoma of Oral Mucosa," Journal of Raman Spectroscopy. vol. 41, no. 2, Feb. 2010, pp. 142-147.
- 80. M.S. Bergholt, W. Zheng, K. Lin, K.Y. Ho, M. Teh, K.G. Yeoh, J.B.Y. So, and Z. Huang, "Characterizing Variability in in Vivo Raman Spectra of Different Anatomical Locations in the Upper Gastrointestinal Tract toward Cancer Detection," Journal of biomedical optics. vol. 16, no. 3, 2011-Mar. 2011, p. 037003.
- 81. D.P. Lau, Z.W. Huang, H. Lui, C.S. Man, K. Berean, M.D. Morrison, and H.S. Zeng, "Raman Spectroscopy for Optical Diagnosis in Normal and Cancerous Tissue of the Nasopharynx Preliminary Findings," Lasers in Surgery and Medicine. vol. 32, no. 3, 2003. 2003.
- 82. W.-L. Lo, J.-Y. Lai, S.E. Feinberg, K. Izumi, S.-Y. Kao, C.-S. Chang, A. Lin, and H.K. Chiang, "Raman Spectroscopy Monitoring of the Cellular Activities of a Tissue-Engineered Ex Vivo Produced Oral Mucosal Equivalent," Journal of Raman Spectroscopy. vol. 42, no. 2, Feb. 2011, pp. 174-178.
- 83. X. Li, J. Lin, J. Ding, S. Wang, Q. Liu, and S. Qing, "Raman Spectroscopy and Fluorescence for the Detection of Liver Cancer and Abnormal Liver Tissue," Conference proceedings: ... Annual International Conference of the IEEE Engineering in Medicine and Biology Society. IEEE Engineering in Medicine and Biology Society. Conference. vol. 1, 2004. 2004.

- 84. J. Guo, B. Du, M. Qian, W. Cai, Z. Wang, and Z. Sun, "Raman Spectroscopic Identification of Normal and Malignant Hepatocytes," Chinese Optics Letters. vol. 7, no. 1, Jan 10. 2009, pp. 60-63.
- 85. I.W. Schie, J. Wu, T. Weeks, M.A. Zern, J.C. Rutledge, and T. Huser, "Label-Free Imaging and Analysis of the Effects of Lipolysis Products on Primary Hepatocytes," Journal of Biophotonics. vol. 4, no. 6, Jun. 2011, pp. 425-434.
- 86. Z. Movasaghi, S. Rehman, and I.U. Rehman, "Raman Spectroscopy Can Detect and Monitor Cancer at Cellular Level: Analysis of Resistant and Sensitive Subtypes of Testicular Cancer Cell Lines," Applied Spectroscopy Reviews. vol. 47, no. 7, 2012. 2012.
- 87. H.P. Chiang, R. Song, B. Mou, K.P. Li, P. Chiang, D. Wang, W.S. Tse, and L.T. Ho, "Fourier Transform Raman Spectroscopy of Carcinogenic Polycyclic Aromatic Hydrocarbons in Biological Systems: Binding to Heme Proteins," Journal of Raman Spectroscopy. vol. 30, no. 7, Jul. 1999.
- 88. S.W.E. van de Poll, T.J. Romer, O.L. Volger, D.J.M. Delsing, T.C.B. Schut, H.M.G. Princen, L.M. Havekes, J.W. Jukema, A. van der Laarse, and G.J. Puppels, "Raman Spectroscopic Evaluation of the Effects of Diet and Lipid-Lowering Therapy on Atherosclerotic Plaque Development in Mice," Arteriosclerosis Thrombosis and Vascular Biology. vol. 21, no. 10, Oct. 2001.
- 89. J. Duarte, M.T.T. Pacheco, R.Z. Machado, L. Silveira, R.A. Zangaro, and A.B. Villaverde, "Use of near-Infrared Raman Spectroscopy to Detect Igg and Igm Antibodies against Toxoplasma Gondii in Serum Samples of Domestic Cats," Cellular and Molecular Biology, vol. 48, no. 5, Jul. 2002.

- 90. X.Z. Li, H.Q. Jin, and Ieee, Raman Spectroscopy of Serum for Cancer Detection, in 23rd Annual International Conference of the IEEE-Engineering-in-Medicine-and-Biology-Society. 2001: Istanbul, Turkey.
- 91. D. Rohleder, W. Kiefer, and W. Petrich, "Quantitative Analysis of Serum and Serum Ultrafiltrate by Means of Raman Spectroscopy," Analyst. vol. 129, no. 10, 2004. 2004.
- 92. U. Neugebauer, J.H. Clement, T. Bocklitz, C. Krafft, and J. Popp, "Identification and Differentiation of Single Cells from Peripheral Blood by Raman Spectroscopic Imaging," Journal of Biophotonics. vol. 3, no. 8-9, Aug. 2010, pp. 579-587.
- 93. U. Neugebauer, T. Bocklitz, J.H. Clement, C. Krafft, and J. Popp, "Towards Detection and Identification of Circulating Tumour Cells Using Raman Spectroscopy," Analyst. vol. 135, no. 12, 2010. 2010, pp. 3178-3182.
- 94. L. Silveira, S. Sathaiah, R.A. Zangaro, M.T.T. Pacheco, M.C. Chavantes, and C.A.G. Pasqualucci, "Correlation between near-Infrared Raman Spectroscopy and the Histopathological Analysis of Atherosclerosis in Human Coronary Arteries," Lasers in Surgery and Medicine. vol. 30, no. 4, 2002. 2002.
- 95. G.J. Puppels, H.S.P. Garritsen, J.A. Kummer, and J. Greve, "Carotenoids Located in Human Lymphocyte Subpopulations and Natural-Killer-Cells by Raman Microspectroscopy," Cytometry. vol. 14, no. 3, 1993. 1993.
- 96. S. Dochow, C. Krafft, U. Neugebauer, T. Bocklitz, T. Henkel, G. Mayer, J. Albert, and J. Popp, "Tumour Cell Identification by Means of Raman Spectroscopy in Combination with Optical Traps and Microfluidic Environments," Lab on a Chip. vol. 11, no. 8, 2011. 2011, pp. 1484-1490.

- 97. D. Lin, J. Lin, Y. Wu, S. Feng, Y. Li, Y. Yu, G. Xi, H. Zeng, and R. Chen, "Investigation on the Interactions of Lymphoma Cells with Paclitaxel by Raman Spectroscopy," Spectroscopy-an International Journal. vol. 25, no. 1, 2011. 2011, pp. 23-32.
- 98. J.L. Deng, Q. Wei, M.H. Zhang, Y.Z. Wang, and Y.Q. Li, "Study of the Effect of Alcohol on Single Human Red Blood Cells Using near-Infrared Laser Tweezers Raman Spectroscopy," Journal of Raman Spectroscopy. vol. 36, no. 3, Mar. 2005.
- 99. F.-T. Liu, S.G. Agrawal, Z. Movasaghi, P.B. Wyatt, I.U. Rehman, J.G. Gribben, A.C. Newland, and L. Jia, "Dietary Flavonoids Inhibit the Anticancer Effects of the Proteasome Inhibitor Bortezomib," Blood. vol. 112, no. 9, Nov 1. 2008.
- 100. C.M. Krishna, G.D. Sockalingum, G. Kegelaer, S. Rubin, V.B. Kartha, and M. Manfait, "Micro-Raman Spectroscopy of Mixed Cancer Cell Populations," Vibrational Spectroscopy. vol. 38, no. 1-2, Jul 29. 2005.
- 101. N. Kuhnert and A. Thumser, "An Investigation into the Use of Raman Microscopy for the Detection of Labelled Compounds in Living Human Cells," Journal of Labelled Compounds & Radiopharmaceuticals. vol. 47, no. 8, Jul. 2004.
- 102. D. Naumann, Infrared and Nir Raman Spectroscopy in Medical Microbiology, in Conference on Infrared Spectroscopy New Tool in Medicine. 1998: San Jose, Ca.
- 103. J.W. Chan, D.S. Taylor, T. Zwerdling, S.M. Lane, K. Ihara, and T. Huser, "Micro-Raman Spectroscopy Detects Individual Neoplastic and Normal Hematopoietic Cells," Biophysical Journal. vol. 90, no. 2, Jan. 2006.

- 104. S. Farquharson, C. Shende, F.E. Inscore, P. Maksymiuk, and A. Gift, "Analysis of 5-Fluorouracil in Saliva Using Surface-Enhanced Raman Spectroscopy," Journal of Raman Spectroscopy. vol. 36, no. 3, Mar. 2005.
- 105. A. Barhoumi and N.J. Halas, "Detecting Chemically Modified Dna Bases Using Surface-Enhanced Raman Spectroscopy," Journal of Physical Chemistry Letters. vol. 2, no. 24, Dec 15. 2011, pp. 3118-3123.
- 106. A.J. Ruiz-Chica, M.A. Medina, F. Sanchez-Jimenez, and F.J. Ramirez, "Characterization by Raman Spectroscopy of Conformational Changes on Guanine-Cytosine and Adenine-Thymine Oligonucleotides Induced by Aminooxy Analogues of Spermidine," Journal of Raman Spectroscopy. vol. 35, no. 2, Feb. 2004.
- 107. K.J. Jalkanen, V.W. Jurgensen, A. Claussen, A. Rahim, G.M. Jensen, R.C. Wade, F. Nardi, C. Jung, I.M. Degtyarenko, R.M. Nieminen, F. Herrmann, M. Knapp-Mohammady, T.A. Niehaus, K. Frimand, and S. Suhai, "Use of Vibrational Spectroscopy to Study Protein and Dna Structure, Hydration, and Binding of Biomolecules: A Combined Theoretical and Experimental Approach," International Journal of Quantum Chemistry. vol. 106, no. 5, Apr 5. 2006.
- 108. X. Zhang, M.B.J. Roeffaers, S. Basu, J.R. Daniele, D. Fu, C.W. Freudiger, G.R. Holtom, and X.S. Xie, "Label-Free Live-Cell Imaging of Nucleic Acids Using Stimulated Raman Scattering Microscopy," Chemphyschem: a European journal of chemical physics and physical chemistry. vol. 13, no. 4, 2012-Mar. 2012, pp. 1054-9.

- 109. T. Vo-Dinh, L.R. Allain, and D.L. Stokes, "Cancer Gene Detection Using Surface-Enhanced Raman Scattering (Sers)," Journal of Raman Spectroscopy. vol. 33, no. 7, Jul. 2002.
- 110. J. Binoy, J.P. Abraham, I.H. Joe, V.S. Jayakumar, G.R. Pettit, and O.F. Nielsen, "Nir-Ft Raman and Ft-Ir Spectral Studies and Ab Initio Calculations of the Anti-Cancer Drug Combretastatin-A4," Journal of Raman Spectroscopy. vol. 35, no. 11, Nov. 2004.
- 111. E. O Faolain, M.B. Hunter, J.M. Byrne, P. Kelehan, M. McNamara, H.J. Byrne, and F.M. Lyng, "A Study Examining the Effects of Tissue Processing on Human Tissue Sections Using Vibrational Spectroscopy," Vibrational Spectroscopy. vol. 38, no. 1-2, Jul 29. 2005.
- 112. A.R. Viehoever, D. Anderson, D. Jansen, and A. Mahadevan-Jansen, "Organotypic Raft Cultures as an Effective in Vitro Tool for Understanding Raman Spectral Analysis of Tissue," Photochemistry and Photobiology. vol. 78, no. 5, Nov. 2003.
- 113. S. Koljenovic, T.B. Schut, A. Vincent, J.M. Kros, and G.J. Puppels, "Detection of Meningioma in Dura Mater by Raman Spectroscopy," Analytical Chemistry. vol. 77, no. 24, Dec 15. 2005.
- 114. C.A. Lieber, H.E. Nethercott, and M.H. Kabeer, "Cancer Field Effects in Normal Tissues Revealed by Raman Spectroscopy," Biomedical Optics Express. vol. 1, no. 3, Oct 1. 2010, pp. 975-982.
- 115. M.A.S.R. Silva, R.M. Lopes, F. Aimbire, K.R.M. Leite, C.A. Pasqualucci, M.T.T. Pacheco, and L. Silveira, Jr., *Diagnostic Model for Differentiating Human Malignant*

- Prostate Lesion from Normal Tissue in Vitro by Raman Spectroscopy, in 22nd International Conference on Raman Spectroscopy. 2010: Boston, MA. p. 424-425.
- 116. R. Rabah, R. Weber, G.K. Serhatkulu, A. Cao, H. Dai, A. Pandya, R. Naik, G. Auner, J. Poulik, and M. Klein, "Diagnosis of Neuroblastoma and Ganglioneuroma Using Raman Spectroscopy," Journal of Pediatric Surgery. vol. 43, no. 1, Jan. 2008, pp. 171-176.
- J.H. Kim, J.S. Kim, H. Choi, S.M. Lee, B.H. Jim, K.N. Yu, E. Kuk, Y.K. Kim, D.H. Jeong, M.H. Cho, and Y.S. Lee, "Nanoparticle Probes with Surface Enhanced Raman Spectroscopic Tags (Sers Dots) for Cellular Cancer Targeting," Nanomedicine-Nanotechnology Biology and Medicine. vol. 2, no. 4, Dec. 2006.
- 118. K.W. Short, S. Carpenter, J.P. Freyer, and J.R. Mourant, "Raman Spectroscopy Detects Biochemical Changes Due to Proliferation in Mammalian Cell Cultures," Biophysical Journal. vol. 88, no. 6, Jun. 2005.
- 119. B. Chen, S. Li, J. Li, Z. Guo, Q. Chen, and H. Mai, "Optimal Multivariate Method for Raman Spectroscopy Based Diagnosis of Nasopharyngeal Carcinoma," Journal of Applied Physics. vol. 114, no. 24, Dec 28. 2013.
- 120. G.R. Lloyd, L.M. Almond, N. Stone, N. Shepherd, S. Sanders, J. Hutchings, H. Barr, and C. Kendall, "Utilising Non-Consensus Pathology Measurements to Improve the Diagnosis of Oesophageal Cancer Using a Raman Spectroscopic Probe," Analyst. vol. 139, no. 2, 2014. 2014, pp. 381-388.
- L.M. Almond, J. Hutchings, G. Lloyd, H. Barr, N. Shepherd, J. Day, O. Stevens, S. Sanders, M. Wadley, N. Stone, and C. Kendall, "Endoscopic Raman Spectroscopy

- Enables Objective Diagnosis of Dysplasia in Barrett's Esophagus," Gastrointestinal Endoscopy. vol. 79, no. 1, Jan. 2014, pp. 37-45.
- 122. Z. Liu, C. Davis, W. Cai, L. He, X. Chen, and H. Dai, "Circulation and Long-Term Fate of Functionalized, Biocompatible Single-Walled Carbon Nanotubes in Mice Probed by Raman Spectroscopy," Proceedings of the National Academy of Sciences of the United States of America. vol. 105, no. 5, Feb 5. 2008, pp. 1410-1415.
- 123. F. Bonnier and H.J. Byrne, "Understanding the Molecular Information Contained in Principal Component Analysis of Vibrational Spectra of Biological Systems," Analyst. vol. 137, no. 2, 2012. 2012.
- 124. A. Shapiro, O.N. Gofrit, G. Pizov, J.K. Cohen, and J. Maier, "Raman Molecular Imaging: A Novel Spectroscopic Technique for Diagnosis of Bladder Cancer in Urine Specimens," European Urology. vol. 59, no. 1, Jan. 2011, pp. 106-112.
- 125. S. Zong, Z. Wang, H. Chen, and Y. Cui, "Ultrasensitive Telomerase Activity Detection by Telomeric Elongation Controlled Surface Enhanced Raman Scattering," Small. vol. 9, no. 24, Dec 20. 2013, pp. 4215-4220.
- 126. T. Bhattacharjee, P. Kumar, G. Maru, A. Ingle, and C.M. Krishna, "Swiss Bare Mice: A Suitable Model for Transcutaneous in Vivo Raman Spectroscopic Studies of Breast Cancer," Lasers in Medical Science. vol. 29, no. 1, Jan. 2014, pp. 325-333.
- 127. A. Sahu, K. Dalal, S. Naglot, P. Aggarwal, and C.M. Krishna, "Serum Based Diagnosis of Asthma Using Raman Spectroscopy: An Early Phase Pilot Study," Plos One. vol. 8, no. 11, Nov 8. 2013.

- 128. L.M. Fullwood, D. Griffiths, K. Ashton, T. Dawson, R.W. Lea, C. Davis, F. Bonnier, H.J. Byrne, and M.J. Baker, "Effect of Substrate Choice and Tissue Type on Tissue Preparation for Spectral Histopathology by Raman Microspectroscopy," Analyst. vol. 139, no. 2, 2014. 2014, pp. 446-454.
- 129. R. Mehrotra, D.K. Jangir, S. Agarwal, B. Ray, P. Singh, and A.K. Srivastava, "Interaction Studies of Anticancer Drug Lomustine with Calf Thymus Dna Using Surface Enhanced Raman Spectroscopy," Mapan-Journal of Metrology Society of India. vol. 28, no. 4, Dec. 2013, pp. 273-277.
- 130. H. Schulz and M. Baranska, "Identification and Quantification of Valuable Plant Substances by Ir and Raman Spectroscopy," Vibrational Spectroscopy. vol. 43, no. 1, Jan 16. 2007.
- 131. I. Notingher, C. Green, C. Dyer, E. Perkins, N. Hopkins, C. Lindsay, and L.L. Hench, "Discrimination between Ricin and Sulphur Mustard Toxicity in Vitro Using Raman Spectroscopy," Journal of the Royal Society Interface. vol. 1, no. 1, Nov 22. 2004.
- 132. C.J. Frank, R.L. McCreery, and D.C.B. Redd, "Raman-Spectroscopy of Normal and Diseased Human Breast Tissues," Analytical Chemistry. vol. 67, no. 5, Mar 1. 1995, pp. 777-783.
- 133. J. Laska and J. Widlarz, "Spectroscopic and Structural Characterization of Low Molecular Weight Fractions of Polyaniline," Polymer. vol. 46, no. 5, Feb 14. 2005.
- 134. E. Katainen, M. Elomaa, U.-M. Laakkonen, E. Sippola, P. Niemela, J. Suhonen, and K. Jarvinen, "Quantification of the Amphetamine Content in Seized Street Samples by Raman Spectroscopy," Journal of Forensic Sciences. vol. 52, no. 1, Jan. 2007.

- 135. Z.W. Huang, H. Lui, D.I. McLean, M. Korbelik, and H.S. Zeng, "Raman Spectroscopy in Combination with Background near-Infrared Autofluorescence Enhances the in Vivo Assessment of Malignant Tissues," Photochemistry and Photobiology. vol. 81, no. 5, Sep-Oct. 2005.
- 136. L. Seballos, J.Z. Zhang, and R. Sutphen, "Surface-Enhanced Raman Scattering Detection of Lysophosphatidic Acid," Analytical and Bioanalytical Chemistry. vol. 383, no. 5, Nov. 2005.
- 137. G.I. Dovbeshko, N.Y. Gridina, E.B. Kruglova, and O.P. Pashchuk, "FTIR Spectroscopy Studies of Nucleic Acid Damage," Talanta. vol. 53, no. 1, Oct 2. 2000.
- 138. P.G.L. Andrus and R.D. Strickland, "Cancer Grading by Fourier Transform Infrared Spectroscopy," Biospectroscopy. vol. 4, no. 1, 1998. 1998.
- 139. S. Mordechai, R.K. Sahu, Z. Hammody, S. Mark, K. Kantarovich, H. Guterman, A. Podshyvalov, J. Goldstein, and S. Argov, "Possible Common Biomarkers from FTIR Microspectroscopy of Cervical Cancer and Melanoma," Journal of Microscopy-Oxford. vol. 215, Jul. 2004, pp. 86-91.
- 140. L. Chiriboga, P. Xie, H. Yee, V. Vigorita, D. Zarou, D. Zakim, and M. Diem, "Infrared Spectroscopy of Human Tissue. I. Differentiation and Maturation of Epithelial Cells in the Human Cervix," Biospectroscopy. vol. 4, no. 1, 1998. 1998.
- 141. S.M. Ronen, A. Stier, and H. Degani, "Nmr-Studies of the Lipid-Metabolism of T47d Human Breast-Cancer Spheroids," Febs Letters. vol. 266, no. 1-2, Jun 18. 1990.
- 142. B.R. Wood, M.A. Quinn, B. Tait, M. Ashdown, T. Hislop, M. Romeo, and D. McNaughton, "FTIR Microspectroscopic Study of Cell Types and Potential Confounding

- Variables in Screening for Cervical Malignancies," Biospectroscopy. vol. 4, no. 2, 1998.
- 143. K. Kachrimanis, D.E. Braun, and U.J. Griesser, "Quantitative Analysis of Paracetamol Polymorphs in Powder Mixtures by Ft-Raman Spectroscopy and Pls Regression," Journal of Pharmaceutical and Biomedical Analysis. vol. 43, no. 2, Jan 17. 2007.
- 144. A. Singha, A. Ghosh, A. Roy, and N.R. Ray, "Quantitative Analysis of Hydrogenated Diamondlike Carbon Films by Visible Raman Spectroscopy," Journal of Applied Physics. vol. 100, no. 4, Aug 15. 2006.
- 145. M.F.K. Fung, M.K. Senterman, N.Z. Mikhael, S. Lacelle, and P.T.T. Wong, "Pressure-Tuning Fourier Transform Infrared Spectroscopic Study of Carcinogenesis in Human Endometrium," Biospectroscopy. vol. 2, no. 3, 1996. 1996.
- 146. H. Barr, T. Dix, and N. Stone, "Optical Spectroscopy for the Early Diagnosis of Gastrointestinal Malignancy," Lasers in Medical Science. vol. 13, no. 1, 1998. 1998.
- 147. G.W. Lucassen, G.N. van Veen, and J.A. Jansen, "Band Analysis of Hydrated Human Skin Stratum Corneum Attenuated Total Reflectance Fourier Transform Infrared Spectra in Vivo," Journal of biomedical optics. vol. 3, no. 3, 1998-Jul. 1998.
- 148. S. Mazurek and R. Szostak, "Quantitative Determination of Captopril and Prednisolone in Tablets by FT-Raman Spectroscopy," Journal of Pharmaceutical and Biomedical Analysis. vol. 40, no. 5, Mar 18. 2006.
- 149. G. Quintas, S. Garrigues, A. Pastor, and M. de la Guardia, "Ft-Raman Determination of Mepiquat Chloride in Agrochemical Products," Vibrational Spectroscopy. vol. 36, no. 1, Oct 18. 2004.

- 150. R. Agarwal, P. Tandon, and V.D. Gupta, "Phonon Dispersion in Poly(Dimethylsilane),"

  Journal of Organometallic Chemistry. vol. 691, no. 13, Jun 15. 2006.
- 151. C. Ortiz, D.M. Zhang, Y. Xie, A.E. Ribbe, and D. Ben-Amotz, "Validation of the Drop Coating Deposition Raman Method for Protein Analysis," Analytical Biochemistry. vol. 353, no. 2, Jun 15. 2006.
- 152. H. Behrens, J. Roux, D.R. Neuville, and M. Siemann, "Quantification of Dissolved H<sub>2</sub>O in Silicate Glasses Using Confocal Microraman Spectroscopy," Chemical Geology. vol. 229, no. 1-3, May 16. 2006.

*Table 1.* The spectral interpretations

Peak	Assignment	Reference Number
415cm <sup>-1</sup>	Phosphatidylinositol	71
418cm <sup>-1</sup>	Cholesterol	71
428cm <sup>-1</sup>	Symmetric stretching vibration of v <sub>2</sub> PO <sub>4</sub> <sup>3</sup> -(phosphate of HA)	50
429cm <sup>-1</sup>	Cholesterol, cholesterol ester	71
445cm <sup>-1</sup>	N-C-S stretch (one of three thiocyanate peaks, with 2095 & 735 cm <sup>-1</sup> )	104
447/54 cm <sup>-1</sup>	Ring torsion of Phenyl(2)	121
477cm <sup>-1</sup>	Polysaccharides(amylase, amylopectin)	64
481cm <sup>-1</sup>	DNA	110
484-90cm <sup>-1</sup>	Glycogen	31
490cm <sup>-1</sup>	Glycogen	30
505/8cm <sup>-1</sup>	C-OH <sub>3</sub> torsion of methoxy group(1)	121
509cm <sup>-1</sup>	S-S disulfide stretching band of collagen	50
	v(S-S) gauche-gauche (aminoacid cysteine)	64

519 cm <sup>-1</sup>	Phosphatidylinositol	70
524cm <sup>-1</sup>	S-S disulfide stretching in proteins	30, 31
	Phosphatidylserine	71
535cm <sup>-1</sup>	cholesterol ester	28
	v(S-S) gauche-gauche-trans (aminoacid cysteine)	64
538 cm <sup>-1</sup>	Cholesterol ester	71
540cm <sup>-1</sup>	v(S-S) trans-gauche-trans (aminoacid cysteine)	64
548 cm <sup>-1</sup>	Cholesterol	71
540cm <sup>-</sup>	Glucose-saccharide band (overlaps with acyl band)	71
573cm-1	Tryptophan/cytosine, guanine	31
576 cm <sup>-1</sup>	Phosphatidylinositol	71
583/6cm <sup>-1</sup>	OH out of plane bending (free)	121
589cm <sup>-1</sup>	Symmetric stretching vibration of v <sub>4</sub> PO <sub>4</sub> <sup>3-</sup> (phosphate	50
	of HA)	
	Glycerol	71
Peak	Assignment	Reference
		Number
596 cm <sup>-1</sup>	Phosphatidylinositol	71

600-800cm <sup>-1</sup>	Nucleotide conformation	103
607cm <sup>-1</sup>	Glycerol	71
608cm <sup>-1</sup>	Cholesterol	71
614 cm <sup>-1</sup>	Cholesterol ester	71
618cm <sup>-1</sup>	C-C twisting (protein)	103
620cm <sup>-1</sup>	C-C twist aromatic ring (one of C-C vibrations to be	111
	expected in aromatic structure of Xylene)	
621cm <sup>-1</sup>	C-C twisting mode of phenylalanine (proteins)	30, 31, 122
630cm <sup>-1</sup>	Glycerol	71
630-70cm <sup>-1</sup>	v(C-S) gauche (aminoacid methionine)	64
639 cm <sup>-1</sup>	Tyrosine ring breathing	39
640cm <sup>-1</sup>	C-S stretching & C-C twisting of proteins-tyrosine	103
643cm <sup>-1</sup>	C-C twisting mode of tyrosine	31, 50
645cm <sup>-1</sup>	C-C twisting mode of phenylalanine (proteins)	122
646cm <sup>-1</sup>	C-C twisting mode of tyrosine	50
662cm <sup>-1</sup>	C-S stretching mode of cystine (collagen type I)	30, 50
666cm <sup>-1</sup>	G, T (ring breathing modes in the DNA bases)-	103
	tyrosine-G backbone in RNA	
667/9cm <sup>-1</sup>	C-S stretching mode of cystine (collagen type I)	30, 50
	T, G (DNA/RNA)	122

669cm <sup>-1</sup>	C-S stretching mode of cytosine	31
669cm <sup>-1</sup>	$v_7(\delta)$ : Porphyrin deformation), observed in the spectra of single human RBC	98
671cm <sup>-1</sup>	Ring breathing of the Tryptophan	39
678 cm <sup>-1</sup>	Ring breathing modes in the DNA bases	103
	G (ring breathing modes in the DNA bases)/C-2'-endo-anti	
700-45cm <sup>-1</sup>	v(C-S) trans (aminoacid methionine)	64
702 cm <sup>-1</sup>	Cholesterol, cholesterol ester	71
717-9cm <sup>-1</sup>	C-N (membrane phospholipids head)/adenine	31
	CN <sup>+</sup> (CH <sub>3</sub> ) <sub>3</sub> (lipids)	122
718cm <sup>-1</sup>	Choline group	71
Peak	Assignment	Reference
		Number
719cm <sup>-1</sup>	C-N (membrane phospholipid head)/nucleotide peak	30
	Symmetric stretch vibration of choline group	71
	N <sup>+</sup> (CH <sub>3</sub> ) <sub>3</sub> , characteristic for phospholipids	
	Phosphatidylcholine, sphingomyelin	71
	C-C-N+ symmetric stretching in phosphatidylcholine (lipid assignment)	122

720/2cm <sup>-1</sup>	DNA	110
724 cm <sup>-1</sup>	Nucleic acids	59
725cm <sup>-1</sup>	A (ring breathing mode of DNA/RNA bases)	103
726cm <sup>-1</sup>	C-S (protein), CH <sub>2</sub> rocking, adenine	31
727/8cm <sup>-1</sup>	C-C stretching, proline (collagen assignment)	123
	Lipid	141
728 cm <sup>-1</sup>	Ring breathing of Tryptophan	39
729cm <sup>-1</sup>	A	122
733cm <sup>-1</sup>	Phosphatidylserine	71
735cm <sup>-1</sup>	C-S stretch (one of three thiocyanate peaks, with 2095 & 445 cm <sup>-1</sup> )	104
742 cm <sup>-1</sup>	DNA, Tryptophan	38
746cm <sup>-1</sup>	T (ring breathing mode of DNA/RNA bases)	103
748cm <sup>-1</sup>	DNA	110
749cm <sup>-1</sup>	Symmetric breathing of tryptophan (protein assignment)	20, 30, 50
750cm <sup>-1</sup>	CH <sub>2,6</sub> out-of-plane bending, observed in the spectra of single human RBC	121
	Lactic acid	110
752cm <sup>-1</sup>	$\nu_{15}$ (Porphyrin breathing mode), (the most informative about the status of RBC & a direct measure of the	98

	heme groups of the hemoglobins)	
	DNA	110
752/3/4/5cm <sup>-1</sup>	Symmetric breathing of tryptophan (protein	20, 30, 50
	assignment)	
755/6cm <sup>-1</sup>	Symmetric breathing of tryptophan	31, 67
759cm <sup>-1</sup>	Tryptophan	31
	Ethanolamine group	71
	Phosphatidylethanolamine	71
760cm <sup>-1</sup>	Tryptophan, δ(ring)	64
	Ring breathing Tryptophan (proteins)	122
Peak	Assignment	Reference
Peak	Assignment	Reference Number
Peak 766cm <sup>-1</sup>	Assignment  Pyrimidine ring breathing mode	
		Number
766cm <sup>-1</sup>	Pyrimidine ring breathing mode	Number 69
766cm <sup>-1</sup> 776cm <sup>-1</sup>	Pyrimidine ring breathing mode  Phosphatidylinositol	<b>Number</b> 69 71
766cm <sup>-1</sup> 776cm <sup>-1</sup> 780cm <sup>-1</sup>	Pyrimidine ring breathing mode  Phosphatidylinositol  Uracil based ring breathing mode	Number  69  71  69
766cm <sup>-1</sup> 776cm <sup>-1</sup> 780cm <sup>-1</sup> 781cm <sup>-1</sup>	Pyrimidine ring breathing mode  Phosphatidylinositol  Uracil based ring breathing mode  Cytosine/Uracil ring breathing (Nucleotide)	Number  69  71  69  31, 30
766cm <sup>-1</sup> 776cm <sup>-1</sup> 780cm <sup>-1</sup> 781cm <sup>-1</sup>	Pyrimidine ring breathing mode  Phosphatidylinositol  Uracil based ring breathing mode  Cytosine/Uracil ring breathing (Nucleotide)  DNA	Number  69  71  69  31, 30  110, 122

	bases)	
784/5cm <sup>-1</sup>	Phosphodiester; cytosine	106
785cm <sup>-1</sup>	U, T, C (ring breathing modes in the DNA/RNA	103
	bases)	
	Backbone O-P-O	
786cm <sup>-1</sup>	DNA: O-P-O, cytosine, uracil, thymine	31
	Pyrimidine ring breathing mode	69
787cm <sup>-1</sup>	Can be taken as a measure for the relative quantity of	102
	nucleic acids present	
	Phosphatidylserine	71
788cm <sup>-1</sup>	C <sub>5</sub> '-O-P-O-C <sub>3</sub> ' phosphodiester bands in DNA	122
	DNA	122
	O-P-O stretching DNA	37
791cm <sup>-1</sup>	Pyrimidine	37
800-1200cm <sup>-1</sup>	Backbone geometry and phosphate ion interactions	103
802cm <sup>-1</sup>	Uracil based ring breathing mode	69
810cm <sup>-1</sup>	Phosphodiester (Z-marker)	106
811cm <sup>-1</sup>	O-P-O stretching RNA	122
812cm <sup>-1</sup>	Phosphodiester (Z-marker)	106
813cm <sup>-1</sup>	One of the two most distinct peaks for RNA (with	103

	1240cm <sup>-1</sup> )	
813cm <sup>-1</sup>	C-C stretching (collagen assignment)	123
	C <sub>5</sub> '-O-P-O-C <sub>3</sub> ' phosphodiester bands in RNA	122
	RNA	122
815cm <sup>-1</sup>	Proline, hydroxyproline, tyrosine, v <sub>2</sub> PO <sub>2</sub> stretch of nucleic acids	50
816cm <sup>-1</sup>	d (CCH) aliphatic of collagen	28
817cm <sup>-1</sup>	C-C stretching (collagen assignment)	123
820cm <sup>-1</sup>	Protein band	2, 3
	Structural protein modes of tumors	27
		<b>D</b> 0
Peak	Assignment	Reference
Peak	Assignment	Number
Peak 820cm <sup>-1</sup>	Assignment Proteins, including collagen I	
		Number
820cm <sup>-1</sup>	Proteins, including collagen I	Number 110
820cm <sup>-1</sup> 820-930cm <sup>-1</sup>	Proteins, including collagen I  C-C stretch of proline and hydroxyproline	Number 110 42
820cm <sup>-1</sup> 820-930cm <sup>-1</sup> 822cm <sup>-1</sup>	Proteins, including collagen I  C-C stretch of proline and hydroxyproline  Phosphodiester	Number 110 42 106
820cm <sup>-1</sup> 820-930cm <sup>-1</sup> 822cm <sup>-1</sup>	Proteins, including collagen I  C-C stretch of proline and hydroxyproline  Phosphodiester  Out-of-plane ring breathing, tyrosine (protein	Number 110 42 106
820cm <sup>-1</sup> 820-930cm <sup>-1</sup> 822cm <sup>-1</sup> 823cm <sup>-1</sup>	Proteins, including collagen I  C-C stretch of proline and hydroxyproline  Phosphodiester  Out-of-plane ring breathing, tyrosine (protein assignment)	Number  110  42  106  20
820cm <sup>-1</sup> 820-930cm <sup>-1</sup> 822cm <sup>-1</sup> 823cm <sup>-1</sup>	Proteins, including collagen I  C-C stretch of proline and hydroxyproline  Phosphodiester  Out-of-plane ring breathing, tyrosine (protein assignment)  Phosphodiester	Number  110  42  106  20

828cm <sup>-1</sup>	Out-of-plane ring breathing, tyrosine/O-P-O stretch	31, 30
	DNA	
	Phosphodiester	106
	O-P-O stretching DNA/RNA	122
	Ring breathing tyrosine	122
830cm <sup>-1</sup>	Proline, hydroxyproline, tyrosine, v <sub>2</sub> PO <sub>2</sub> stretch of nucleic acids	50
	C-H out of plane bending in benzoid ring	124
830cm <sup>-1</sup>	Tyrosine (Fermi resonance of ring fundamental and	64
	overtone)	
831cm <sup>-1</sup>	Asymmetric O-P-O stretching, tyrosine	103
838cm <sup>-1</sup>	Deformative vibrations od amine groups	124
840cm <sup>-1</sup>	α-anomers	71
	Glucose-saccharide band (overlaps with acyl band)	71
	Saccharide (α)	71
840-60cm <sup>-1</sup>	Polysaccharide structure	53
842cm <sup>-1</sup>	Glucose	31
847cm <sup>-1</sup>	Monosaccharides (α-glucose), (C-O-C) skeletal mode	64
	Disaccharide (maltose), (C-O-C) skeletal mode	64
850cm <sup>-1</sup>	Most probably due to single bond stretching vibrations	53
	for the amino acids and valine and polysaccharides	

	Tyrosine (Fermi resonance of ring fundamental and overtone)	64
850-950cm <sup>-1</sup>	Signal free area of amphetamine	125
852cm <sup>-1</sup>	Proline, hydroxyproline, tyrosine	50
	Tyrosine ring breathing	103
	Glycogen	110
853cm <sup>-1</sup>	Ring breathing mode of tyrosine & C-C stretch of	31, 30
	proline ring	
	Glycogen	110
Peak	Assignment	Reference
		Number
854cm <sup>-1</sup>	(C-O-C) skeletal mode of $\alpha$ -anomers (polysaccharides,	64
	pectin)	
	Ring breathing tyrosine (proteins)	100
		122
855cm <sup>-1</sup>	Proline, tyrosine	20
855cm <sup>-1</sup>	Proline, tyrosine $\nu(\text{C-C}), \text{ proline+}\delta(\text{CCH})\text{ring breathing, tyrosine}$	
855cm <sup>-1</sup>	·	20
855cm <sup>-1</sup>	$\nu$ (C-C), proline+ $\delta$ (CCH)ring breathing, tyrosine	20
855cm <sup>-1</sup>	$\nu$ (C-C), proline+ $\delta$ (CCH)ring breathing, tyrosine (protein assignment and polysaccharide) $\delta$ (CCH) phevylalanine, olefinic (protein assignment and polysaccharide)	20 20 126
855cm <sup>-1</sup>	$\nu$ (C-C), proline+ $\delta$ (CCH)ring breathing, tyrosine (protein assignment and polysaccharide) $\delta$ (CCH) phevylalanine, olefinic (protein assignment	20 20

	C-C stretching, proline (collagen assignment)	123
856cm <sup>-1</sup>	Amino acid side chain vibrations of proline & hydroxyproline, as well as a (C-C) vibration of the	50
	collagen backbone Hydroxyproline (collagen type I)	
859 cm <sup>-1</sup>	Tyrosine, collagen	31
860cm <sup>-1</sup>	Phosphate group	71
	Phosphatidic acid	71
867cm <sup>-1</sup>	Ribose vibration, one of the distinct RNA modes (with	103
	915 and 974cm <sup>-1</sup> )	
868/870/872 cm <sup>-</sup>	Lipid	141
868cm <sup>-1</sup>	C-C stretching, hypro (collagen assignment)	123
	Monosaccharides (β-fructose), (C-O-C) skeletal mode	64
	Disaccharide (sucrose), (C-O-C) skeletal mode	64
	Polysaccharides, amylase	64
	Polysaccharides, amylopectin	64
869cm <sup>-1</sup>	Proline	31
870cm <sup>-1</sup>	Most probably due to single bond stretching vibrations	53
	for the amino acids proline and valine and	
	polysaccharides	
	C-C stretching, hypro (collagen assignment)	123

873cm <sup>-1</sup>	Hydroxyproline, tryptophan	50
874cm <sup>-1</sup>	C-C stretching, hypro (collagen assignment)	123
875cm <sup>-1</sup>	Antisymmetric stretch vibration of choline group	71
	N <sup>+</sup> (CH <sub>3</sub> ) <sub>3</sub> , characteristic for phospholipids	
	Phosphatidylcholine, sphingomyelin	71
876cm <sup>-1</sup>	ν(C-C), hydroxyproline (protein assignment)	20
	C-C stretching, hydroxyproline (collagen assignment)	123
Peak	Assignment	Reference
		Number
877cm <sup>-1</sup>	C-C-N <sup>+</sup> symmetric stretching (lipids)	122
	C-O-C ring (carbohydrate)	122
879cm <sup>-1</sup>	Hydroxyproline, tryptophan	50
880cm <sup>-1</sup>	Tryptophan, $\delta(\text{ring})$	64
883cm <sup>-1</sup>	ρ (CH <sub>2</sub> ) (protein assignment)	126
884cm <sup>-1</sup>	Proteins, including collagen I	110
885cm <sup>-1</sup>	Disaccharide (cellobiose), (C-O-C) skeletal mode	64
889cm <sup>-1</sup>	Methylene rocking	127
890cm <sup>-1</sup>	Protein bands	2, 3
	Structural protein modes of tumors	27
	β-anomers	71

891cm <sup>-1</sup>	Saccharide band (overlaps with acyl band)	71
893cm <sup>-1</sup>	Backbone, C-C skeletal	103
893/5/6cm <sup>-1</sup>	Phosphodiester, Deoxyribose	106
898cm <sup>-1</sup>	Monosaccharides (β-glucose), (C-O-C) skeletal mode	64
	Disaccharide (maltose), (C-O-C) skeletal mode	64
	Adenine	30
904cm <sup>-1</sup>	C-C skeletal stretching	39
906cm <sup>-1</sup>	Tyrosine	37
907cm <sup>-1</sup>	Formalin contamination peak on fixed tissues	35
912cm <sup>-1</sup>	Calcium Oxalate	54
913cm <sup>-1</sup>	Glucose	71
915cm <sup>-1</sup>	Ribose vibration, one of the distinct RNA modes (with	103
	915 and 974cm <sup>-1</sup> )	
918cm <sup>-1</sup>	Proline, hydroxyproline	50
	Glycogen and lactic acid	110
920cm <sup>-1</sup>	C-C stretch of proline ring/glucose/lactic acid	31, 30
	C-C, praline ring (collagen assignment)	123
921 cm <sup>-1</sup>	Proline ring/glucose/lactic acid/praline ring	51
922 cm <sup>-1</sup>	C-C stretch	28
928-40cm <sup>-1</sup>	v(C-C),stretching-probably in amino acids proline &	56

	valine (protein band)	
931cm <sup>-1</sup>	Carbohydrates peak for solutions and solids	3
932cm <sup>-1</sup>	Skeletal C-C, α-helix	31
933cm <sup>-1</sup>	Proline, hydroxyproline, v(C-C) skeletal of collagen	50
	backbone	
Peak	Assignment	Reference
		Number
934cm <sup>-1</sup>	C-C backbone (collagen assignment)	123
935cm <sup>-1</sup>	C-C stretching mode of proline & valine & protein	20, 30
	backbone (α-helix conformation) /glycogen (protein	
	assignment)	
	P(CH <sub>3</sub> ) terminal, proline, valine + $\nu$ (CC) $\alpha$ -helix	31
	keratin (protein assignment)	
937cm <sup>-1</sup>	Proline(collagen type I)	50
	Amino acid side chain vibrations of proline and	50
	hydroxyproline, as well as a	
	(C-C) vibration of the collagen backbone	
	C-C backbone (collagen assignment)	123
	Glycogen	110
	ν (C-C) residues (α-helix)	70
	C-C stretching, α-helix (proteins)	122

	C-O-C glycodides (carbohydrates)	122
	Collagen	59
937/8cm <sup>-1</sup>	Proline, hydroxyproline, v(C-C) skeletal of collagen	50
	backbone	
938cm <sup>-1</sup>	C-C stretch backbone	31
941cm <sup>-1</sup>	Skeletal modes (polysaccharides, amylose)	64
	Skeletal modes (polysaccharides, amylopectin)	64
950cm <sup>-1</sup>	Most probably due to single bond stretching vibrations	53
	for the amino acids proline and valine and	
	polysaccharides	
	Calcium Phosphate stretch band	51
950-1050cm <sup>-1</sup>	Amphetamine has a group of three bands at this region	125
951cm <sup>-1</sup>	$v_s$ (CH <sub>3</sub> ) of proteins ( $\alpha$ -helix)	70
956cm <sup>-1</sup>	Crotenoids (absent in normal tissues)	1
957cm <sup>-1</sup>	Hydroxyapatite, carotenoid, cholesterol	31
960cm <sup>-1</sup>	Symmetric stretching vibration of v <sub>1</sub> PO <sub>4</sub> <sup>3-</sup> (phosphate	50
	of HA)	
	Calcium –Phosphate stretch band (high quantities of	3, 87
	cholesterol)	
	Quinoid ring in-plane deformation	124
	Calcium hydroxyapatite	68

962cm <sup>-1</sup>	Phoisphate symmetric stretching vibration of calcium hydroxyapatite	94
963cm <sup>-1</sup>	Unassigned in protein assignments	20
	CH <sub>2,6</sub> out-of-plane bending	121
966cm <sup>-1</sup>	Hydroxyapatite	31
Peak	Assignment	Reference Number
968cm <sup>-1</sup>	Lipids	3
970cm <sup>-1</sup>	Phosphate monoester groups of phosphorylated proteins & cellular nucleic acids	3
971cm <sup>-1</sup>	ν(C-C) wagging	70
972cm <sup>-1</sup>	Lipid	141
972/3cm <sup>-1</sup>	C-C backbone (collagen assignment)	123
973cm <sup>-1</sup>	$\rho(CH_3)$ , $\delta(CCH)$ olefinic (protein assignment)	126
974cm <sup>-1</sup>	Ribose vibration, one of the distinct RNA modes (with 874 and 915cm <sup>-1</sup> )	103
980cm <sup>-1</sup>	C-C stretching β-sheet (proteins)	122
991cm <sup>-1</sup>	Single human RBC, Phenylalanine, NADH	38
996cm <sup>-1</sup>	C-O ribose, C-C	3
999cm <sup>-1</sup>	$v_{45}(CC)$ , observed in the spectra of single human RBC	98
1000cm <sup>-1</sup>	Phenylalanine	76

	Bound & free NADH	76
1001cm <sup>-1</sup>	Symmetric ring breathing mode of phenylalanine	31, 30, 52
1002cm <sup>-1</sup>	C-C aromatic ring stretching	111
	Phenylalanine	76
1002cm <sup>-1</sup>	Phenylalanine	50
	Phenylalanine (collagen assignment)	123
1003cm <sup>-1</sup>	Phenylalanine, C-C skeletal	103
1004cm <sup>-1</sup>	Phenylalanine ( of collagen)	50
	$\nu_s$ (C-C), Symmetric ring breathing ,phenylalanine	20, 126
	(protein assignment)	
	Phenylalanine (collagen assignment)	123
	Phenyl breathing mode	126
	ν(C-C) phenylalanine	70
1005cm <sup>-1</sup>	Phenylalanine (proteins)	122
	Proteins	122
	Symmetric ring breathing of phenylalanine	122
	Carotenoids	141
1006cm <sup>-1</sup>	Carotenoids (absent in normal tissues)	1
	Phenylalanine, δ(ring)	64
1007cm <sup>-1</sup>	Phenylalanine, carbamide	37

Phenylalanine	102
$\nu$ (CO), $\nu$ (CC), $\delta$ (OCH), ring (polysaccharides, pectin)	64
Assignment	Reference
	Number
Tryptophan ring breathing	52
Carbohydrates peak for solids	3
Ribose	51
Stretching C-O ribose	128
Glycogen	3
Glycogen	3
Carbohydrates peak for solutions	3
Glycogen	3, 129
O-CH <sub>3</sub> stretching of methoxy groups	121
Phenylalanine of collagen	50
ν (CC) skeletal, keratin (protein assignment)	126
C-H bending	52
$\delta$ (C-H), phenylalanine (protein assignment)	20
C-H in-plane bending mode of phenylalanine	30
Carbohydrate residues of collagen	3
Phenylalanine, C-N stretching of proteins	103
	Assignment  Tryptophan ring breathing Carbohydrates peak for solids Ribose Stretching C-O ribose Glycogen Glycogen Carbohydrates peak for solutions Glycogen  O-CH <sub>3</sub> stretching of methoxy groups Phenylalanine of collagen v (CC) skeletal, keratin (protein assignment) C-H bending δ(C-H), phenylalanine (protein assignment) C-H in-plane bending mode of phenylalanine Carbohydrate residues of collagen

C-H in-planebending mode of phenylalanine	31
CH <sub>2</sub> CH <sub>3</sub> bending modes of collagen & phospholipids	20
C-C skeletal stretch (one of C-C ring vibration to be	111
expected in aromatic structure of Xylene)	
Phenylalanine of collagen	50
Proline (collagen assignment)	123
Differences in collagen content	3
Phenylalanine mode	103
v(CO), v(CC), v(CCO) (polysaccharides, pectin)	64
C-H in-plane phenylalanine (proteins)	122
Phenylalanine of collagen	50
Collagen	130
Formalin peaks appearing in the fixed normal and	131
tumor tissues	
Carbohydrates peak for solutions and solids	3
Proline (collagen assignment)	123
v <sub>3</sub> PO <sub>4</sub> <sup>3-</sup> (symmetric stretching vibration of v <sub>3</sub> PO <sub>4</sub> <sup>3-</sup> of	50
HA)	
Proline	51
Glycogen	110
	C-C skeletal stretch (one of C-C ring vibration to be expected in aromatic structure of Xylene)  Phenylalanine of collagen  Proline (collagen assignment)  Differences in collagen content  Phenylalanine mode  v(CO), v(CC), v(CCO) (polysaccharides, pectin)  C-H in-plane phenylalanine (proteins)  Phenylalanine of collagen  Collagen  Formalin peaks appearing in the fixed normal and tumor tissues  Carbohydrates peak for solutions and solids  Proline (collagen assignment)  v <sub>3</sub> PO <sub>4</sub> <sup>3-</sup> (symmetric stretching vibration of v <sub>3</sub> PO <sub>4</sub> <sup>3-</sup> of HA)  Proline

1053cm <sup>-1</sup>	C-O stretching, C-N stretching (protein)	103
Peak	Assignment	Reference Number
1055cm <sup>-1</sup>	In the solid, the most significant difference between the 2 nucleic acids is the ratio intensity of the bands in this area	3
1057cm <sup>-1</sup>	Lipids	3
1060-95cm <sup>-1</sup>	PO <sub>2</sub> stretching (DNA/RNA)	122
	Chain C-C stretching (lipids)	122
	C-O, C-C stretching (carbohydrates)	122
1060-130cm <sup>-1</sup>	C-C skeletal stretching	127
1061cm <sup>-1</sup>	C-C in-plane bending (one of C-C ring vibration to be expected in aromatic structure of Xylene)	111
	C-N stretching	52
	Ceramide	91
1063cm <sup>-1</sup>	C-C skeletal stretch random conformation	111
1064cm <sup>-1</sup>	Skeletal c-c stretch of lipids	31
	Acyl chains	71
	ν(C-C) trans	70
1065cm <sup>-1</sup>	Palmitic acid	71
	Fatty acid	71

	Proline	51
1066/7cm <sup>-1</sup>	Proline (collagen assignment)	123
1070cm <sup>-1</sup>	Triglycerides (fatty acids)	94
1070-90cm <sup>-1</sup>	Symmetric PO <sub>2</sub> stretching of DNA (represents more DNA in cell)	132
1071cm <sup>-1</sup>	Glucose	71
1073cm <sup>-1</sup>	Carbonate symmetric stretching vibration of calcium carbonate apatite	94
	Triglycerides (fatty acids)	94
1074cm <sup>-1</sup>	Glucose, Triglycerides, C-C (lipid)	38
1076cm <sup>-1</sup>	C-C (lipid in normal tissues)	76
	Symmetric stretching vibration of v3PO <sub>4</sub> <sup>3-</sup> (phosphate of HA)	50
1078cm <sup>-1</sup>	$\nu(C-C)$ or $\nu(C-O)$ , phospholipids (lipid assignment)	20
	Pronounced symmetric phosphate stretch	20
	Phospholipids	20
	C-C or C-O stretching mode of phospholipids	20
	Carbohydrate peak for solids	3
	C-C or C-O stretch (lipid), C-C or PO <sub>2</sub> stretch (nucleic acid)	31
	v(CC) skeletal	126

Peak	Assignment	Reference
Tean	rissignment	Number
1078cm <sup>-1</sup>	ν(CC) vitor <sub>s</sub> (PO <sub>2</sub> <sup>-</sup> ) nucleic acid	126
1080cm <sup>-1</sup>	Amide II (?)	3
	Typical phospholipids	76
	Phosphate vibrations (phosphodiester groups in	22
	nucleic acids)	
	Collagen	130
	Tryptophan	30
1081cm <sup>-1</sup>	$v_1CO_3^{2-}$ , $v_3PO_4^{3-}$ , $v(C-C)$ skeletal of acyl backbone in	50
	lipid (gauche conformation)	
1082cm <sup>-1</sup>	Carbohydrate residues of collagen	3
	Carbohydrates peak for solutions	3
	Nucleic acids	3
1083cm <sup>-1</sup>	C-N stretching mode of proteins (& lipid mode of	30
	lesser degree)	
	C-N stretching mode of proteins (and lipid mode to a	31
	lesser degree)	
1084cm <sup>-1</sup>	Phosphodiester groups in nucleic acids	3
1086cm <sup>-1</sup>	v(C-C) gauche	70

1087cm <sup>-1</sup>	$v_1CO_3^{2-}$ , $v_3PO_4^{3-}$ , $v(C-C)$ skeletal of acyl backbone in lipid (gauche conformation)	50
1087-90cm <sup>-1</sup>	C-C stretch	31
	PO <sub>2</sub> stretch	
1090cm <sup>-1</sup>	Symmetric phosphate stretching vibrations	3
1092/3cm <sup>-1</sup>	Phosphodioxy	106
1093cm <sup>-1</sup>	Symmetric PO <sub>2</sub> stretching vibration of the DNA	103, 91
	backbone-Phosphate backbone vibration as a marker	
	mode for the DNA concentration-C-N of proteins	
1094cm <sup>-1</sup>	DNA	76
	C-N stretching	52
1095cm <sup>-1</sup>	Lipid	133
	ν(C-N)	50
	Phosphodioxy group (PO <sub>2</sub> <sup>-</sup> in nucleic acids)	122
1096cm <sup>-1</sup>	Phosphodioxy (PO <sub>2</sub> -) groups	71
1099cm <sup>-1</sup>	ν(C-N)	50
1100cm <sup>-1</sup>	C-C vibration mode of the gauche-bonded chain	127
1100-375cm <sup>-1</sup>	Several bands of moderate intensity, belonging to	70
	anide III and other groups (proteins)	
Peak	Assignment	Reference
		Number

1100-800cm <sup>-1</sup>	ν(C-C)-Lipids, fatty acids	64
1101cm <sup>-1</sup>	O-P-O backbone stretch of DNA	28
1104cm <sup>-1</sup>	Phenylalanine (proteins)	70
1105cm <sup>-1</sup>	Carbohydrates peak for solutions	3
1111cm <sup>-1</sup>	Benzoid ring deformation	124
1112cm <sup>-1</sup>	Saccharide band (overlaps with acyl band)	71
1115/6cm <sup>-1</sup>	$CH_{2,6}$ in-plane bend and $C_1\text{-}C_{\alpha}\text{-}H_{\alpha}$ bend	121
1117cm <sup>-1</sup>	Glucose	71
1117-9cm <sup>-1</sup>	C-C stretch (breast lipid)	31
1120cm <sup>-1</sup>	The strong C-O band of ribose (serves as a marker	3
	band for RNA in solutions)	
	Carotene	76
1122cm <sup>-1</sup>	$v_{22}$ (porphyrin half ring), observed in the spectra of	98
	single human RBC	
	$v_s(CC)$ skeletal	126
	v <sub>sym</sub> (C-O-C) (polysaccharides, cellulose)	64
	v(C-C) trans	70
1123cm <sup>-1</sup>	(C-N), proteins (protein assignment)	20
	C-C stretching mode of lipids & protein, C-N stretch	31, 30
	Glucose	31

1124cm <sup>-1</sup>	v(C-C) skeletal of acyl backbone in lipid (transconformation)	50
1126cm <sup>-1</sup>	Paraffin	3
	ν(C-C) skeletal of acyl backbone in lipid (transconformation)	50
	C-N stretching vibration (protein vibration)	103
	$\nu$ (C-O)+ $\nu$ (C-C), Disaccharides, sucrose	64
1126 cm <sup>-1</sup>	C-N stretching	39
1127cm <sup>-1</sup>	ν(C-N)	70
1128cm <sup>-1</sup>	C-N stretching (proteins)	122
	C-O stretching (carbohydrates)	122
	Ceramide	59
1128/9cm <sup>-1</sup>	v(C-C) skeletal of acyl backbone in lipid (transconformation)	50
1130cm <sup>-1</sup>	C-C skeletal stretch transconformation	111
	Phospholipid structural changes ( <i>trans</i> versus <i>gauche</i> isomerism)	129
	Acyl chains	71
Peak	Assignment	Reference Number
1131cm <sup>-1</sup>	Palmitic acid	71

	Fatty acid	71
	C-C skeletal stretching	39
1149cm <sup>-1</sup>	Carbohydrates peak for solids	3
1150cm <sup>-1</sup>	Glycogen	3
	Carotenoid	2
1152cm <sup>-1</sup>	ν(C-N), proteins (protein assignment)	20
	ν(C-C), carotenoids	20
	Carotenoid peaks due to C-C & conjugated C=C band	20
	stretch	
1153cm <sup>-1</sup>	Carbohydrates peak for solutions	3
1154cm <sup>-1</sup>	β-Carotenes	30
1155/6/7cm <sup>-1</sup>	Carotenoids	141
1155cm <sup>-1</sup>	C-C (&C-N) stretching of proteins (also carotenoids)	31, 30
	Glycogen	3
	ν (C-C)- Diagnostic for the presence of a carotenoid	102
	structure, most likely a cellular pigment.	
1156cm <sup>-1</sup>	C-C, C-N stretching (protein)	103
1156/7cm <sup>-1</sup>	Carotenoids (absent in normal tissue)	1
1157cm <sup>-1</sup>	In-plane vibrations of the conjugated =C-C=	95
	β-carotene accumulation (C=C stretch mode)	94

1158cm <sup>-1</sup>	C-C/C-N stretching (proteins)	122
1160cm <sup>-1</sup>	C-C/C-N stretching (proteins)	38
1161cm <sup>-1</sup>	Deformative vibrations of quinoid ring	124
1163cm <sup>-1</sup>	Tyrosine (collagen type I)	50
	Tyrosine	50
1167cm <sup>-1</sup>	N=Quinoid ring=N stretching and C-H in plane	124
	bending	
1168cm <sup>-1</sup>	Lipids	3
	$\nu$ (C=C) $\delta$ (COH) (lipid assignment)	126
	ν(C-C), carotenoids	126
1169cm <sup>-1</sup>	Tyrosine (collagen type I)	50
	Tyrosine	50
1170cm <sup>-1</sup>	C-H in-plane bending mode of tyrosine	31, 30
1171cm <sup>-1</sup>	Tyrosine (collagen type I)	50
	Tyrosine	50
	(CH) Phenylalanine, Tyrosine	70
Peak	Assignment	Reference
		Number
1172cm <sup>-1</sup>	$\delta$ (C-H), tyrosine (protein assignment)	20
1173cm <sup>-1</sup>	Cytosine, guanine	106

	Tyrosine (collagen type I)	50
1174cm <sup>-1</sup>	Tyrosine, phenylalanine, C-H bend (protein)	103
1175/6cm <sup>-1</sup>	Cytosine, guanine	106
1176cm <sup>-1</sup>	C-H bending tyrosine (proteins)	122
1177cm <sup>-1</sup>	Cytosine, guanine	106
1180cm <sup>-1</sup>	Cytosine, guanine	106
1180-84cm <sup>-1</sup>	Cytosine, guanine, adenine	31
1185-300cm <sup>-1</sup>	Anti-symmetric phosphate vibrations	130
1199cm <sup>-1</sup>	Tryptophan ring breathing	39
1200cm <sup>-1</sup>	Nucleic acids and phosphates	130
	Aromatic C-O and C-N	134
1200-300cm <sup>-1</sup>	Amide III (proteins)	122
1200-350cm <sup>-1</sup>	Amide III-Due to C-N stretching and N-H bending	76, 103
1200-360cm <sup>-1</sup>	Electronic structure of nucleotides	103
1203cm <sup>-1</sup>	C-C <sub>6</sub> H <sub>5</sub> stretch mode (one of C-C ring vibration to be	11
	expected in aromatic structure of Xylene)	
1204cm <sup>-1</sup>	Amide III & CH <sub>2</sub> wagging vibrations from glycine	3
	backbone & proline side chains	
	Collagen	
	Tyrosine, Phenylalanine (IgG)	129, 130

1205cm <sup>-1</sup>	Differences in collagen content	3
1206cm <sup>-1</sup>	Hydroxyproline, tyrosine (collagen assignment)	123
	Hydroxyproline, tyrosine	31
1208cm <sup>-1</sup>	$\nu(C\text{-}C_6H_5)$ , tryptophan, phenylalanine (protein assignment)	20, 126
	Tryptophan	50
	A,T (ring breathing modes of the DNA/RNA bases)- Amide III (protein)	103
1209cm <sup>-1</sup>	Tryptophan & phenylalanine $\nu(C\text{-}C_6H_5)$ mode	31, 30, 122
1210cm <sup>-1</sup>	C-C <sub>6</sub> H <sub>5</sub> stretching mode in tyrosine and phenylalanine	78
	$\nu_{18}(\delta;C_m H),$ observed in the spectra of single human RBC	102
1216cm <sup>-1</sup>	Stretching of C-N	124
1220cm <sup>-1</sup>	C=N=C stretching	124
Peak	Assignment	Reference
		Number
1220-1cm <sup>-1</sup>	Amide III (β-sheet)	31
1220-84cm <sup>-1</sup>	T,A (DNA/RNA)	122
	Amide III (proteins)	122
1220-300cm <sup>-1</sup>	Amide III (arising from coupling of C-N stretching & N-H bonding-can be mixed with vibrations of side	53

	chains)(protein band)	
1223cm <sup>-1</sup>	ν(PO <sub>2</sub> -), nucleic acids	20
	Cellular nucleic acids	20
	A concerted ring mode	104
	Proteins, including collagen I	110
1224cm <sup>-1</sup>	Amide III (β sheet structure)	70
1230cm <sup>-1</sup>	Antisymmetric phosphate stretching vibration	3
1230-300cm <sup>-1</sup>	Amide III (arising from coupling of C-N stretching &	3
	N-H bonding- can be mixed with vibrations of side	
	chains)	
1234cm <sup>-1</sup>	A concerted ring mode	104
1235cm <sup>-1</sup>	Amide III	64
1237cm <sup>-1</sup>	Amide III &CH <sub>2</sub> wagging vibrations from glycine	3
	backbone& proline side chains	
1239cm <sup>-1</sup>	Amide III	111
1240cm <sup>-1</sup>	One of the two most distinct peaks for RNA (with	103
	813cm <sup>-1</sup> )	
	Differences in collagen content	3
	Asymmetric phosphate [PO <sub>2</sub> (asym.)] stretching	30
	modes	
	Collagen	130

1241cm <sup>-1</sup>	Asymmetric phosphate [PO <sub>2</sub> <sup>-</sup> (asym.)] stretching modes (phosphate stretching modes originate from the phosphodiester groups of nucleic acids and suggest an increase in the nucleic acids in the malignant tissues)(Generally, the PO <sub>2</sub> <sup>-</sup> groups of phospholipids do not contribute to these bands)	50
1242cm <sup>-1</sup>	Amide III (β sheet and random coils)	70
1243cm <sup>-1</sup>	Amide III	3
	Asymmetric phosphate [PO <sub>2</sub> <sup>-</sup> (asym.)] stretching modes (phosphate stretching modes originate from the phosphodiester groups of nucleic acids and suggest an increase the in nucleic acids in the malignant tissues)(Generally, the PO <sub>2</sub> <sup>-</sup> groups of phospholipids do not contribute to these bands)	
Peak	Assignment	Reference Number
1243cm <sup>-1</sup>	C-O <sub>4</sub> aromatic stretch	50
	Amide III of collagen (CH <sub>2</sub> wagging, C-N stretching) and pyrimidine bases (C, T)	121, 31
1245cm <sup>-1</sup>	Amide III	64
1246cm <sup>-1</sup>	Amide III (of collagen)	50

28
28
102
2) 106
121
n on fixed tissues 35
124
3
odes of the DNA/RNA bases)- 103
osine 31
on 38
2) 106
123
3
2
1
31
es of tumours 27

	Amide III vibration mode of structural proteins	94
	CH <sub>2</sub> in-plane deformation (lipids)	113
1263cm <sup>-1</sup>	T, A (ring breathing modes of the DNA/RNA bases)-	103
	=C-H bend (protein)	
1263/5/9cm <sup>-1</sup>	Lipids	141
1264cm <sup>-1</sup>	Triglycerides (fatty acids)	94
1265cm <sup>-1</sup>	Amide III of collagen	35
	Amide III (collagen assignment)	123
	Amide III	126
	ν(CN), $δ(NH)$ amide III, α-helix, collagen (protein	126
	assignment)	
	ussignment)	
1266cm <sup>-1</sup>	Amide III (of proteins in the $\alpha$ -helix conformation)	20, 50
1266cm <sup>-1</sup>	,	20, 50  Reference
	Amide III (of proteins in the $\alpha$ -helix conformation)	
	Amide III (of proteins in the $\alpha$ -helix conformation)	Reference
Peak	Amide III (of proteins in the α-helix conformation)  Assignment	Reference Number
Peak	Amide III (of proteins in the $\alpha$ -helix conformation)  Assignment $\nu(CN), \delta(NH)$ amide III, $\alpha$ -helix, collagen, tryptophan	Reference Number
Peak	Amide III (of proteins in the $\alpha$ -helix conformation)  Assignment $\nu(CN), \delta(NH)$ amide III, $\alpha$ -helix, collagen, tryptophan (protein assignment)	Reference Number 20
Peak	Amide III (of proteins in the $\alpha$ -helix conformation)  Assignment $v(CN), \delta(NH)$ amide III, $\alpha$ -helix, collagen, tryptophan (protein assignment) $\delta$ (=C-H) $cis$	Reference Number 20
Peak 1266cm <sup>-1</sup>	Amide III (of proteins in the $\alpha$ -helix conformation)  Assignment $\nu(\text{CN}), \delta(\text{NH})$ amide III, $\alpha$ -helix, collagen, tryptophan  (protein assignment) $\delta$ (=C-H) $cis$ Amide III ( $\alpha$ -helix)	Reference Number 20 64 70

1268/9cm <sup>-1</sup>	Amide III (collagen assignment)	123
1270cm <sup>-1</sup>	Typical phospholipids	76
	Amide III band in proteins	52
	Has traditionally been attributed to Amide III, a C-N stretch from alpha helix proteins	112
	C=C groups in unsaturated fatty acids	71
1272/3cm <sup>-1</sup>	$CH_{\alpha}$ , rocking	121
1273cm <sup>-1</sup>	δ (C=CH)	28
1275cm <sup>-1</sup>	Amide III	64
1278cm <sup>-1</sup>	Proteins, including collagen I	110
1279cm <sup>-1</sup>	Amide III (α-helix)	31
1280cm <sup>-1</sup>	Amide III & CH <sub>2</sub> wagging vibrations from glycine	3
	backbone & proline side chains	
	Collagen	
	Nucleic acids and phosphates	130
1283cm <sup>-1</sup>	Differences in collagen content	3
1287/8cm <sup>-1</sup>	Cytosine	106
1288cm <sup>-1</sup>	Phosphodiester groups in nucleic acids	3
1290cm <sup>-1</sup>	Cytosine	106
1290-400cm <sup>-1</sup>	CH bending	135

1291/2cm <sup>-1</sup>	Cytosine	106
1294cm <sup>-1</sup>	Methylene twisting	127
1296cm <sup>-1</sup>	CH <sub>2</sub> deformation	111
	Ceramide	59
1297cm <sup>-1</sup>	Palmitic acid	38
1298cm <sup>-1</sup>	Palmitic acid	71
	Acyl chains	71
	Fatty acids	71
1299/300cm <sup>-1</sup>	CH <sub>2</sub> deformation (lipid)	31
Peak	Assignment	Reference
Peak	Assignment	Reference Number
Peak 1300/1/3/5	Assignment	
		Number
1300/1/3/5	Lipid	Number 141
1300/1/3/5	Lipid -(CH <sub>2</sub> )n- in-plane twist vibration (lipid band)	<b>Number</b> 141 53
1300/1/3/5	Lipid  -(CH <sub>2</sub> )n- in-plane twist vibration (lipid band)  Fatty acids	Number  141  53  3
1300/1/3/5	Lipid  -(CH <sub>2</sub> )n- in-plane twist vibration (lipid band)  Fatty acids  Fatty acids	Number  141  53  3
1300/1/3/5	Lipid  -(CH <sub>2</sub> )n- in-plane twist vibration (lipid band)  Fatty acids  Fatty acids $\delta(\text{CH}_2)$ -lipids, fatty acids	Number  141  53  3  2  64

	CH <sub>2</sub> twisting and wagging (lipids)	113
1301cm <sup>-1</sup>	Assign from Parker (lipid in normal tissue)	76
	Triglycerides (fatty acids)	94
	τ(CH <sub>2</sub> ), lipids	70
	C-H vibration (lipids)	122
	Lipids	122
	CH <sub>2</sub> twisting (lipids)	122
1302cm <sup>-1</sup>	$\delta(CH_2)$ twisting, wagging, collagen (protein assignment)	20, 126
	$\delta(CH_2)$ twisting, wagging, phospholipids (lipid assignment)	20, 126
	CH <sub>3</sub> /CH <sub>2</sub> twisting or bending mode of lipid/collagen	50
	Amide III (protein)	103
	Methylene bending mode (a combination of proteins & phospholipids	35
1303/4cm <sup>-1</sup>	CH <sub>3</sub> ,CH <sub>2</sub> twisting (collagen assignment)	123
1304cm <sup>-1</sup>	CH <sub>2</sub> deformation (lipid), adenine, cytosine	31
1307cm <sup>-1</sup>	CH <sub>3</sub> /CH <sub>2</sub> twisting or bending mode of lipid/collagen	50
	CH <sub>3</sub> /CH <sub>2</sub> twisting, wagging &/or bending mode of collagens & lipids	50
1308cm <sup>-1</sup>	C-N asymmetric stretching in asymmetric aromatic	124

	amines	
1309cm <sup>-1</sup>	CH <sub>3</sub> /CH <sub>2</sub> twisting or bending mode of lipid/collagen	50
	CH <sub>3</sub> /CH <sub>2</sub> twisting, wagging &/or bending mode of	50
	collagens & lipids	
1313cm <sup>-1</sup>	CH <sub>3</sub> CH <sub>2</sub> twisting mode of collagen/lipid	31, 30
1314cm <sup>-1</sup>	CH <sub>3</sub> CH <sub>2</sub> twisting mode of collagen	81
1315cm <sup>-1</sup>	Guanine (B,Z-marker)	106
1317/8/9cm <sup>-1</sup>	Guanine (B,Z-marker)	106
Peak	Assignment	Reference
I can	Assignment	Number
1318cm <sup>-1</sup>	G (ring breathing modes of the DNA/RNA bases)-C-H	103
	deformation (protein)	
	Amide III (α-helix)	70
1319cm <sup>-1</sup>	Guanine (B,Z-marker)	106
	CH <sub>3</sub> CH <sub>2</sub> twisting (collagen assignment)	123
1320cm <sup>-1</sup>	G (DNA/RNA)	122
	CH deformation (proteins)	122
1321cm <sup>-1</sup>	Amide III (α-helix),	70
	CH <sub>2</sub> deformation of lipids	28

	CH <sub>3</sub> CH <sub>2</sub> twisting and wagging in collagen	20
	CH <sub>3</sub> CH <sub>2</sub> deforming modes of collagen and nucleic acids	35
1323cm <sup>-1</sup>	Guanine (B,Z marker)	106
	CH deformation	39
1324cm <sup>-1</sup>	CH <sub>3</sub> CH <sub>2</sub> wagging mode present in collagen & purine bases of DNA	78
1325-30cm <sup>-1</sup>	CH <sub>3</sub> CH <sub>2</sub> wagging mode in purine bases of nucleic acids	112, 59
1330cm <sup>-1</sup>	Typical phospholipids	76
	Region associated with DNA & phospholipids	27
	Collagen	130
	Nucleic acids and phosphates	130
1332cm <sup>-1</sup>	-C stretch of Phenyl (1) and $C_3$ - $C_3$ stretch and $C_5$ - $O_5$ stretch $CH_\alpha$ in-plane bend	121
1333cm <sup>-1</sup>	Guanine	106
1335cm <sup>-1</sup>	CH <sub>3</sub> CH <sub>2</sub> wagging, collagen (protein assignment)	20
	CH <sub>3</sub> CH <sub>2</sub> wagging, nucleic acid	20
	CH <sub>3</sub> CH <sub>2</sub> wagging mode of collagen & polynucleotide chain (DNA purine bases)	30
	CH <sub>3</sub> CH <sub>2</sub> twisting and wagging in collagen	20

	Cellular nucleic acids	20
	CH <sub>3</sub> CH <sub>2</sub> deforming modes of collagen and nucleic acids	35
	An unassigned mode	104
1335-45cm <sup>-1</sup>	CH <sub>3</sub> CH <sub>2</sub> wagging mode of collagen	31
1335/6cm <sup>-1</sup>	Guanine	106
Peak	Assignment	Reference Number
1336cm <sup>-1</sup>	Polynucleotide chain (DNA purine bases)	31
	$\delta(CH_3)  \delta(CH_2)$ twisting, collagen (protein assignment)	126
1337cm <sup>-1</sup>	Amide III & CH <sub>2</sub> wagging vibrations from glycine backbone & proline side chain	3
	A, G (ring breathing modes in the DNA bases)- C-H deformation (protein)	103
1337/9cm <sup>-1</sup>	Tryptophan	50
	CH <sup>2</sup> /CH <sub>3</sub> wagging, twisting &/or bending mode of collagens & lipids	50
	CH <sub>2</sub> /CH <sub>3</sub> wagging & twisting mode in collagen, nucleic acid & tryptophan	50
1339cm <sup>-1</sup>	C-C stretch of Phenyl (1) and $C_3$ - $C_3$ stretch and $C_5$ - $O_5$ stretch $CH_{\alpha}$ in-plane bend	136

1340cm <sup>-1</sup>	Nucleic acid mode	1
	Differences in collagen content	3
	Nucleic acid modes indicating the nucleic acid content	137
	in tissues	
1341cm <sup>-1</sup>	A or G of DNA	67
1342cm <sup>-1</sup>	G (DNA/RNA)	122
	CH deformation (proteins and carbohydrates)	122
1343cm <sup>-1</sup>	CH <sub>3</sub> ,CH <sub>2</sub> wagging (collagen assignment)	123
	Glucose	49
1343/4cm <sup>-1</sup>	δ(CH), residual vibrations	70
1347cm <sup>-1</sup>	An unassigned mode	104
1350cm <sup>-1</sup>	Carbon Particle	33
1355/7cm <sup>-1</sup>	Guanine (N <sub>7</sub> , B,Z-marker	106
1359cm <sup>-1</sup>	Tryptophan	50
1360/4cm <sup>-1</sup>	Tryptophan	64, 37
1361-3/5cm <sup>-1</sup>	Guanine (N <sub>7</sub> , B,Z-marker	106
1365cm <sup>-1</sup>	Tryptophan	50
1367cm <sup>-1</sup>	vs (CH <sub>3</sub> ) (phosphplipids)	70
1369cm <sup>-1</sup>	Guanine, TRP (protein), porphyrins, lipids	34
1370cm <sup>-1</sup>	The most pronounced saccharide band	71

1371cm <sup>-1</sup>	CH3 stretching	39
1373cm <sup>-1</sup>	T, A, G (ring breathing modes of the DNA/RNA	103
	bases)	
1378cm <sup>-1</sup>	Paraffin	3
Peak	Assignment	Reference
		Number
1379cm <sup>-1</sup>	δCH <sub>3</sub> symmetric (lipid assignment)	126
1383cm <sup>-1</sup>	CH <sub>3</sub> band	38
1386cm <sup>-1</sup>	CH <sub>3</sub> band	31
1391cm <sup>-1</sup>	CH rocking	121
1392cm <sup>-1</sup>	C-N stretching, in Quinoid ring_Benzoid ring-Quinoid	124
	ring	
1393cm <sup>-1</sup>	CH rocking	121
1396cm <sup>-1</sup>	βενετοραΧ-	29
1398cm <sup>-1</sup>	C=O symmetric stretch	111
	CH <sub>2</sub> deformation	50
1400cm <sup>-1</sup>	NH in-plane deformation	104
1400-30cm <sup>-1</sup>	v(C=O)O (amino acids aspartic & glutamic acid)	64
1401cm <sup>-1</sup>	Bending modes of methyl groups (one of vibrational	3
	modes of collagen)	
1404cm <sup>-1</sup>	CH deformation	39

1409cm <sup>-1</sup> v <sub>s</sub> COO <sup>-</sup> (IgG?)  1417cm <sup>-1</sup> C=C stretching in quinoid ring  1420-50cm <sup>-1</sup> CH <sub>2</sub> scissoring vibration (lipid band)  1420-70cm <sup>-1</sup> (prominent peak at 1445cm <sup>-1</sup> - being of diagnostic significance)	70 124 53 81
1420-50cm <sup>-1</sup> CH <sub>2</sub> scissoring vibration (lipid band)  1420-70cm <sup>-1</sup> (prominent peak at 1445cm <sup>-1</sup> - being of diagnostic	53
1420-70cm <sup>-1</sup> (prominent peak at 1445cm <sup>-1</sup> - being of diagnostic	
	81
significance)	
CH <sub>2</sub> bending mode of proteins & lipids	
1420-80cm <sup>-1</sup> G, A (DNA, RNA)	122
CH deformation (DNA/RNA & proteins & lipids &	122
carbohydrates)	
1420/1cm <sup>-1</sup> Deoxyribose, (B,Z-marker)	106
1421cm <sup>-1</sup> A, G (ring breathing modes of the DNA/RNA bases)	103
1422cm <sup>-1</sup> Deoxyribose, (B,Z-marker)	106
1423cm <sup>-1</sup> NH in-plane deformation	104
1424cm <sup>-1</sup> Deoxyribose, (B,Z-marker)	106
1436cm <sup>-1</sup> CH <sub>2</sub> scissoring	106
1437cm <sup>-1</sup> CH <sub>2</sub> (lipids in normal tissue)	76
CH <sub>2</sub> deformation (lipid)	31
Acyl chains	71
1437-42cm <sup>-1</sup> CH <sub>2</sub> deformation	71

Peak	Aggignmont	Reference
геак	Assignment	Number
1437-53cm <sup>-1</sup>	CH <sub>2</sub> deformation	113
1438/39/40/42/4	Lipid	141
3cm <sup>-1</sup>		
1439cm <sup>-1</sup>	CH <sub>2</sub> bending mode in normal tissue	21
	CH <sub>3</sub> ,CH <sub>2</sub> deformation (collagen assignment)	123
	CH <sub>2</sub> scissoring	119
	CH <sub>2</sub> deformation in normal breast tissue	123
	CH <sub>2</sub> deformation	123
	CH <sub>2</sub>	76
	$\delta(CH_2)$ (lipids)	70
1440cm <sup>-1</sup>	CH <sub>2</sub> and CH <sub>3</sub> deformation vibrations	2
	CH deformation	71
	Cholesterol, fatty acid band	71
	$\delta(CH_2)$ (lipids)	70
	CH <sub>2</sub> bending (lipids)	70, 113
1441cm <sup>-1</sup>	CH <sub>2</sub> scissoring & CH <sub>3</sub> bending in lipids	78
	Cholesterol & its esters	94
	C-H bending mode of accumulated lipids in the	94

Peak	Assignment	Reference Number
	CH <sub>2</sub> scissoring	20
	CH <sub>2</sub> CH <sub>3</sub> bending modes of collagen & phospholipids	20, 65
	assignment)	
	$\delta(CH_2)$ , $\delta(CH_3)$ , scissoring, phospholipids (lipid	20, 126
1445cm <sup>-1</sup>	$\delta(CH_2)$ , $\delta(CH_3)$ , collagen (protein assignment)	20, 126
	$\delta(CH_2)$ , lipids, fatty acids	63
	RBC	
	$\nu_{28}$ ( $C_{\alpha}C_{m}$ ), observed in the spectra of single human	98
	spectrum)	
1444cm <sup>-1</sup>	Cholesterol band (associated to atherosclerotic	94
	Triglycerides (fatty acids)	94
1443cm <sup>-1</sup>	CH <sub>2</sub> deformation (lipids and proteins)	31
	Triglycerides (fatty acids)	94
	CH <sub>3</sub> ,CH <sub>2</sub> deformation (collagen assignment)	123
	bending mode	
	Due to changes in chemical environment of the CH2	2
	CH <sub>2</sub> bending mode	1
1442cm <sup>-1</sup>	Fatty acids	2, 3
	vecrotic core of the atheromatous plaque	

1445cm <sup>-1</sup>	CH <sub>2</sub> bending mode of proteins & lipids-being of diagnostic significance	81
	CH <sub>2</sub> bending and scissoring modes of collagen and phospholipids	35
	Methylene bending mode (a combination of proteins & phospholipids)	35
	CH <sub>2</sub> bending modes	126
	CH <sub>2</sub> deformation	113
1446cm <sup>-1</sup>	CH <sub>2</sub> bending mode of proteins & lipids	31, 30
	CH <sub>2</sub> deformation	123
1447cm <sup>-1</sup>	CH <sub>2</sub> bending mode of proteins & lipids	111
	CH <sub>2</sub> deformation (protein vibration)-A marker for protein concentration	103
	$\delta as(CH_3)  \delta(CH_2)$ of proteins	70
1448cm <sup>-1</sup>	CH <sub>2</sub> CH <sub>3</sub> deformation	50
	CH <sub>2</sub> deformation	123
	$\mathrm{CH}_2$	76
	Collagen	34
	CH deformation	29
1449cm <sup>-1</sup>	C-H vibration (proteins)	122
	C-H vibration (lipids)	122

	Lipids	122
1450cm <sup>-1</sup>	CH <sub>2</sub> bending	51, 62, 76
	CH <sub>2</sub> bending mode in malignant tissues	21
	Bending modes of methyl groups(one of vibrational	
	modes of collagen)	
	Methylene deformation in biomolecules	3
	CH <sub>2</sub> deformation in IDC breast tissue	123
	C-H deformation bands (CH functional groups in	102
	lipids, amino acids side chains of the proteins and	
	carbohydrates)	
	δ(C-H)	102
	CH <sub>2</sub> bending (proteins)	70
1451cm <sup>-1</sup>	CH <sub>2</sub> CH <sub>3</sub> deformation	70
	CH <sub>2</sub> CH <sub>3</sub> deformation (collagen assignment)	123
1453cm <sup>-1</sup>	Protein bands	2, 3
	Umbrella mode of methoxyl (4)	121
	C-H bending mode of structural proteins	94
1453cm <sup>-1</sup>	Structural protein modes of tumors	27
Peak	Assignment	Reference
		Number
1454cm <sup>-1</sup>	CH <sub>2</sub> stretching/CH <sub>3</sub> assymetric deformation	111

	Overlapping asymmetric CH <sub>3</sub> bending & CH <sub>2</sub>	81
	scissoring (is associated with elastin, collagen&	
	phospholipids)	
	Collagen & phospholipids	27
1455cm <sup>-1</sup>	Deoxyribose	106
	$\delta(CH_2)$	70
1457cm <sup>-1</sup>	Deoxyribose	106
1458cm <sup>-1</sup>	Nucleic acid modes	1
	Nucleic acid modes indicating the nucleic acid content	137
	in tissues	
1459cm <sup>-1</sup>	Deoxyribose	106
	$\delta(\mathrm{CH_2})$	70
1460cm <sup>-1</sup>	CH <sub>2</sub> /CH <sub>3</sub> deformation of lipids & collagen	50
	CH <sub>2</sub> wagging, CH <sub>2</sub> /CH <sub>3</sub> deformation	50
	Deoxyribose	106
1462cm <sup>-1</sup>	$\delta CH_2$ , Disaccharides, sucrose	64
1463cm <sup>-1</sup>	Fermi interaction $\delta(CH_2)$ , & $\gamma(CH_2)$	70
1465cm <sup>-1</sup>	Lipids	3
1470cm <sup>-1</sup>	C=N stretching	124
1472cm <sup>-1</sup>	Paraffin	3

1477cm <sup>-1</sup>	Calcium oxalate	47
1480-575cm <sup>-1</sup>	Amide II (largely due to a coupling of CN stretching & in-plane bending of the N-H group-is not often used for structural studies per se because it is less sensitive & is subject to interference from absorption bounds of amino acid side chain vibrations)	3
1485cm <sup>-1</sup>	G, A (ring breathing modes in the DNA bases)	103
	Nucleotide acid purine bases (guanine and adenine)	31
1485-550cm <sup>-1</sup>	NH <sub>3</sub> <sup>+</sup>	111
1487/8cm <sup>-1</sup>	Guanine (N <sub>7</sub> )	106
1488cm <sup>-1</sup>	Collagen	34
1490cm <sup>-1</sup>	DNA	76
	Formalin peak appearing in the fixed normal and tumor tissues	35
1491cm <sup>-1</sup>	C-N stretching vibration coupled with the in-plane C-H bending in amino radical cations	111
Peak	Assignment	Reference
		Number
1492cm <sup>-1</sup>	Formalin peak appearing in the fixed normal and tumor tissues	35
1499cm <sup>-1</sup>	C-C stretching in benzenoid ring	124

1506cm <sup>-1</sup>	N-H bending	124
1506/08cm <sup>-1</sup> 1510cm <sup>-1</sup>	Cytosine	106
1510cm <sup>-1</sup>	A (ring breathing modes in the DNA bases)	103
1513cm <sup>-1</sup>	Cytosine	106
1514cm <sup>-1</sup>	v(C=C) - Diagnostic for the presence of a carotenoid structure, most likely a cellular pigment	102
	v(C=C) carotenoids	126
1515cm <sup>-1</sup>	Cytosine	106
1515/25cm <sup>-1</sup> 1526cm <sup>-1</sup>	Carotenoids	141
1517cm <sup>-1</sup>	β-carotene accumulation (C-C stretch mode)	94
1518cm <sup>-1</sup>	ν(C=C), porphyrin	20
	Carotenoid peaks due to C-C & conjugated C=C band stretch	20
1520cm <sup>-1</sup>	Carotene	76
1520-38cm <sup>-1</sup>	-C=C- carotenoids	31, 29
1524cm <sup>-1</sup>	Carotenoid (absent in normal tissues)	1
1525cm <sup>-1</sup>	In-plane vibrations of the conjugated -C=C-	95
1528cm <sup>-1</sup>	Carotenoid (absent in normal tissues)	1
1540-680cm <sup>-1</sup>	Amide carbonyl group vibrations and aromatic	134

hydrogens	
Single Human RBC, Amide II	38
v11 ( $C_{\beta}C_{\beta}$ ), observed in the spectra of single human	102
RBC	
Amide II	3
C <sub>6</sub> -H deformation mode	104
Bound & free NADH	76
Tryptophan	67
Proline	29
Tryptophan	31, 30
Tryptophan	20
ν(C=C), tryptophan (protein assignment)	20
ν(C=C), porphyrin	20
Amide II	111
Assignment	Reference
	Number
Tryptophan	50
$\nu$ (CN) and $\delta$ (NH) amide II (protein assignment)	126
ν(C=C) porphyrin	126
Tyrosine, amide II, COO	70
	Single Human RBC, Amide II  v11 ( $C_{\beta}C_{\beta}$ ), observed in the spectra of single human  RBC  Amide II $C_{\delta}$ -H deformation mode  Bound & free NADH  Tryptophan  Proline  Tryptophan  Tryptophan  v(C=C), tryptophan (protein assignment)  v(C=C), porphyrin  Amide II  Assignment  Tryptophan  v (CN) and $\delta$ (NH) amide II (protein assignment)  v(C=C) porphyrin

1560cm <sup>-1</sup>	Tryptophan	52
1560-600cm <sup>-1</sup>	COO	6
1573cm <sup>-1</sup>	Guanine, adenine, TRP (protein)	31
1575cm <sup>-1</sup>	Ring breathing modes in the DNA bases	103
	G, A (ring breathing modes of the DNA/RNA bases)	
1576cm <sup>-1</sup>	Nucleic acid mode	1
	Nucleic acid modes indicating the nucleic acid content	137
	in tissues	
1576/7cm <sup>-1</sup>	Guanine (N <sub>3</sub> )	106
1577cm <sup>-1</sup>	Bound & free NADH	76
	IgG?	70
1578cm <sup>-1</sup>	Guanine (N <sub>3</sub> )	106
	Guanine, adenine	122
1579cm <sup>-1</sup>	Pyrimidine ring (nucleic acids) & heme protein	31, 30
1580cm <sup>-1</sup>	C-C stretching	124
	C=C bending mode of Phenylalanine	100
1582cm <sup>-1</sup>	δ(C=C), phenylalanine	20
	Phenylalanine	20
1583cm <sup>-1</sup>	C=C bending mode of phenylalanine	81
1585cm <sup>-1</sup>	C=C olefinic stretch	111

	C=C olefinic stretch (protein assignment)	127
1585cm <sup>-1</sup>	Phenylalanine, hydroxyproline	38
1586/8cm <sup>-1</sup>	Phenylalanine, hydroxyproline	50
1590cm <sup>-1</sup>	Carbon particles	33
1593cm <sup>-1</sup>	C=N and C=C stretching in quinoid ring	124
1600-800cm <sup>-1</sup>	Amide I band of proteins-Due to C=O stretching	52, 103
	Amide I (which is due mostly to the C=O stretching	3
	vibrations of the peptide backbone-Has been used the	
	most for structural studies due to its high sensitivity to	
	small changes in molecular geometry & hydrogen	
	bonding of peptide group)	
	boliding of peptide group)	
Peak		Reference
Peak	Assignment	Reference Number
Peak 1602cm <sup>-1</sup>		
	Assignment	Number
	Assignment Phenylalanine	Number 20
1602cm <sup>-1</sup>	Assignment  Phenylalanine $\delta(C=C)$ , phenylalanine (protein assignment)	Number 20 50
1602cm <sup>-1</sup>		Number 20 50
1602cm <sup>-1</sup>	Assignment  Phenylalanine δ(C=C), phenylalanine (protein assignment)  C=C in-plane bending mode of phenylalanine & tyrosine	Number 20 50 31, 30
1602cm <sup>-1</sup>	Assignment  Phenylalanine δ(C=C), phenylalanine (protein assignment)  C=C in-plane bending mode of phenylalanine & tyrosine  Ring C-C stretch of Phenyl (1)	Number  20  50  31, 30

1606cm <sup>-1</sup>	C=C bending	39
1607cm <sup>-1</sup>	Tyrosine, Phenylalanine ring vibration	70
	C=C phenylalanine, tyrosine	122
1608/9cm <sup>-1</sup>	Cytosine (NH <sub>2</sub> )	106
1610cm <sup>-1</sup>	Cytosine (NH <sub>2</sub> )	106
1614cm <sup>-1</sup>	Tyrosine	50
1615cm <sup>-1</sup>	Tyrosine, Tryptophan, C=C (protein)	103
	Adenine	30
1616cm <sup>-1</sup>	C=C stretching mode of tyrosine & tryptophan	31, 30
1617cm <sup>-1</sup>	$\nu$ ( $C_aC_b$ ), observed in the spectra of single human	102
	RBC	
	C=C phenylalanine, tyrosine	122
1618cm <sup>-1</sup>	ν(C=C), tryptophan (protein assignment)	20
	ν(C=C), porphyrin	20
	Tryptophan	20
	Bound & free NADH	76
1620cm <sup>-1</sup>	ν(C=C), porphyrin	126
1620-750cm <sup>-1</sup>	In-plane double end vibrations of bases- The spectra in	3
	this region are very sensitive to base-pairing	
	interactions & base-stacking effects, i.e effects of	

	hydrogen bond formation	
1622cm <sup>-1</sup>	Tryptophan	50
	Tryptophan &/or β-sheet	50
	Tryptophan (IgG?)	70
1623cm <sup>-1</sup>	Tryptophan	38
1628cm <sup>-1</sup>	$C_{\alpha}=C_{\alpha}$ stretch	121
	Amide C=O stretching absorption for the β-form	6
	polypeptide films	
1634cm <sup>-1</sup>	Amide I	3
1635cm <sup>-1</sup>	Differences in collagen content	3
1637cm <sup>-1</sup>	Amide I band	111
1637cm <sup>-1</sup>		111 Reference
	Amide I band  Assignment	
		Reference
	Assignment	Reference Number
Peak	<b>Assignment</b> Amide I band (both α-helix and β-structure)	Reference Number 70
Peak	Assignment  Amide I band (both $\alpha$ -helix and $\beta$ -structure)  Intermolecular bending mode of water	Reference Number 70 31
Peak 1638cm <sup>-1</sup>	Assignment  Amide I band (both $\alpha$ -helix and $\beta$ -structure)  Intermolecular bending mode of water  Very weak and broad $\nu_2$ mode of water	Reference Number 70 31 70
Peak  1638cm <sup>-1</sup> 1640-80cm <sup>-1</sup>	Assignment  Amide I band (both $\alpha$ -helix and $\beta$ -structure)  Intermolecular bending mode of water  Very weak and broad $\nu_2$ mode of water  Amide I band (protein band)	Reference           Number           70           31           70           142

	Protein amide I absorption	
	Amide I	55
1652/3cm <sup>-1</sup>	Lipid (C=C stretch)	31
1653/4/5	Lipid	141
1653cm <sup>-1</sup>	Carbonyl stretch (C=O), Amide I	104, 38
1654cm <sup>-1</sup>	Due to a combination of C=C stretch & the Amide I	3, 21
	bands + Amide I	
	Amide I (collagen assignment)	123
	C=C stretch	123
	Amide I (C=O stretching mode of proteins, α-helix	31
	conformation)/C=C lipid strech	
	Collagen	27
1655cm <sup>-1</sup>	Amide I (of collagen)	50
	C=C (of lipids in normal tissues- not that of amide I)	77
	ν(C=O) amide I, α-helix, collagen	20, 62, 126
	Amide I (C=O stretching mode of proteins, α-helix	31, 30
	conformation)/C=C lipid strech	
	In normal tissues : C=C of lipids (& not amide I)	20
	C=O stretching of collagen & elastin (protein	20
	assignment)	
	Amide I of proteins	35, 126

	Amide I (collagen assignment)	123
	Amide I (typically associated with collagen)	112
	Amide I (α-helix), Amide I	64, 39
1655-80cm <sup>-1</sup>	Amide I (proteins)	122
	C=O stretching (lipids)	122
1656cm <sup>-1</sup>	C=C (lipids)	70
	Amide I (proteins)	70
1655-80cm <sup>-1</sup>	T, G, C (ring breathing modes of the DNA/RNA	103
	bases)-amide I (protein)	
Peak	Assignment	Reference
Tean	1 issignment	Number
1656cm <sup>-1</sup>	v(C=C)cis (phospholipids)	70
1657cm <sup>-1</sup>	Fatty acids	
	ratty actus	2, 3
	Amide I (collagen assignment)	2, 3
1658cm <sup>-1</sup>	Amide I (collagen assignment)	123
1658cm <sup>-1</sup>	Amide I (collagen assignment)  Triglycerides (fatty acids)	123 94
	Amide I (collagen assignment)  Triglycerides (fatty acids)  Amide I (α-helix)	123 94 70
	Amide I (collagen assignment)  Triglycerides (fatty acids)  Amide I (α-helix)  Amide I vibration (collagen like proteins)	123 94 70 33, 131
	Amide I (collagen assignment)  Triglycerides (fatty acids)  Amide I (α-helix)  Amide I vibration (collagen like proteins)  Amide C=O stretching absorption for the α-folded	123 94 70 33, 131

	Glutathione	29
1660cm <sup>-1</sup>	Amide I band	102
	Amide I	102
	Amide I vibration mode of structural proteins	94
	v(C=C) cis, lipids, fatty acids	64
	C=C groups in unsaturated fatty acids	71
	Ceramide backbone	71
	Amide I (protein)	122
	Lipids	122
1662cm <sup>-1</sup>	Nucleic acid modes	1
	Nucleic acid modes indicating the nucleic acid content	138
	in tissues	
1663cm <sup>-1</sup>	DNA	110
	Proteins, including collagen I	110
1664/5cm <sup>-1</sup>	Amide I	50
1665cm <sup>-1</sup>	Amide I (of collagen)	50
	Amide I	50
	Amide I (collagen assignment)	123
	Amide I (disordered structure-solvated)	64
	$v_s(C=O)$	139

1666cm <sup>-1</sup>	Collagen	34
1667cm <sup>-1</sup>	Protein band	2, 3
	C=C stretching band	1
	α-helical structure of amide I	20
	Structural protein modes of tumors	27
	Carbonyl stretch (C=O)	104
1669cm <sup>-1</sup>	Carbonyl stretch (C=O)	104
	Cholesterol ester	71
1670cm <sup>-1</sup>	Amide I	51
		Reference
D 1	<b>▲</b> •	
Peak	Assignment	Number
<b>Peak</b> 1670cm <sup>-1</sup>	Assignment  C=C stretching vibrations	Number 2
	C=C stretching vibrations	2
	C=C stretching vibrations Cholesterol & its esters	2 94
	C=C stretching vibrations  Cholesterol & its esters  C=C stretching vibration mode of steroid ring	2 94 94
	C=C stretching vibrations  Cholesterol & its esters  C=C stretching vibration mode of steroid ring  Amide I (Anti-parallel β-sheet)	2 94 94 64
1670cm <sup>-1</sup>	C=C stretching vibrations  Cholesterol & its esters  C=C stretching vibration mode of steroid ring  Amide I (Anti-parallel β-sheet)  v(C=C) trans, lipids, fatty acids	2 94 94 64 64
1670cm <sup>-1</sup>	C=C stretching vibrations  Cholesterol & its esters  C=C stretching vibration mode of steroid ring  Amide I (Anti-parallel β-sheet)  v(C=C) trans, lipids, fatty acids  C=C stretch	2 94 94 64 64 121

Cholesterol 71  1676cm <sup>-1</sup> Amide I ( $\beta$ -sheet) 70  1678cm <sup>-1</sup> Bound & free NADH 76  1682cm <sup>-1</sup> One of absorption positions for the C=O stretching vibrations of cortisone  1685cm <sup>-1</sup> Amide I (disordered structure-non-hydrogen bonded) 64  1697cm <sup>-1</sup> Amide I (turns and bands) 70  1700-50cm <sup>-1</sup> v(C=O)OH (amino acids aspartic & glutamic acid) 64  1710cm <sup>-1</sup> One of absorption positions for the C=O stretching vibrations of cortisone  1716-41cm <sup>-1</sup> C=O 71  1720cm <sup>-1</sup> Lipid 37  1725cm <sup>-1</sup> C=O lipids 38  1729cm <sup>-1</sup> Ester group 71  1732cm <sup>-1</sup> One of absorption positions for the C=O stretching of wibrations of cortisone	1674cm <sup>-1</sup>	C=C stretch vibration	71
1678cm <sup>-1</sup> Bound & free NADH 76 1682cm <sup>-1</sup> One of absorption positions for the C=O stretching vibrations of cortisone  1685cm <sup>-1</sup> Amide I (disordered structure-non-hydrogen bonded) 64 1697cm <sup>-1</sup> Amide I (turns and bands) 70 1700-50cm <sup>-1</sup> v(C=O)OH (amino acids aspartic & glutamic acid) 64 1710cm <sup>-1</sup> One of absorption positions for the C=O stretching vibrations of cortisone  1716-41cm <sup>-1</sup> C=O 71 1720cm <sup>-1</sup> Lipid 37 1725cm <sup>-1</sup> C=O lipids 38 1729cm <sup>-1</sup> Ester group 71 1732cm <sup>-1</sup> One of absorption positions for the C=O stretching 6		Cholesterol	71
1682cm <sup>-1</sup> One of absorption positions for the C=O stretching vibrations of cortisone  1685cm <sup>-1</sup> Amide I (disordered structure-non-hydrogen bonded)  64 1697cm <sup>-1</sup> Amide I (turns and bands)  70 1700-50cm <sup>-1</sup> v(C=O)OH (amino acids aspartic & glutamic acid)  64 1710cm <sup>-1</sup> One of absorption positions for the C=O stretching vibrations of cortisone  1716-41cm <sup>-1</sup> C=O  71 1720cm <sup>-1</sup> Lipid  37 1725cm <sup>-1</sup> C=O lipids  38 1729cm <sup>-1</sup> Ester group  71 1732cm <sup>-1</sup> One of absorption positions for the C=O stretching 6	1676cm <sup>-1</sup>	Amide I (β-sheet)	70
vibrations of cortisone  1685cm <sup>-1</sup> Amide I (disordered structure-non-hydrogen bonded) 64  1697cm <sup>-1</sup> Amide I (turns and bands) 70  1700-50cm <sup>-1</sup> v(C=O)OH (amino acids aspartic & glutamic acid) 64  1710cm <sup>-1</sup> One of absorption positions for the C=O stretching vibrations of cortisone  1716-41cm <sup>-1</sup> C=O 71  1720cm <sup>-1</sup> Lipid 37  1725cm <sup>-1</sup> C=O lipids 38  1729cm <sup>-1</sup> Ester group 71  1732cm <sup>-1</sup> One of absorption positions for the C=O stretching 6	1678cm <sup>-1</sup>	Bound & free NADH	76
1685cm <sup>-1</sup> Amide I (disordered structure-non-hydrogen bonded) 64 1697cm <sup>-1</sup> Amide I (turns and bands) 70 1700-50cm <sup>-1</sup> v(C=O)OH (amino acids aspartic & glutamic acid) 64 1710cm <sup>-1</sup> One of absorption positions for the C=O stretching vibrations of cortisone 71 1720cm <sup>-1</sup> Lipid 37 1725cm <sup>-1</sup> C=O lipids 38 1729cm <sup>-1</sup> Ester group 71 1732cm <sup>-1</sup> One of absorption positions for the C=O stretching 6	1682cm <sup>-1</sup>	One of absorption positions for the C=O stretching	6
1697cm <sup>-1</sup> Amide I (turns and bands)  1700-50cm <sup>-1</sup> v(C=O)OH (amino acids aspartic & glutamic acid)  1710cm <sup>-1</sup> One of absorption positions for the C=O stretching vibrations of cortisone  1716-41cm <sup>-1</sup> C=O  171 1720cm <sup>-1</sup> Lipid  37 1725cm <sup>-1</sup> C=O lipids  38 1729cm <sup>-1</sup> Ester group  71 1732cm <sup>-1</sup> One of absorption positions for the C=O stretching 6		vibrations of cortisone	
1700-50cm <sup>-1</sup> v(C=O)OH (amino acids aspartic & glutamic acid) 64  1710cm <sup>-1</sup> One of absorption positions for the C=O stretching 6 vibrations of cortisone  1716-41cm <sup>-1</sup> C=O 71  1720cm <sup>-1</sup> Lipid 37  1725cm <sup>-1</sup> C=O lipids 38  1729cm <sup>-1</sup> Ester group 71  1732cm <sup>-1</sup> One of absorption positions for the C=O stretching 6	1685cm <sup>-1</sup>	Amide I (disordered structure-non-hydrogen bonded)	64
1710cm <sup>-1</sup> One of absorption positions for the C=O stretching vibrations of cortisone  1716-41cm <sup>-1</sup> C=O 71  1720cm <sup>-1</sup> Lipid 37  1725cm <sup>-1</sup> C=O lipids 38  1729cm <sup>-1</sup> Ester group 71  1732cm <sup>-1</sup> One of absorption positions for the C=O stretching 6	1697cm <sup>-1</sup>	Amide I (turns and bands)	70
vibrations of cortisone  1716-41cm <sup>-1</sup> C=O 71  1720cm <sup>-1</sup> Lipid 37  1725cm <sup>-1</sup> C=O lipids 38  1729cm <sup>-1</sup> Ester group 71  1732cm <sup>-1</sup> One of absorption positions for the C=O stretching 6	1700-50cm <sup>-1</sup>	ν(C=O)OH (amino acids aspartic & glutamic acid)	64
1716-41cm <sup>-1</sup> C=O       71         1720cm <sup>-1</sup> Lipid       37         1725cm <sup>-1</sup> C=O lipids       38         1729cm <sup>-1</sup> Ester group       71         1732cm <sup>-1</sup> One of absorption positions for the C=O stretching       6	1710cm <sup>-1</sup>	One of absorption positions for the C=O stretching	6
1720cm <sup>-1</sup> Lipid 37 1725cm <sup>-1</sup> C=O lipids 38 1729cm <sup>-1</sup> Ester group 71 1732cm <sup>-1</sup> One of absorption positions for the C=O stretching 6		vibrations of cortisone	
1725cm <sup>-1</sup> C=O lipids 38  1729cm <sup>-1</sup> Ester group 71  1732cm <sup>-1</sup> One of absorption positions for the C=O stretching 6	1716-41cm <sup>-1</sup>	C=O	71
1729cm <sup>-1</sup> Ester group 71  1732cm <sup>-1</sup> One of absorption positions for the C=O stretching 6	1720cm <sup>-1</sup>	Lipid	37
One of absorption positions for the C=O stretching 6	1725cm <sup>-1</sup>	C=O lipids	38
	1729cm <sup>-1</sup>	Ester group	71
vibrations of cortisone	1732cm <sup>-1</sup>	One of absorption positions for the C=O stretching	6
		vibrations of cortisone	
1734cm <sup>-1</sup> Esters, C=O stretching (lipids) 122	1734cm <sup>-1</sup>	Esters, C=O stretching (lipids)	122
1736cm <sup>-1</sup> C=O ester (lipids) 122	1736cm <sup>-1</sup>	C=O ester (lipids)	122
1737cm <sup>-1</sup> C=O Ester (lipids) 38	1737cm <sup>-1</sup>	C=O Ester (lipids)	38

1738cm <sup>-1</sup>	Lipids	3
1739cm <sup>-1</sup>	Ester group	71
1740cm <sup>-1</sup>	Ester group	71
1743/5cm <sup>-1</sup>	Lipid	141
1744cm <sup>-1</sup>	Carbonyl feature of lipid spectra	42
	Ester group	71
1745cm <sup>-1</sup>	Phospholipids	20
Peak	Assignment	Reference
	<b>g</b>	Number
1745cm <sup>-1</sup>	ν(C=O), phospholipids (Lipid assignment)	20, 126
	ν(C=O), phospholipids	131
	Triglycerides (fatty acids)	94
	v(C=O) (polysaccharides, pectin)	64
1746cm <sup>-1</sup>	C=O stretch (lipid)	31
1747cm <sup>-1</sup>	C=O, lipids	70
1750cm <sup>-1</sup>	C=O (lipid in normal tissues)	76
	ν(C=C) lipids, fatty acids	64
1754cm <sup>-1</sup>	C=O (lipid)	70
1756cm <sup>-1</sup>	One of absorption positions for the C=O stretching vibrations of cortisone	6

2095cm <sup>-1</sup>	C-N stretch (one of three thiocyanate peaks, with 445 & 735 cm <sup>-1</sup> )	104
2225cm <sup>-1</sup>	C≡N	19
2300-3800cm <sup>-1</sup>	Region of the OH-NH-CH stretching vibrations	128
2343cm <sup>-1</sup>	Asymmetric stretching band of CO <sub>2</sub> hydrates	128
2550-80cm <sup>-1</sup>	v(S-H) (aminoacid methionine)	64
2700-	C-H stretches	19
3300cm <sup>-1</sup>		
2700-	Stretching vibrations of CH, NH, and OH groups	71
3500cm <sup>-1</sup>		
2741cm <sup>-1</sup>	Stretching vibrations of CH, NH, and OH groups	38
2800-	Contributions from acyl chans	71
3050cm <sup>-1</sup>		
2800-	CH, CH <sub>2</sub> , & CH <sub>3</sub> symmetric and antisymmetric	137
3100cm <sup>-1</sup>	stretching	
2817-49cm <sup>-1</sup>	CH <sub>2</sub> symmetric stretch of lipids (suggests change in	113
	the amount of lipid)	
2840-75cm <sup>-1</sup>	CH <sub>3</sub> symmetric stretch of lipids	113
2850cm <sup>-1</sup>	$\nu_s$ CH <sub>2</sub> , lipids, fatty acids	64
	CH <sub>2</sub> symmetric	
2850-75cm <sup>-1</sup>	CH <sub>2</sub> symmetric stretch of lipids	113

2853-81cm <sup>-1</sup>	CH <sub>2</sub> symmetric stretch of lipids & CH <sub>2</sub> asymmetric stretch of lipids and proteins	113
2876-906cm <sup>-1</sup>	CH <sub>2</sub> asymmetric stretch and CH stretch of lipids and proteins	113
2876-919cm <sup>-1</sup>	CH <sub>2</sub> asymmetric stretch of lipids and proteins	113
2879cm <sup>-1</sup>	CH <sub>2</sub> and CH of lipids and proteins	38
Peak	Assignment	Reference Number
2883cm <sup>-1</sup>	CH <sub>2</sub> asymmetric stretch of lipids and proteins	113
2885cm <sup>-1</sup>	ν <sub>s</sub> CH <sub>3</sub> , lipids, fatty acids	64
2886cm <sup>-1</sup>	Fermi resonance CH <sub>2</sub> stretch	71
2889-908cm <sup>-1</sup>	CH <sub>2</sub> asymmetric stretch of lipids and proteins	113
2900cm <sup>-1</sup>	CH stretch of lipids and proteins	113
2893/4/5cm <sup>-1</sup>	CH <sub>3</sub> symmetric stretch	142
2900cm <sup>-1</sup>	CH stretch	141
2910-65cm <sup>-1</sup>	CH <sub>3</sub> stretching vibrations	55
2913-38cm <sup>-1</sup>	CH stretch of lipids and proteins	133, 38
2915cm <sup>-1</sup>	CH band of lipids and proteins (The lipid band has a tendency towards higher levels of energy, such as 2855cm <sup>-1</sup> , while the protein band's tendency is towards lower energy levels like 2920cm <sup>-1</sup> )	42

2928cm <sup>-1</sup>	Symmetric CH <sub>3</sub> stretch	42
	Due primarily to protein	42
2929-40cm <sup>-1</sup>	CH <sub>2</sub> asymmetric stretch	113
2933cm <sup>-1</sup>	CH <sub>2</sub> asymmetric stretch	113
2935cm <sup>-1</sup>	Chain end CH <sub>3</sub> symmetric band	71
2940cm <sup>-1</sup>	C-H vibrations in lipids & proteins	52
	ν <sub>as</sub> CH <sub>2</sub> , lipids, fatty acids	64
2956/7cm <sup>-1</sup>	CH <sub>3</sub> asymmetric stretch	142
2960cm <sup>-1</sup>	Out-of-plane chain end antisymmetric CH <sub>3</sub> stretch	71
	band	
2970cm <sup>-1</sup>	v <sub>as</sub> CH <sub>3</sub> , lipids, fatty acids	64
	Cholecterol and cholesterol ester	71
2971/3cm <sup>-1</sup>	Asymmetric stretching of methoxy(4)	121
2987cm <sup>-1</sup>	cholesterol ester cholesterol ester	38
>3000cm <sup>-1</sup>	CH stretching	135
3006	Bond =C-H stretch	141
3008cm <sup>-1</sup>	ν <sub>as</sub> (=C-H), lipids, fatty acids	64
3010cm <sup>-1</sup>	Unsaturated =CH stretch	71
3015cm <sup>-1</sup>	v=CH of lipids	121
3232cm <sup>-1</sup>	O-H & N-H stretching vibrations (hydrogen bonding	142

	network may vary in the malignant tissues)	
3296cm <sup>-1</sup>	NH asymmetric stretching (proteins), Amide A	28
Peak	Assignment	Reference
		Number
3300cm <sup>-1</sup>	Attributed to OH stretch	71
3329cm <sup>-1</sup>	N-H vibration of proteins	55
3350-550cm <sup>-1</sup>	OH stretching	55
3550cm <sup>-1</sup>	O-H stretching vibration	143